

# **NANOLITHOGRAPHIC CONTROL OF CARBON NANOTUBE SYNTHESIS**

A Thesis

by

DAVID HUITINK

Submitted to the Office of Graduate Studies of  
Texas A&M University  
in partial fulfillment of the requirements for the degree of

MASTER OF SCIENCE

December 2007

Major Subject: Mechanical Engineering

# NANOLITHOGRAPHIC CONTROL OF CARBON NANOTUBE SYNTHESIS

A Thesis

by

DAVID HUITINK

Submitted to the Office of Graduate Studies of  
Texas A&M University  
in partial fulfillment of the requirements for the degree of

MASTER OF SCIENCE

Approved by:

Chair of Committee,  
Committee Members,

Head of Department,

Debjyoti Banerjee  
Warren Heffington  
Tahir Cagin  
Dennis O'Neal

December 2007

Major Subject: Mechanical Engineering

## ABSTRACT

Nanolithographic Control of Carbon Nanotube Synthesis. (December 2007)

David Huitink, B.S. Texas A&M University

Chair of Advisory Committee: Dr. Debjyoti Banerjee

A method offering precise control over the synthesis conditions to obtain carbon nanotube (CNT) samples of a single chirality (metallic or semi-conducting) is presented. Using this nanolithographic method of catalyst deposition, the location of CNT growth is also precisely defined.

This technique obviates three significant hurdles that are preventing the exploitation of CNT in micro- and nano-devices. Microelectronic applications (e.g., interconnects, CNT gates, etc.) require precisely defined locations and spatial density, as well as precisely defined chirality for the synthesized CNT. Conventional CVD synthesis techniques typically yield a mixture of CNT (semi-conducting and metallic types) that grow at random locations on a substrate in high number density, which leads to extreme difficulty in application integration.

Dip Pen Nanolithography (DPN) techniques were used to deposit the catalysts at precisely defined locations on a substrate and to precisely control the catalyst composition as well as the size of the patterned catalyst. After deposition of catalysts, a low temperature Chemical Vapor Deposition (CVD) process at atmospheric pressure was used to synthesize CNT. Various types of catalysts (Ni, Co, Fe, Pd, Pt, and Rh) were deposited in the form of metal salt solutions or nano-particle solutions. Various

characterization studies before and after CVD synthesis of CNT at the location of the deposited catalysts showed that the CNT were of a single chirality (metallic or semi-conducting) as well as a single diameter (with a very narrow range of variability). Additionally, X-ray photoelectron spectroscopy (XPS) was used to characterize the deposited samples before and after the CVD, as was lateral force microscopy (LFM) for determination of the successful deposition of the catalyst material immediately after DPN as well as following the CVD synthesis of the samples. The diameter of the CNT determines the chirality. The diameter of the CNT measured by TEM was found to be consistent with the chirality measurements obtained from Raman Spectroscopy for the different samples. Hence, the results showed that CNT samples of a single chirality can be obtained by this technique. The results show that the chirality of the synthesized CNT can be controlled by changing the synthesis conditions (e.g., size of the catalyst patterns, composition of the catalysts, temperature of CVD, gas flow rates, etc.).

For

My beloved wife, Linsay, and our wonderful son, Davis

## ACKNOWLEDGEMENTS

First of all, I would like to thank Dr. Banerjee for providing me with an incredible opportunity to conduct meaningful research in such an interesting field. I can definitely say that I have learned more in the process of researching over the past year than I would have ever expected. Also, for his guidance and support as my research advisor and committee chair, I am grateful for his efforts to aid my pursuit of this degree. I am also thankful for the opportunity for which he allowed me to be a co-participant in the Summer Research Fellowship Program for the Air Force Research Laboratory at Wright-Patterson Air Force Base in Dayton, Ohio. It was a valuable and memorable experience. Additionally, I extend my thanks to Dr. Cagin and Dr. Heffington for their participation in my oversight committee, and to Dr. Heffington, once more, for his support and mentoring throughout my academic career.

To all who helped in the process of completing the research – thank you! Dr. Sinha played a vital role in the actual CVD synthesis of the samples. Rohit Gargate took on an immense task of trying to fill in for me during my absence to Dayton. Thanks also to Dr. Raj Ganguli of the Materials Directorate at the Air Force Research Laboratory in Dayton, OH for help with SEM measurements during my stay there. And to the staff of the Texas A&M Materials Characterization Facility and the Microscopy and Imaging Center, thanks for your help in troubleshooting the equipment, and giving the occasional needed “pointers.”

Furthermore, I would like to thank my wonderfully supportive wife, Linsay, and our son, Davis, for putting up with the odd hours, late night studying, and travel which separated us for several weeks. I love you both. And to my family and friends who encouraged me, thanks for always being there.

## TABLE OF CONTENTS

	Page
ABSTRACT .....	iii
ACKNOWLEDGEMENTS .....	vi
LIST OF FIGURES .....	x
LIST OF TABLES .....	xv
NOMENCLATURE .....	xvi
CHAPTER I      INTRODUCTION .....	1
1.1 Carbon Nanotube Synthesis .....	1
1.2 Carbon Nanotube Characterization .....	3
1.3 Research Motivation .....	6
1.4 Dip Pen Nanolithography .....	7
CHAPTER II      DESCRIPTION OF EXPERIMENTAL APPARATUS .....	15
2.1 Introduction to Experimental Apparatus .....	15
2.2 Deposition and Manipulation .....	16
2.3 Substrates .....	17
2.3.1 DPN Samples .....	17
2.3.2 Bulk Samples .....	19
2.4 CVD Furnace .....	19
2.5 Verification and Evaluation .....	20
CHAPTER III      EXPERIMENTAL PROCEDURE .....	23
3.1 Sample Preparation .....	23
3.1.1 DPN Pen .....	23
3.1.2 DPN Patterning .....	24
3.1.3 “Bulk” Prepared Samples .....	27
3.2 CVD Synthesis .....	27
3.3 Evaluation .....	28
3.3.1 XPS .....	28
3.3.2 XRD .....	29
3.3.3 Raman .....	29
3.3.4 TEM/SEM .....	29
3.3.5 LFM .....	30



	Page
CHAPTER IV RESULTS AND DISCUSSION .....	31
4.1 DPN Depositions / LFM Measurements.....	31
4.1.1 Prior to CVD: Deposition Measurements .....	31
4.1.2 Post CVD Comparison.....	37
4.2 XPS Characterization.....	38
4.3 XRD Characterization.....	42
4.4 Direct Measurements Using TEM and SEM .....	43
4.4.1 TEM of Bulk Deposited Samples.....	43
4.4.2 TEM of DPN Samples.....	46
4.4.3 SEM of AFM Tip Samples.....	48
4.5 Raman Spectral Characterization.....	50
4.5.1 Samples Prepared on SiN <sub>3</sub> .....	50
4.5.2 Samples Prepared on AFM Probe Tips .....	59
4.5.3 Overview of Raman Results.....	61
CHAPTER V CONCLUSION .....	63
REFERENCES.....	65
APPENDIX A XPS ELECTRON HYBRIDIZATION LEVELS .....	69
APPENDIX B RAMAN SPECTRA FOR SAMPLES BY EXCITATION WAVELENGTH .....	70
VITA .....	84

## LIST OF FIGURES

		Page
Figure 1.	Armchair and Zig-Zag Type CNT Chiralities.....	5
Figure 2.	Schematic of DPN "Ink" Deposition.....	7
Figure 3.	Schematic Explaining Registration Capability of DPN .....	12
Figure 4.	DPN of MHA 75 nm Line Array on Gold Substrate.....	13
Figure 5.	Digital Instruments Nanoscope IIIA Atomic Force Microscope (Left) and Veeco Silicon Nitride AFM Probe (Right) .....	15
Figure 6.	Inkwell Chip (left) and Microscope Image (8x) of Individual Inkwell.....	16
Figure 7.	Sindex Chip Surface.....	17
Figure 8.	Magnified Image of SiN <sub>3</sub> Perforated Window Grid.....	18
Figure 9.	CVD System (Courtesy of S.K. Sinha, UNH) .....	19
Figure 10.	Kratos Axis Ultra Imaging XPS.....	20
Figure 11.	JEOL 2010 Transmission Electron Microscope.....	21
Figure 12.	JY Horiba LabRam IR Raman Spectrometer.....	21
Figure 13.	LFM Image of PtCl <sub>2</sub> DPN on SiN <sub>3</sub> .....	25
Figure 14.	Tip-to-Tip Schematic .....	26
Figure 15.	AFM Scan During "Tip 2 Tip" Deposition for Verification of Probe Placement.....	26
Figure 16.	DPN of NiCl <sub>2</sub> onto (A) Sindex Chip and (B) SiN <sub>3</sub> Membrane.....	31
Figure 17.	DPN of CoCl <sub>2</sub> onto (A) Sindex Chip and (B) SiN <sub>3</sub> Membrane .....	32
Figure 18.	DPN of PdCl <sub>2</sub> onto (A) Sindex Chip and (B) SiN <sub>3</sub> Membrane.....	33

	Page	
Figure 19.	LFM Imaging of PdCl <sub>2</sub> DPN on Sindex Chip (a) Before and (b) After CVD, Including (c) 3D Image and (d) Closer 3D Scan of Post CVD.....	38
Figure 20.	XPS Response of Metal Salts Prior to CVD for NiCl <sub>2</sub> (top), CoCl <sub>2</sub> (middle), and PdCl <sub>2</sub> (bottom) .....	39
Figure 21.	XPS Response after CVD for PdCl <sub>2</sub> (top), NiCl <sub>2</sub> (middle), and CoCl <sub>2</sub> (bottom) .....	40
Figure 22.	XPS Verification of Carbon Presence Prior to CVD (a) and After CVD (b).....	41
Figure 23.	XRD Response for Post-CVD PdCl <sub>2</sub> Bulk Sample on Si .....	43
Figure 24.	Bundle of CNTs Grown from Bulk Deposition of NiCl <sub>2</sub> .....	44
Figure 25.	CNT Formations from CoCl <sub>2</sub> (Left) and NiCl <sub>2</sub> -CoCl <sub>2</sub> Mixture (Right) Bulk Deposits.....	45
Figure 26.	CNT Bundle Grown from 1um DPN Pattern (PdCl <sub>2</sub> ).....	45
Figure 27.	CNT Formation from 1um DPN Pattern (NiCl <sub>2</sub> ) .....	46
Figure 28.	CNT Formation from 2um DPN Pattern (CoCl <sub>2</sub> ).....	47
Figure 29.	CNT Formation from 30 second Stationary DPN Pattern (NiCl <sub>2</sub> -CoCl <sub>2</sub> Mixture).....	47
Figure 30.	SEM Micrographs of Clean AFM Tip (Left) and Post-CVD Tip-to-Tip Sample Showing Presence of CVD Deposit (Right).....	48
Figure 31.	SEM Micrograph of Deposited Material on Post-CVD Inkwell Dipped Sample .....	49
Figure 32.	EDX Analysis of Tip-to-Tip Sample .....	50
Figure 33.	Comparison of Raman Laser Excitation for Wavelengths of 633 and 785nm.....	51
Figure 34.	Full Raman Spectra of MWNT .....	52

	Page
Figure 35.	Raman Spectra for CNTs Grown from Bulk and DPN Deposits of NiCl <sub>2</sub> .....53
Figure 36.	Raman Spectra for CNTs Grown from Bulk and DPN Deposits of CoCl <sub>2</sub> .....55
Figure 37.	Raman Spectra for CNTs Grown from Bulk and DPN Deposits of PdCl <sub>2</sub> .....56
Figure 38.	Raman Spectra for CNTs Grown from Bulk and DPN Deposits of NiCl <sub>2</sub> -CoCl <sub>2</sub> Mixture.....57
Figure 39.	Raman Scans of Anomalous Behavior on DPN Samples Showing MWNT .....58
Figure 40.	Raman of Samples Prepared on AFM Probes (NiCl <sub>2</sub> ) .....59
Figure 41.	CoCl <sub>2</sub> Tip-to-Tip CNT Sample Raman Spectrum.....61
Figure B - 1.	Spectra Excitation Comparison of Bulk Prepared CNT Sample of CoCl <sub>2</sub> .....71
Figure B - 2.	Spectra Excitation Comparison of 1 μm DPN Patterned CNT Sample of CoCl <sub>2</sub> .....71
Figure B - 3.	Alternate Excitation Comparison of 500 nm DPN Patterned CNT Sample of CoCl <sub>2</sub> .....72
Figure B - 4.	Alternate Excitation Comparison of 250nm DPN Patterned CNT Sample of CoCl <sub>2</sub> .....72
Figure B - 5.	Alternate Excitation Comparison of 2 μm DPN Patterned CNT Sample of CoCl <sub>2</sub> .....73
Figure B - 6.	Excitation Comparison of 1 μm DPN Patterned CNT Sample of NiCl <sub>2</sub> .....73
Figure B - 7.	Alternate Excitation Comparison of 2 μm DPN Patterned CNT Sample of NiCl <sub>2</sub> .....74
Figure B - 8.	Excitation Comparison of DPN Prepared CNT Sample of NiCl <sub>2</sub> Exhibiting an Anomalous Response Away from Deposition Site .....74

	Page
Figure B - 9. Bulk and DPN Prepared CNT Samples of PdCl <sub>2</sub> Observed with 633 nm Laser .....	75
Figure B - 10. Bulk and DPN Prepared CNT Samples of PdCl <sub>2</sub> Observed with 785 nm Laser .....	75
Figure B - 11. 785 nm Excitation of NiCl <sub>2</sub> Inkwell Dipped Tips .....	77
Figure B - 12. 785 nm Excitation of NiCl <sub>2</sub> Sample. Meniscus Dipped Tip and Cantilever Arm of the Scanning Probe. ....	77
Figure B - 13. 785 nm Excitation of NiCl <sub>2</sub> Bulk Deposited Samples on SiN <sub>3</sub> Compared to Bare SiN <sub>3</sub> .....	78
Figure B - 14. Comparison of 785 nm Excitation on Bare Substrate and on CNT Obtained from PdCl <sub>2</sub> Catalysts by Bulk and DPN Deposition on Sindex Substrate .....	78
Figure B - 15. 785 nm Excitation of CoCl <sub>2</sub> Bulk Deposited Samples on Si .....	79
Figure B - 16. 785 nm Excitation of CoCl <sub>2</sub> Bulk Deposited Sample on SiN <sub>3</sub> .....	79
Figure B - 17. 785 nm Excitation of CNT Obtained by Deposition of CoCl <sub>2</sub> Catalysts using Tip-to-Tip Deposition. (Responses Obtained Away from the Tip though Still Patterned - On the Cantilever Arm of the Scanning Probe - is Also Shown for Reference) .....	80
Figure B - 18. 785 nm Excitation after CVD on the NiCl <sub>2</sub> Catalysts Remaining on the Tip of the DPN Pen (Double Dipping Procedure) .....	80
Figure B - 19. 785 nm Excitation of PdCl <sub>2</sub> Inkwell Dipped CNT Formations. ....	81
Figure B - 20. 785 nm Excitation of NiCl <sub>2</sub> Bulk Deposited Sample on SiN <sub>3</sub> .....	81
Figure B - 21. 785 nm Excitation of CoCl <sub>2</sub> Bulk Deposited Sample on SiN <sub>3</sub> .....	82
Figure B - 22. 785 nm Excitation of PdCl <sub>2</sub> DPN Deposited Samples on SiN <sub>3</sub> .....	82
Figure B - 23. 785 nm Excitation of PdCl <sub>2</sub> DPN Deposited Samples on SiN <sub>3</sub> . The Figure Also Shows Anomalies Away from DPN Locations .....	83

	Page
Figure B - 24. Raman Spectra Obtained by 633 nm Excitation of PdCl <sub>2</sub> DPN Deposited Samples on SiN <sub>3</sub> . The Figure Also Shows Anomalies Away from DPN Locations.....	83

**LIST OF TABLES**

	Page
Table 1. DPN Depositions for Various Metal Salts on Sindex and SiN <sub>3</sub> Substrates .....	35
Table 2. Binding Energies for Elements Present on Metal Salt Samples.....	69

**NOMENCLATURE**

A	–	Contact area between tip and meniscus
AFM	–	Atomic Force Microscope/Microscopy
$C_0$	–	Concentration of ink solution adjacent to the tip
CNT	–	Carbon Nanotube
CVD	–	Chemical Vapor Deposition
D	–	Diffusion constant
$dN/dt$	–	Molecular transfer rate
$D_{\text{SWNT}}$	–	Diameter of SWNT
DI	–	Deionized (in reference to DI water)
DPN	–	Dip Pen Nanolithography
eV	–	Electron Volts
FET	–	Field-Effect Transistor
LFM	–	Lateral Force Microscopy
MEMS	–	Microelectromechanical Systems
MHA	–	16-mercaptohexadecanoic acid
MWNT	–	Multi-Walled Nanotube (in reference to CNT)
n	–	Diffusion rate of molecules from probe to surface
ODT	–	1-octadecanethiol
OPA	–	Octadecylphosphonic acid
R	–	DPN dot pattern radius



RBM	–	Radial Breathing Mode
RH	–	Relative Humidity
RMS	–	Root Mean Square
SEM	–	Scanning Electron Microscope/Microscopy
SWNT	–	Single-Walled Nanotube (in reference to CNT)
t	–	Time
TEM	–	Transmission Electron Microscope/Microscopy
v	–	Tip velocity / Write speed
W	–	DPN linewidth
XPS	–	X-ray Photoelectron Spectroscopy
XRD	–	X-ray Diffraction
$\rho$	–	Number density of DPN pattern
$\tau$	–	Contact time of tip to substrate
$\omega_{\text{G-band}}$	–	Frequency of Raman Shift where G band Appears
$\omega_{\text{RBM}}$	–	Frequency of Raman Shift where RBM Appears

## CHAPTER I

### INTRODUCTION

#### 1.1 Carbon Nanotube Synthesis

At the present state, production of carbon nanotubes (CNTs) has been accomplished\* via several techniques, both natural<sup>1,2</sup> and artificial; however, the primary means of obtaining “high purity” nanotubes is fairly limited. Two popular methods of synthesizing large quantities of CNTs include laser ablation of graphite rods and arc discharge which require a plasma source to induce the growth of nanotubes in the presence of catalysts (e.g. Pd, Ni, Co, etc.).<sup>3</sup> In 1991, carbon soot formed between two graphitic electrodes operating at 100 amps was found to contain nanotubes;<sup>4</sup> and later, this method of arc discharge was refined by Ebbesen, et al.<sup>5</sup> The high temperatures involved in the electric arc causes the carbon in the negative graphitic electrode to sublime and form hollow rods. The high yield for this method (up to 30%) allows for the macro-generation of tubes in measures of grams, which are comprised of a mixture of single-walled and multi-walled tubes up to 50 microns in length.<sup>6</sup> Guo, et al., first demonstrated laser ablated CNT formations by creating a target composed of graphite powder, carbon cement, and catalytic metal.<sup>7</sup> In the presence of argon gas flow, the resultant baked rod produces CNTs under incident laser irradiation when heated to approximately 1200°C. Carbon Nanotechnologies, Inc (CNI) in Houston alternatively utilizes a high-pressure carbon monoxide (HiPco) flow method in the presence of an

---

This thesis follows the style of *Nano Letters*.

electric arc - a procedure developed in 1999 - to generate larger amounts of single wall nanotubes (SWNTs) than the original plasma discharge methods.<sup>8</sup> Furthermore, chemical vapor deposition (CVD) provides another useful means of producing large quantities of nanotubes as first demonstrated by M. José-Yacamán *et al.*,<sup>9</sup> which has gained popularity due to the fact that CVD allows for synthesis of CNTs in the absence of vacuum, unlike the other popular methods. Using this method, a substrate coated with metal catalyst particles is heated near 700°C over which a carbonaceous gas (such as ethanol or acetylene) is introduced alongside a process gas (like nitrogen). The carbon in the reactor chamber collects on the metal catalyst from which tubes are formed as the atoms migrate along the surface of the metal particles. It has also been shown that application of a strong electric field which results in a plasma inside the reactor (known as plasma enhanced chemical vapor deposition) will generate CNT growth in the direction of the electric field.<sup>10</sup> Using this method, it is possible to obtain a sample of vertically aligned CNT by arranging the CVD reactor perpendicular to the substrate, a feat not reproducible using the other methods.<sup>6</sup>

Irrespective of the synthesis process (with the exception of arc discharge), in-situ TEM observations have shown that carbide precursors gather on the surface of catalyst particles (transition metals, typically Fe, Ni, Co, and intermingled combinations, among others) at which point rapid rod-formations occur on the catalyst metals, which are metastable carbide particles.<sup>11</sup> Following the appearance of these rods, graphitic structures form on the rod slowly, resulting in the final, hollow nanotube.<sup>11</sup> Studies<sup>12</sup> have suggested that this rapid rod-forming process is the result of the carbon extruding from

the catalyst particle labeled "base (or root) growth" and "tip growth" depending on whether the metal particle remains at the base or moves at the end of the tube proceeding forth from the substrate, respectively. These models suggest, which has been validated,<sup>13</sup> that the size of the catalyst particles play a direct role in the diameter of the synthesized CNTs, for which it appears that the chirality (orientation of hexagonal bonds comprising tube wall) of the formed nanotubes are somewhat dependent on the tube diameter. This is of particular interest, since the chiral behavior of CNT determines the electrical properties of the tube, where it may be either conducting or semi-conducting; and, furthermore, theory has indicated that a conducting CNT can handle 1,000 times the current density of conventional conductive materials like copper or silver.<sup>6</sup> Additionally, a nuclear magnetic resonance study of SWNT formations by Wu, et al., showed that changing the catalyst composition in a laser ablation target and by increasing the exposure to oxygen resulted in varying proportions of metallic nanotubes in the synthesized CNT sample.<sup>14</sup> According to the authors, these results "indicate that the chirality distribution in SWNT samples is not always random and might be controllable by synthesis conditions."

## **1.2 Carbon Nanotube Characterization**

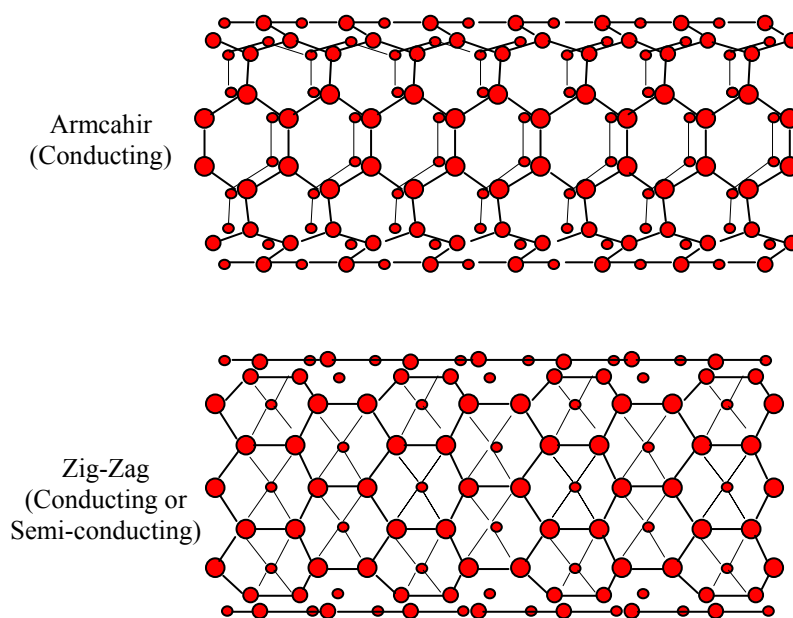
Among many of the various techniques used for the evaluation of CNTs and their properties, Raman Spectroscopy has emerged as a prominent method for verification of tube presence when imaging is difficult to obtain, as well as for the determination of structural characteristics.<sup>15,16</sup> In the presence of the laser excitation, the CNTs can

exhibit three very distinct resonance peaks, each representing a different tube feature. The first observed peak (or set of peaks) is called the "radial-breathing mode" or RBM (sometimes, RB mode), whose Raman shift is observed in the range of roughly 50 - 400  $\text{cm}^{-1}$ . The reason for this nomenclature is explained by the fact that this peak is the result of the radial pulsing of the tube cylinder which perhaps mimics the expanding and contracting of a lung during breathing. Because the relationship seen between the shift location of this peak and the diameter of the tube, Dresselhaus developed the following empirical correlation for the determination of SWNT diameters from Raman information.<sup>17</sup>

$$D_{SWNT} = \frac{248}{\omega_{RBM}} \quad (1)$$

Here,  $D_{SWNT}$  is the diameter of the SWNT in nm, and  $\omega_{RBM}$  is the Raman shift location of the observed peak in  $\text{cm}^{-1}$ . The two other typically observed peaks are the D and G bands, which occur near 1300 and 1600  $\text{cm}^{-1}$  respectively, and which refer to the disorder (D) and graphitic (G) structure of the CNT sample. Prior to Dresselhaus, a study by Eklund, et al., calculated the numerator in this equation to be 223.8 nm/cm when predicting the theoretical behavior of the rolled graphitic structure.<sup>18</sup> Other authors have noted the use of 234 nm/cm,<sup>19</sup> as well; however, the value of 248 nm/cm as found by Dresselhaus, et al., has been exclusively used in a variety of recent studies. This formula is only valid for tube diameters ranging from 1 to 2 nm. Since the size of these peaks are a statistical representation of the concentration of these features in the sample, a Raman response with a D-band larger than the G-band typically reflects that

the sample is predominantly multi-walled. In other words, an entirely single-walled tube sample will show little or no evidence of this peak. The G-band alternatively provides insight into the chiral nature of the tube. This "chirality" refers to the orientation of the hexagonal carbon-carbon bonding patterns that are seen in CNTs. Depending of the angle described by the (n,m) indices, the CNTs may be either conducting or semi-conducting. Chiral angles resulting in an "armchair" pattern are "metallic" (where  $n - m$  equals a multiple of 3); those exhibiting the "zig-zag" pattern can either be conducting (1/3 of n, m combinations) or semi-conducting (2/3 of (n,m) combinations). The remaining index combinations in between armchair and zig-zag are referred to as "chiral" and are semi-conducting. Figure 1 is a schematic of these two CNT types, where the origins of the names for these types are seen in the shapes made at the end of the open tubes. When the chiral bond angles of the tube are aligned in such a way that



**Figure 1. Armchair and Zig-Zag Type CNT Chiralities**

results in a "metallic" tube sample, the G-band will shift to a lower Raman shift frequency than seen in semi-conducting samples.<sup>20</sup> Essentially all CNT samples exist in a mixture of all chirality types with diameters varying within a certain range, and therefore, Raman is most often used for classifying the statistical distribution of the presence of these tube types.

### **1.3 Research Motivation**

Despite the continuing research revolving around CNT formation, several barriers still remain before CNTs can unveil their full potential in technology that researchers predicted in 1990's.<sup>6</sup> Applications of CNTs have been envisioned in superconductors and field-effect transistors (FETs) for use in sub-microelectronics, MEMS, and sensors, depending on whether the CNTs are conducting or semi-conducting.<sup>21</sup> However, the current production methods result in large amounts of amorphous carbon and soot in proportion to the actual number of CNTs formed (i.e. the production density is inadequate). Also, the synthesized CNTs have non-uniform distributions of diameter, length, and chirality. More than that, often batches of reportedly SWNTs contain MWNTs, indicating that even controlling the type of nanotube formations is inconsistent with traditional synthesis.<sup>22</sup> Li, et al.,<sup>13</sup> presented encouraging results showing that the use of iron (III) oxide nanoparticles of semi-controlled diameters led to fairly consistent nanotube diameters located at the discrete positions where the nanoparticles were "planted." Yet this method, among the rest, are incapable of growing CNTs at precisely defined locations, being that the introduction of catalyst particles is accomplished in

bulk. Generally, for the nanotubes to be efficiently utilized, separation processes<sup>23,24</sup> and nano-manipulation techniques must be employed, which can be extremely costly and time consuming and often lead to damaging or altering of the properties of the original sample.<sup>25</sup> Therefore, it is desirable to have a means of CNT synthesis leading to a controlled size and chirality, and which has the ability to precisely locate the growth of the nanotubes for functionalization in applications like FET's. With this ability, it is conceivable that an entire nano-circuit board could be grown!

#### 1.4 Dip Pen Nanolithography

Since its emergence as a robust means of nano-plotting in 1999,<sup>26</sup> Dip-Pen Nanolithography (DPN) has gained much attention for its unique registration capabilities at the nanoscale. Akin to its age-old analog of an ink quill, DPN accomplishes its nanopatterning via the transport of chemical "inks" from the tip of an atomic force

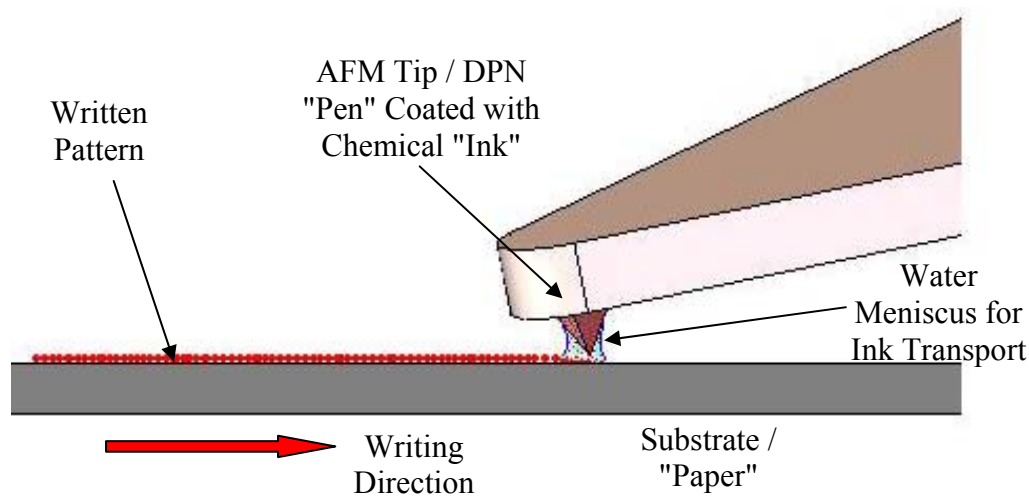


Figure 2. Schematic of DPN "Ink" Deposition



microscope (AFM) scanning probe (the nib) onto a substrate (often Au film), sometimes referred to as "paper," as depicted in the schematic in Figure 2. However, a significant limiting factor in the direct write capabilities of DPN is the inability to precisely and repeatedly deposit an "ink" on surfaces exhibiting uneven features or having greater than a critical surface roughness since the resultant pattern is often only a molecule thick.<sup>26</sup>

Studies have shown that this molecular transport is largely the result of diffusion across a concentration gradient, that is facilitated by means of a water meniscus that forms on contact of the nib with the paper in the presence of sufficient humidity.<sup>27,28</sup> However, some argument has arisen to the nature of the meniscus formation due to contradicting studies. Weeks and Vaughn used environmental scanning electron microscopy to observe the formation of water menisci at the tip of a silicon nitride probe in contact with either silicon or gold surfaces. Here, they observed that a meniscus does not form until the relative humidity (RH) is increased above 70%, from which point it grows (by height) at different exponential rates, depending on the substrate material. They also observed significant hysteresis in which the menisci did not disappear until the relative humidity was decreased below 40%.<sup>28</sup> When attempting to deposit MHA (16-mercaptohexadecanoic acid) onto a gold substrate, Weeks, et al., observed pattern transfer at humidity as low as 15% RH, and found that the resultant feature size is more dependent on the humidity than on the dwell time of the tip on the substrate.<sup>29</sup> However, several clear examples of the effect of dwell time and/or tip speed in lateral force mode have been shown to be proportional to the feature size.<sup>26,29,30,31</sup> In light of the disparities seen in the "required" amount of humidity for ink delivery, Hörber, et al., sought to

explain this phenomena when scanning tunneling microscopy measurements led to the discovery of adsorbed water in the surface of a substrate even at very low humidity, which may lead to the formation of a meniscus in a "dry" environment.<sup>32</sup> Additionally, Mirkin, et al., observed meniscus formation at 0% RH on the surface of a NaCl substrate by means of an observed recrystallization induced by presence of water, which is attributed to "residual water" that migrates toward the tip during contact.<sup>33</sup> They also observed the growth rate of ODT (1-octadecanethiol) patterns to be independent of humidity while MHA showed significant increase with humidity. Sheehan and Whitman also noticed this independence of humidity for the DPN deposition of ODT, for which they surprisingly deposited ODT at 0% RH after holding the substrate and pen in a dry nitrogen environment for several hours, claiming a water meniscus is unnecessary for chemical transport.<sup>31</sup> In the dry nitrogen environment, they further observed a surface diffusion of the ODT on gold of  $8400 \text{ nm}^2/\text{s}$ . Similarly, Schwartz observed the DPN of ODT onto a gold substrate in a dry nitrogen environment, a humid environment, and an ethanol vapor environment, claiming that meniscus formation is irrelevant to transport in the pure sense (i.e. it affects molecular distribution, but is not the driving agent) because "the molecules are individually mobile."<sup>27</sup> Weiss, et al., sought to explain the observed differences between the diffusion of MHA and ODT on a gold substrate by studying the deposition of the two inks at the same location. They observed a migration of ODT to the boundaries of the previously deposited MHA, for which no apparent mixing occurred. Furthermore, the MHA did not exhibit different transport behavior when patterned on top of itself, while ODT's transport rate decreased when attempting to

transport on top of another ODT pattern. These results indicated that the molecules travel across the top of any preexisting self-assembled monolayer deposition from the AFM tip, for which the substrate or chemical species upon which the deposition is made directly affects the rate of transport.<sup>34</sup> Furthermore, the behavior of the ink depositions is explained by the hydrophilic nature of MHA in contrast to the hydrophobic nature of ODT. When patterning ODT on top of MHA, the water meniscus spreads over the surface of the MHA pattern, facilitating quick transport of the ODT molecules to the periphery of the previous deposition. In contrast, the meniscus contacting the ODT pattern becomes more compact (or does not even form) resulting in no MHA migration to the edges of the ODT.<sup>34</sup> This also explains the phenomena of "phase separation" observed by Mirkin, et al., when attempts to pattern a binary mixture of MHA and ODT led to distinct separation of the two compounds when deposited on the surface of gold.<sup>35</sup>

In addition to factors of humidity, meniscus formation and dwell time of the tip, other factors have also been studied. De Yoreo found that contact force did not play any role in the feature size of deposited compounds. It was discovered that the capillary force induced by the incident water meniscus was significantly larger than the force applied by the AFM such that the contact pressure is essentially uniform despite any load applied.<sup>29</sup> Mirkin and Hong also discovered less than 10% variation in feature size of ODT on gold when subjected to varying contact forces by up to 40 times.<sup>36</sup> Piner, Rozhok and Mirkin additionally found a significant dependence on temperature of the diffusion rate from the DPN pen.<sup>33</sup> Using this premise, Sheehan and Whitman demonstrated the selective DPN of octadecylphosphonic acid (OPA), whose melting

point is near 100°C, by using a thermally active AFM probe to heat the OPA above its melting point during deposition. This technique, deemed "thermal dip pen nanolithography," is significant because it allows for the avoidance of pattern contamination - a significant problem in typical DPN molecular transport - during scanning by simply removing heat from the tip.<sup>37</sup>

Several attempts to model the diffusion from the DPN tip have also been studied. In the transport behavior as suggested by Weiss et al.,<sup>34</sup> Hong, et al., developed a molecular transport model assuming that every lattice site of the substrate traps an "ink" molecule, above which any additional ink molecules diffuse until reaching an available lattice site.<sup>38</sup> The developed solution to the size of a deposited dot with respect to time is the combination of the diffusion from the tip to the surface (the slow deposition limit) and the diffusion of the molecules once deposited on the surface (the fast deposition limit). The resulting equation is a time dependent proportionality relation comprised of the following equations:<sup>38</sup>

$$\text{Slow Deposition Limit:} \quad R(t)^2 = \frac{n}{\pi\rho} t \quad (2)$$

$$\text{Fast Deposition Limit:} \quad R(t)^2 = 4D \cdot t \ln\left(\frac{n}{\pi\rho 4D}\right) \quad (3)$$

In these equations  $R(t)$  is the radius of a dot as a function of time,  $n$  is the diffusion rate from the probe in molecules per unit time,  $\rho$  is the number density of the monolayer deposition ( $\text{area}^{-1}$ ),  $t$  is time, and  $D$  is the diffusion constant. Alternatively, Weeks and De Yoreo observed a transitional diffusion behavior for which they attributed to two primary regimes: kinetic motion through the meniscus followed by diffusion across the

surface of prior deposited material. From these suppositions, the following semi-empirical models for deposition size of dots and lines were developed.

$$\text{Dots:} \quad R^2 = A \left[ \beta_+ \tau - \pi \alpha^2 \beta_- \int_0^\tau C_o(t) dt \right] \quad (4)$$

$$\text{Lines:} \quad W = \left( \frac{A}{v} \right) \left[ \beta_+ - \pi \alpha^2 \beta_- C_o(v) \right] \quad (5)$$

Where,

$$\left( \frac{dN}{dt} \right)_+ = \left( \frac{A}{\pi \alpha^2} \right) \beta_+ \quad \text{and} \quad \left( \frac{dN}{dt} \right)_- = A \beta_- C_o \quad (6, 7)$$

In these models, R is the dot radius and W is the line width, A is the contact area between the tip and the meniscus,  $\pi \alpha^2$  is the average area of an "ink" molecule,  $\tau$  is the total contact time of the pen to the surface,  $C_o$  is the concentration of ink in solution adjacent to the tip, v is the tip writing speed,  $dN/dt$  is the transfer rate, and the positive

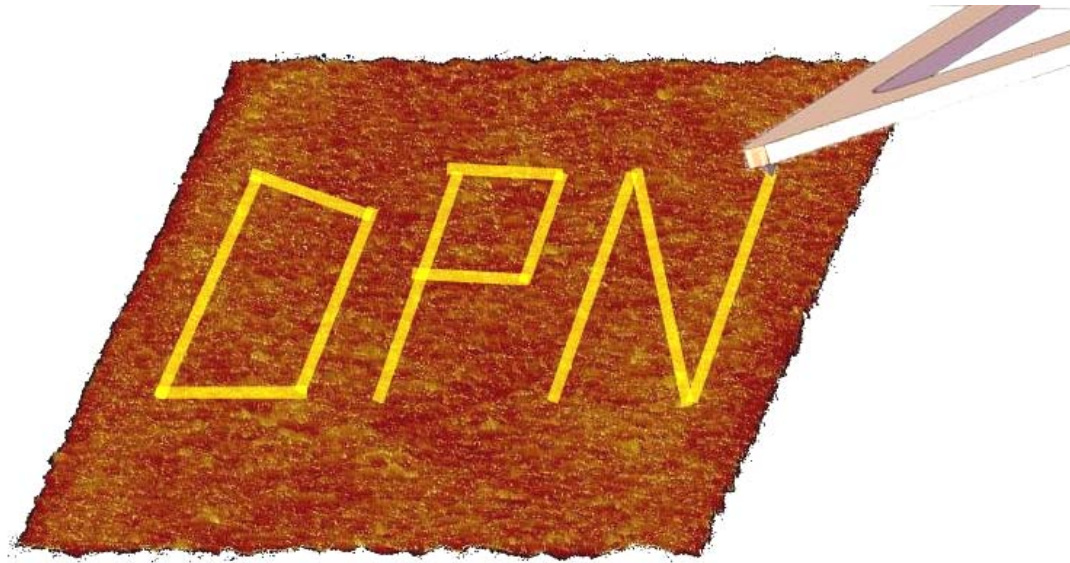


**Figure 3. Schematic Explaining Registration Capability of DPN**

and negative subscripts refer to diffusion away and toward the tip surface, respectively. However, these models are developed in the specific cases of the inks/surfaces used for specific circumstances and neglect to explain other types of diffusive behavior. For instance, a study by Mandahar found some chemicals (e.g. 1-dodecylamine on mica) to diffuse in fractal patterns rather than the typical linear diffusion.<sup>30</sup> Similar nano-fractals were also observed during patterning of poly-ethylene glycol on gold coated silicon substrates by Rivas-Cordona and Banerjee.<sup>39</sup>

One of the distinct advantages of DPN is its ability to create monolayer deposits of molecular compounds in virtually any two dimensional pattern imaginable (or programmable, for that matter). Figure 3 (previous page) depicts a schematic of the

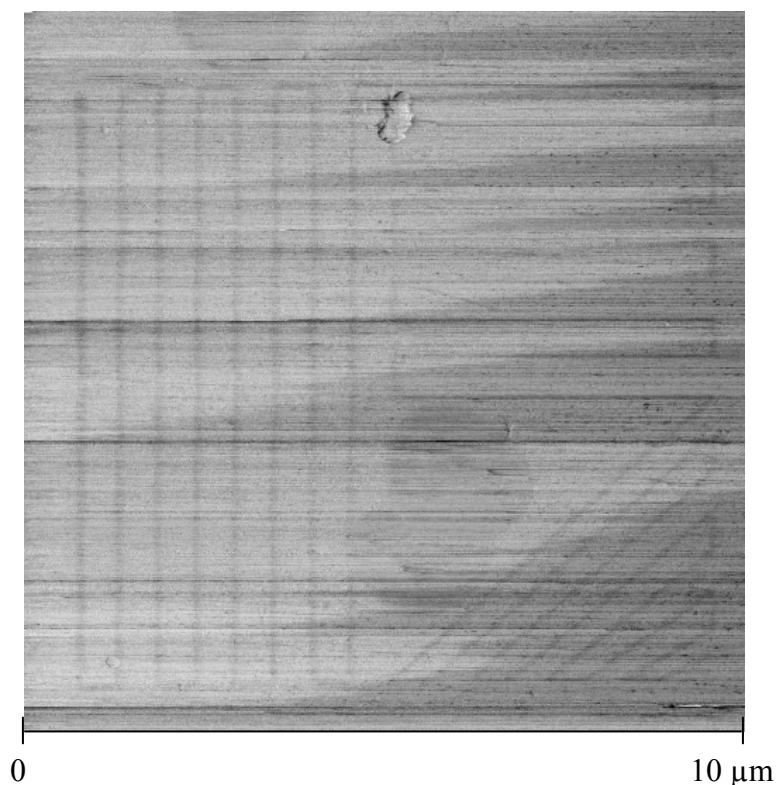


**Figure 4. DPN of MHA 75 nm Line Array on Gold Substrate**

ability of DPN to even deposit text due to its high registration capabilities. Figure 4 provides an actual scan of an array of MHA lines patterned on a gold substrate. The lines are 75 nm thick. Moreover, Hong, et al., showed the ability of DPN to deposit multiple "inks" (MHA and ODT) in overlaid and adjacent patterns.<sup>40</sup> In fact, DPN has been shown to be capable of writing with almost any ink, provided it being in correct combination with an appropriate substrate.<sup>26, 41,42,43</sup> Furthermore, Zhang, et al.,<sup>44</sup> showed the applicability of DPN in mass fabrication, through the development of a multiple pen, parallel ink delivery MEMS nanoplotting system for use with DPN. Mirkin and Hong demonstrated parallel DPN capabilities using this type of probe array.<sup>36</sup> DPN has been touted for its potential applicability in molecule-based electronics<sup>40</sup> and magnetic storage devices and nano-magnetic biosensors,<sup>45</sup> but has attracted perhaps the most attention in regards to the biomolecular nanoarrays that can be generated using DPN.<sup>46</sup> Advances in this field may feasibly lead to the ability to identify single nucleotide polymorphisms in a screening of the entire human genome on one chip, according to E. S. Lander.<sup>47</sup> Yet despite DPN's appeal for positive print nanolithography, its use in the nanodeposition of catalyst particles for CNT synthesis has been overlooked. In this paper, we introduce DPN as an effective means of controlling the size, characteristics and location of CVD synthesized CNTs through the strategic placement of metal catalysts.

## CHAPTER II

### DESCRIPTION OF EXPERIMENTAL APPARATUS

#### 2.1 Introduction to Experimental Apparatus

The scope of this project required the use of several nanoscopic techniques and evaluation methods, since the elements of the study required the nano-precise articulation and observation of features smaller than the visible spectrum. The following sections describe the elements used in the deposition and manipulation of samples, the substrates upon which samples were prepared, the low-temperature CVD furnace used

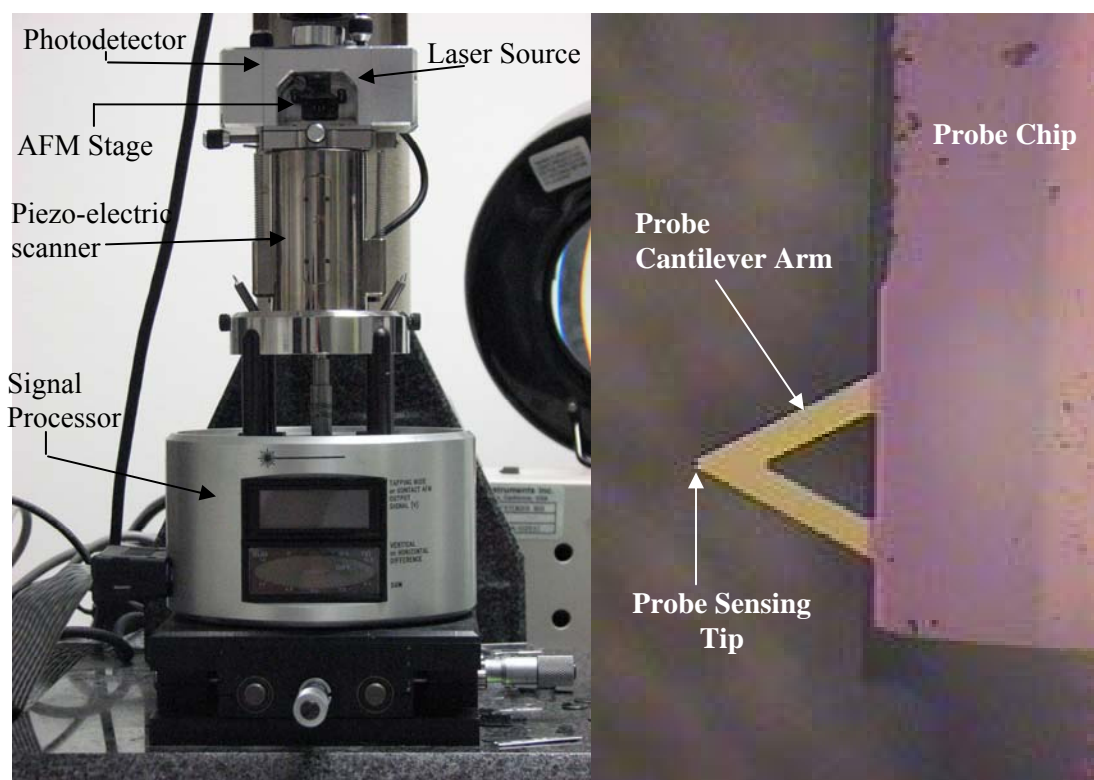


Figure 5. Digital Instruments Nanoscope IIIA Atomic Force Microscope (Left) and Veeco Silicon Nitride AFM Probe (Right)



for synthesizing the CNT and the equipment required for the evaluation of the samples post-processing.

## 2.2 Deposition and Manipulation

The patterning capabilities of Dip Pen Nanolithography were made possible through the precise manipulation control of an atomic force microscope. For the DPN work, AFM and LFM measurements taken for this study, a Nanoscope IIIA (using the J scanner; Digital Instruments) was used in conjunction with silicon nitride AFM probes (Veeco). These probes are gold backed for improved signal, and have four tips of various stiffness (Veeco product #: DNP-20). When patterning, typically the 0.58 N/m tip was used, although all tips are capable of DPN ink deposition. Figure 5 on the previous page shows the AFM experimental setup, as well as an image of the scanning probes utilized.

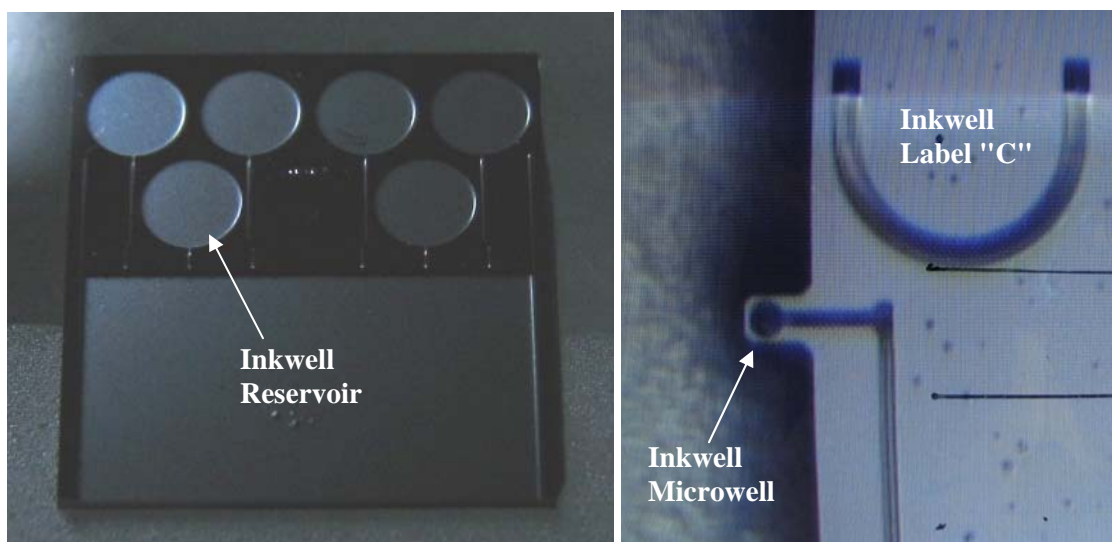


**Figure 6. Inkwell Chip (left) and Microscope Image (8x) of Individual Inkwell**

The AFM was also used to dip the tips of the AFM probes (used as samples) into the microscopic reservoirs of metal salt solutions on Inkwell chips (NanoInk, Inc. – see Figure 6, previous page), for precision in salt delivery.

Bulk samples were prepared by hand using 1 mL syringes with 20 gage needles for the delivery of the salt solutions onto either silicon nitride ( $\text{SiN}_3$ ) membranes, silicon wafers, or the AFM probes.

## 2.3 Substrates

### 2.3.1 DPN Samples

When performing DPN depositions, three primary substrates were used. First, a gold-filmed silicon wafer, with a 15x15 array of 100  $\mu\text{m}$  by 100  $\mu\text{m}$  etched mesas called a Sindex chip (Bioforce Nanosciences, see Figure 7) was used as a test substrate to verify the patterning capability of the DPN pens coated with the metal salt solutions. Its

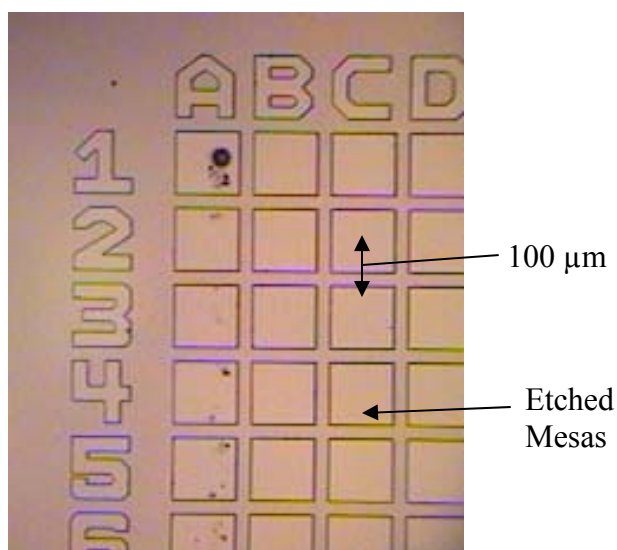


**Figure 7. Sindex Chip Surface**

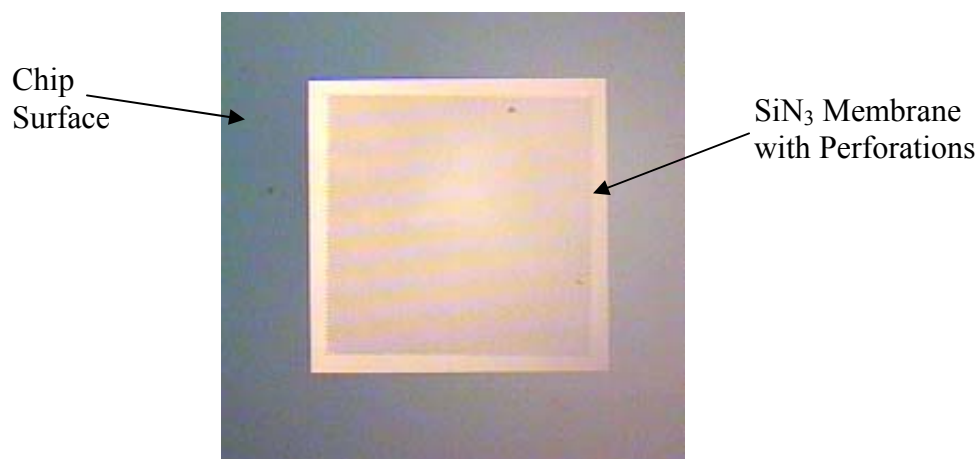


**Figure 8. Magnified Image of SiN<sub>3</sub> Perforated Window Grid**

superior surface smoothness (RMS roughness  $\sim 0.2$  nm) made it an excellent choice over the substrates used in processing, since their surface features often made it difficult to easily identify patterned material. Having thus verified, SiN<sub>3</sub> membrane TEM window grids (SPI Supplies), both perforated (2  $\mu\text{m}$  holes at 5  $\mu\text{m}$  spacing) and non-perforated, were used for patterning. A magnified image of a perforated membrane is shown in Figure 8. These samples allowed for TEM verification of growth of CNT due to having a thickness of only 50 nm yet they maintain sufficient stiffness to endure the patterning process. DPN patterns were also made on the tips of alternate AFM probes. Using the same probe type (Veeco # DNP-20), these sample probes were mounted on AFM pucks using either two-sided adhesive or melted candle wax. The two widest cantilever probes (stiffness values of 0.58 and 0.12 N/m) were patterned upon, using the AFM imaging software to identify when the apex of the probe tip was reached. This process was dubbed “tip to tip DPN.” Some of the tips used as samples in this process were prepped

by sputtering with a Au-Pd target until a good coating on the probe was observed. This was done to aid in the SEM imaging by reducing charging of the sample.

### 2.3.2 Bulk Samples

As a control to the DPN experiments, bulk samples were also prepared by hand using all of the same substrates mentioned above, as well as on broken pieces silicon wafers which were used in XPS analysis.

## 2.4 CVD Furnace

The CVD system utilized in the synthesis of CNTs for these experiments is pictured in Figure 9, which was generously provided by Dr. S.K. Sinha of the University of New Haven. It consists of an electric furnace that encapsulates a Pyrex glass tube where the sample is placed. A thermocouple monitors the temperature inside the tube where



Figure 9. CVD System (Courtesy of S.K. Sinha, UNH)

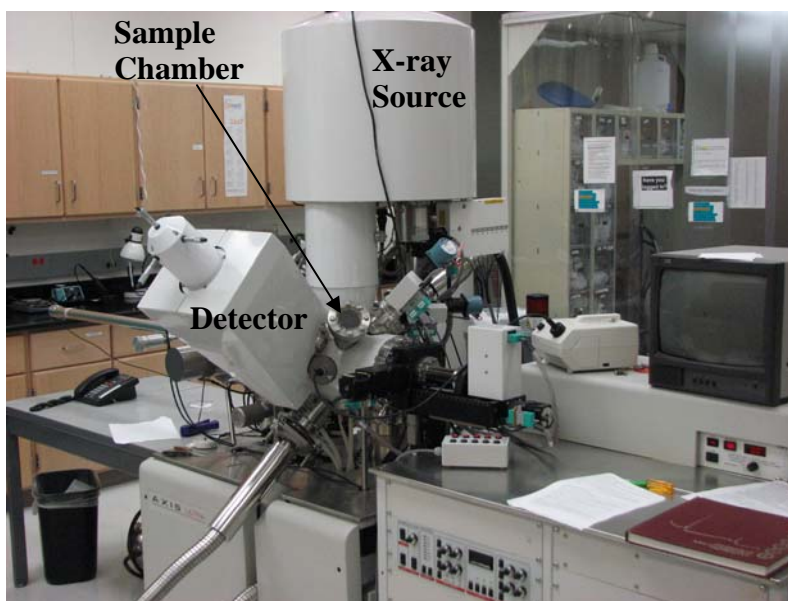


**Figure 10. Kratos Axis Ultra Imaging XPS**

vaporized alcohol and argon flow resulting in the deposition of carbon onto the sample. The flow of the vapor is controlled using an infusion pump and positive pressure is maintained using argon.

## **2.5 Verification and Evaluation**

Both before and after CVD processing, the samples were evaluated using various techniques, including X-ray Photoelectron Spectroscopy (XPS), Transmission Electron Microscopy (TEM), Scanning Electron Microscopy (SEM), Raman Spectroscopy, as well as AFM and LFM. XPS was performed using a Kratos Axis Ultra Imaging X-ray Photoelectron Spectrometer (Figure 10), equipped with dual aluminum-magnesium sources. TEM was performed with a JEOL 2010 TEM operating at 200 kV, shown in Figure 11. SEM was performed at different locations, using Environmental SEM's

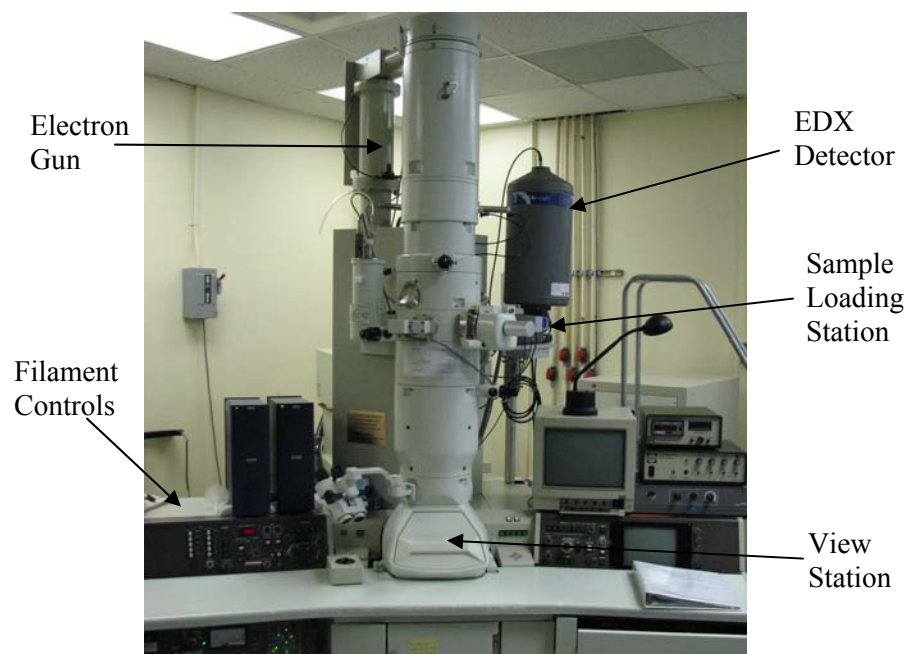


**Figure 11. JEOL 2010 Transmission Electron Microscope**

(ESEM) at Rice University and at the Materials Directorate of the Air Force Research Laboratory on Wright-Patterson Air Force Base in Dayton, Ohio. The latter was

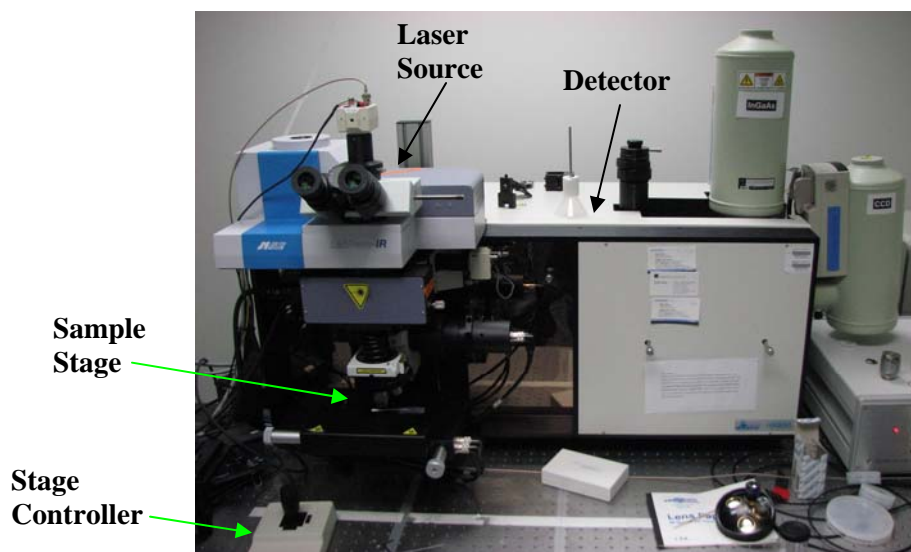


**Figure 12. JY Horiba LabRam IR Raman Spectrometer**

equipped with an EDAX Electron Dispersive X-ray Spectrometer (EDX), which was used for chemically characterizing microscopic material. Raman spectroscopy measurements were made using a JY Horiba LabRam IR Raman/FTIR Spectrometer (Figure 12), in conjunction with the JY Open Electrode CCD detector for excitation laser wavelengths of 633 and 785 nm.

## CHAPTER III

### EXPERIMENTAL PROCEDURE

#### 3.1 Sample Preparation

##### 3.1.1. DPN Pen

The DPN pens (SiN<sub>3</sub> AFM tip – 0.58 N/m, Veeco) were coated with metal salt solutions of which the cation was one of the known catalyst metals for CNT synthesis. NiCl<sub>2</sub>, CoCl<sub>2</sub>, PdCl<sub>2</sub>, FeCl<sub>2</sub>, FeCl<sub>3</sub>, PtCl<sub>2</sub>, and RhCl<sub>3</sub> were dissolved to form 0.05 M aqueous solutions, which were used in the double dipping procedure recommended by NanoInk, Inc. This procedure involves immersing the tip of the AFM probe into the “ink” solution for 5 – 10 seconds, followed by using ~ 10 psi of compressed nitrogen to gently blow off any droplets remaining on the surface of the probe. During this procedure the nitrogen flow was maintained at an angle less than 30 degrees from the cantilever arm to prevent damage to the probe. Next, deionized (DI) water was evaporated onto the surface of the probe by suspending the probe above DI water that had been heated to the point that condensation appeared on the sidewalls of its container. Once a visible film of condensed water was observed, the probe was removed and left to air dry for approximately 5 minutes; then the entire procedure was repeated to ensure proper coating of the “ink.” Additionally, 50/50 mixtures of the NiCl<sub>2</sub>/ CoCl<sub>2</sub> solutions and RhCl<sub>3</sub>/PdCl<sub>2</sub> solutions were used as inks. All salts except RhCl<sub>3</sub> are water soluble, which required the addition of NaOH to the solution by roughly 6% by weight, since RhCl<sub>3</sub> is soluble in alkali hydroxide solutions.



### 3.1.2. DPN Patterning

To generate DPN patterns, an atomic force microscope was used to manipulate the "nib" after the dipping process (Nanoscope IIIA, Digital Instruments). However, this particular model is open to the atmosphere, and therefore, the humidity often needed to be increased by creating a semi-closed environment using a plastic envelope around the AFM into which water vapor was introduced in the form of saturated steam by boiling water from a beaker. If the ambient relative humidity was observed to be 40% or greater, this apparatus was not necessary, qualifying the claims of previous studies into meniscus formation.<sup>27,28</sup> To verify DPN patterning, the pens were first used to pattern on the Sindex chips before patterning on the SiN<sub>3</sub> TEM window grids, where patterns were not as distinguishable due to an increased surface roughness. These particular grids were chosen for their stiffness for enduring the forces present during DPN, while still allowing for TEM imaging. During writing, the tip speed of the pen was maintained at less than 2  $\mu\text{m/s}$ . Square patterns of 1  $\mu\text{m}$ , 500 nm, 200 nm, 100 nm, and 30 nm were attempted for each metal salt. Verification of the deposited patterns was accomplished using lateral force microscopy (LFM) at an increased scan rate, usually greater than 60  $\mu\text{m/s}$ . LFM is more indicative of the presence of a monolayer deposition since it measures surface friction instead of height, being that the layers are usually less than a nanometer in height but the presence of a different substance changes the friction of the surface considerably. An example of this verification method is exhibited in Figure 13, showing a 1  $\mu\text{m}$  square deposition of PtCl<sub>2</sub> solution onto a SiN<sub>3</sub> membrane. In this image, the friction observed by the scanning probe is lower where the deposition took

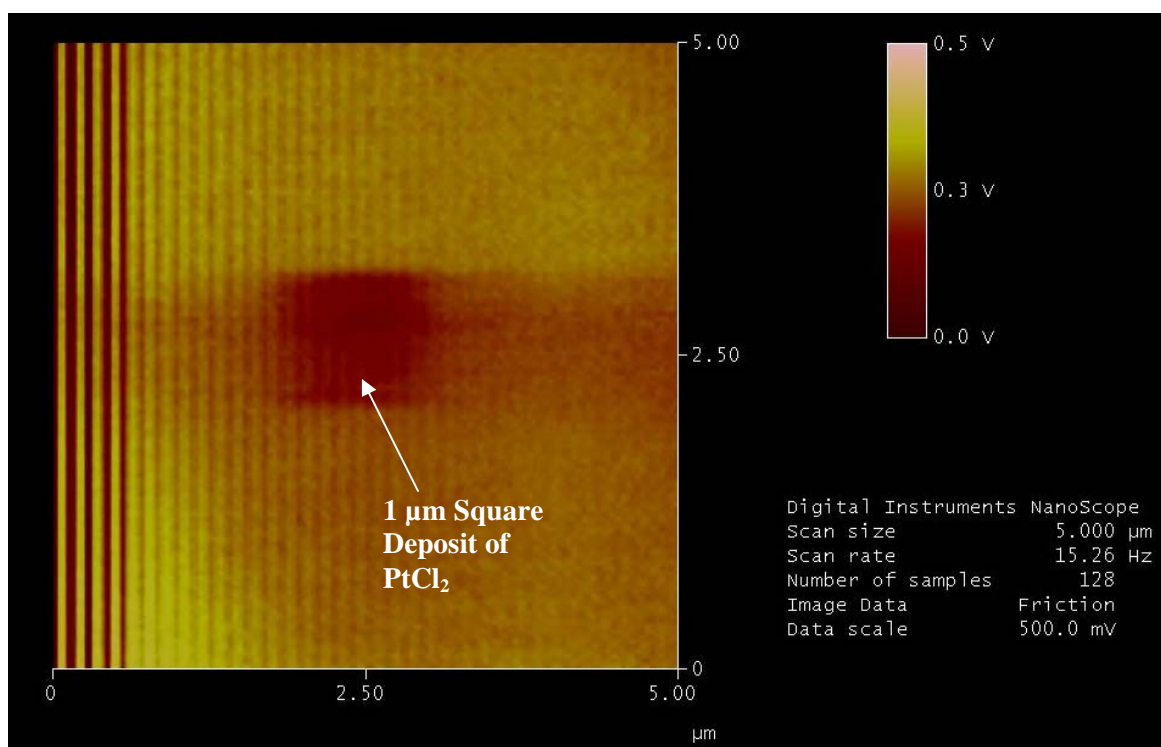


**Figure 13. LFM Image of  $\text{PtCl}_2$  DPN on  $\text{SiN}_3$**

place due to the monolayer salt solution. The vertical lines present in the image are a result of the probe tip "skipping" across the surface at the beginning of its lateral scan. This occurs during rapid scans due to the static friction that occurs at each reversal of motion (this effect can be reduced using a less stiff probe), for which it can be seen that the scan shown above is reading left to right.

The same scanning parameters were followed when attempting "tip to tip DPN" depositions, where a coated DPN pen would be used to write directly onto a clean AFM probe tip. A schematic representation of this process is shown in Figure 14. A scan size of 2  $\mu\text{m}$  would be used while trying to coat the tip whose base was 5  $\mu\text{m}$  across. To

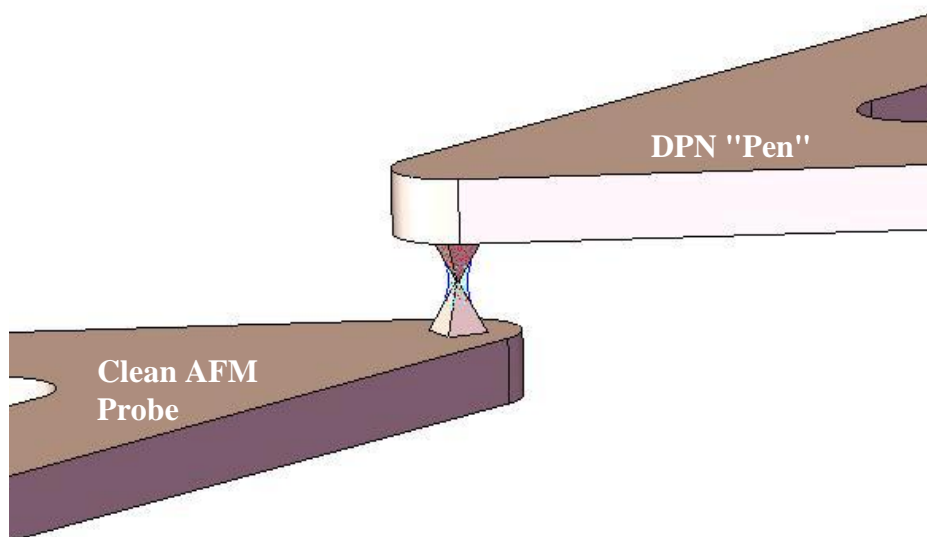


**Figure 14. Tip-to-Tip Schematic**

verify that the tips were in contact, the cantilevers would first be aligned under a microscope and then using the AFM software to gradually adjust the placement of the

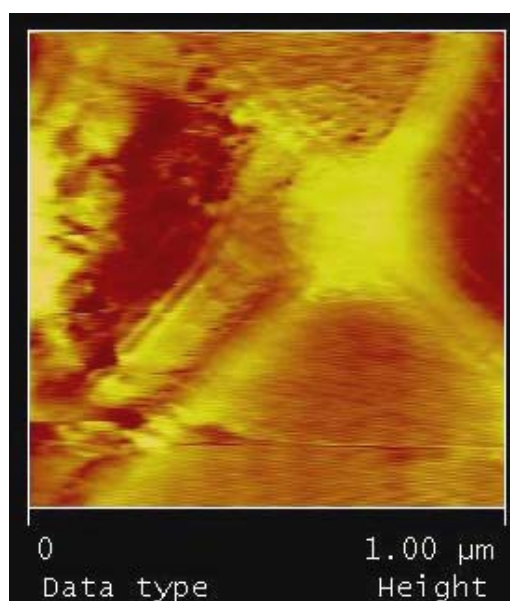


**Figure 15. AFM Scan During "Tip 2 Tip" Deposition for Verification of Probe Placement**

pen until the AFM scan measured the probe's presence. Figure 15 shows a scan during a tip to tip deposition, in which the tip can be seen by the "X" made by the four edges of the probe prism.

### 3.1.3. "Bulk" Prepared Samples

In addition to the depositions of the metal salts using DPN, bulk depositions were made on the SiN<sub>3</sub> grids and AFM probes as experimental controls to gage whether DPN offered any direct advantage. Droplets of each solution were deposited on both the membranes and the AFM probes using a syringe. Additionally, to increase the control during this process for the AFM probes, Inkwell reservoirs were filled with the solutions and then transferred onto the probe tips by dipping the probes into the inkwells using the AFM stage controller to manipulate the tip.

## 3.2 CVD Synthesis

The synthesis of CNTs from these DPN patterns was accomplished using a novel method of CVD, developed by S. Sinha, which allows the CNT growth to take place at 500°C using ethanol as a precursor. This technique offers the advantage of CNT synthesis being achievable at a lower temperature instead of temperatures greater than 650°C, which are typical of other methods.<sup>48</sup> The CVD system utilized in these experiments is pictured in Figure 9 in section 2.4. After mounting the DPN and bulk samples with the metal salt deposits, the CVD system was purged with argon for 30 minutes. The furnace and hotplate were heated such that the furnace temperature was slowly increased to 500°C (the slow rate is necessary to avoid sudden spikes in

temperature, which can lead to the softening of the Pyrex glass tube). A thermocouple, calibrated for measuring the internal flow temperature, was used to monitor the temperature during synthesis. A thermally insulated flask located on the hotplate was injected with liquid ethyl and methyl alcohols, for which the flow rate was controlled using an infusion pump. Positive pressure in the tube was maintained by continuous flow of argon as it mixed with the vaporizing alcohol. The amount of carbon free radicals generated in the process was controlled by varying the respective flow rates of argon and alcohol. After completing the synthesis, to avoid the oxidation of the CNT samples, the argon flow was held constant until the system cooled below 200°C.

### **3.3 Evaluation**

#### *3.3.1 XPS*

The bulk samples were chemically characterized with x-ray photoelectron spectroscopy (XPS) in order to verify the composition of the deposition before and after the CVD process. The XPS data for the samples deposited by DPN had low signal to noise ratio since the amount of deposited materials was incredibly small, and thus could not be used in this analysis. A basic survey for binding energies between 1,100 and 0 eV was obtained using either the Mg source with the anode operating at 12 mA and 15 kV or the mono Al source operating at 10 mA and 12 kV (used during a period when the Mg source was out of commission). Additionally, the carbon content was explicitly evaluated by scanning the C 1s binding energy region between 295 and 275 eV.

### 3.3.2 XRD

The bulk samples were also characterized with x-ray diffraction (XRD) in order to verify the presence of CNT according to their structural XRD signature after the CVD process. The XRD was hoped to be used as a method for determining chirality as well, but poor evaluation led to the discontinuation of its use as a characterization device.

### 3.3.3 Raman

After completing CNT synthesis on the metal salt samples, the CNTs grown on the substrates were characterized using Raman spectroscopy (at both 633 and 785 nm wavelength laser excitations). Although variations in samples required different scan parameters, typical settings were as follows:

Scan Range:	50 to 2,000 $\text{cm}^{-1}$
Microscope Obj:	100x
Exposure time:	3 s
Accumulation #:	5
Grating:	300
Confocal Hole:	200 $\mu\text{m}$
Filter:	D 0.6

### 3.3.4 TEM/SEM

In addition to spectral information, direct measurements and verifications were made using TEM and SEM. The  $\text{SiN}_3$  membrane samples were evaluated in the JEOL 2010 TEM, while samples prepared on AFM probes were evaluated with various SEM techniques. Energy Dispersive X-ray Spectroscopy (EDX) in conjunction with SEM

was also performed on a few samples for verification of chemical components where XPS lacked the ability to measure at microscopic levels. This evaluation was performed using a 15 kV acceleration voltage at 50,000 x magnification. The EDX detector was Silicon/Lithium exposed for 50 seconds.

### 3.3.5 LFM

While LFM techniques were primarily used in the verification of and deposition of catalyst material through DPN, certain samples could not be readily evaluated under TEM/SEM. Therefore, LFM was also used as a measure to verify the presence of deposited material and/or CNT after the CVD processing of the samples. This technique was primarily reserved for samples prepared on silicon wafer fragments or Sindex chips. For this stage of measurement, the 0.12 N/m (wide and long) cantilever was used at scan rates between 2 and 5 Hz, depending on the resultant image resolution.

## CHAPTER IV

### RESULTS AND DISCUSSION

#### 4.1 DPN Depositions / LFM Measurements

The following sections describe the results pertaining to the LFM measurement of catalyst deposits prior to the CVD process and the measurement of some appropriate samples post CVD.

##### 4.1.1 Prior to CVD: Deposition Measurements

To verify the writing ability of a prepared DPN pen, a  $1\ \mu\text{m}$  by  $1\ \mu\text{m}$  square was deposited of each metal salt solution onto a Sindex chip, followed by the deposition for CNT growth on  $\text{SiN}_3$  membranes or AFM tips in tip to tip DPN mode. Figure 16 shows the verification of DPN deposition of  $\text{NiCl}_2$  onto both Sindex and  $\text{SiN}_3$  membrane

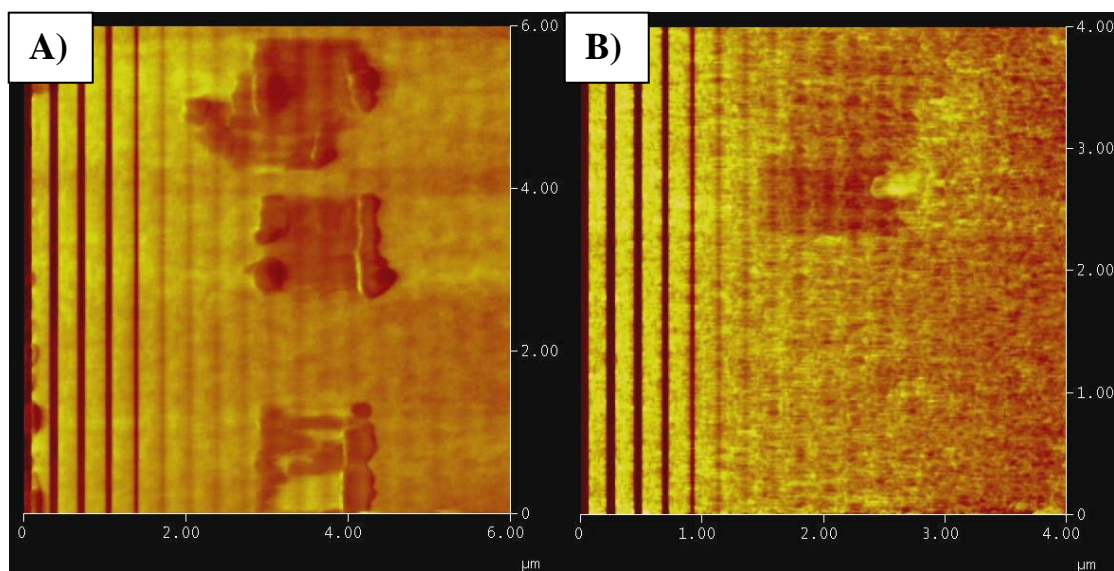
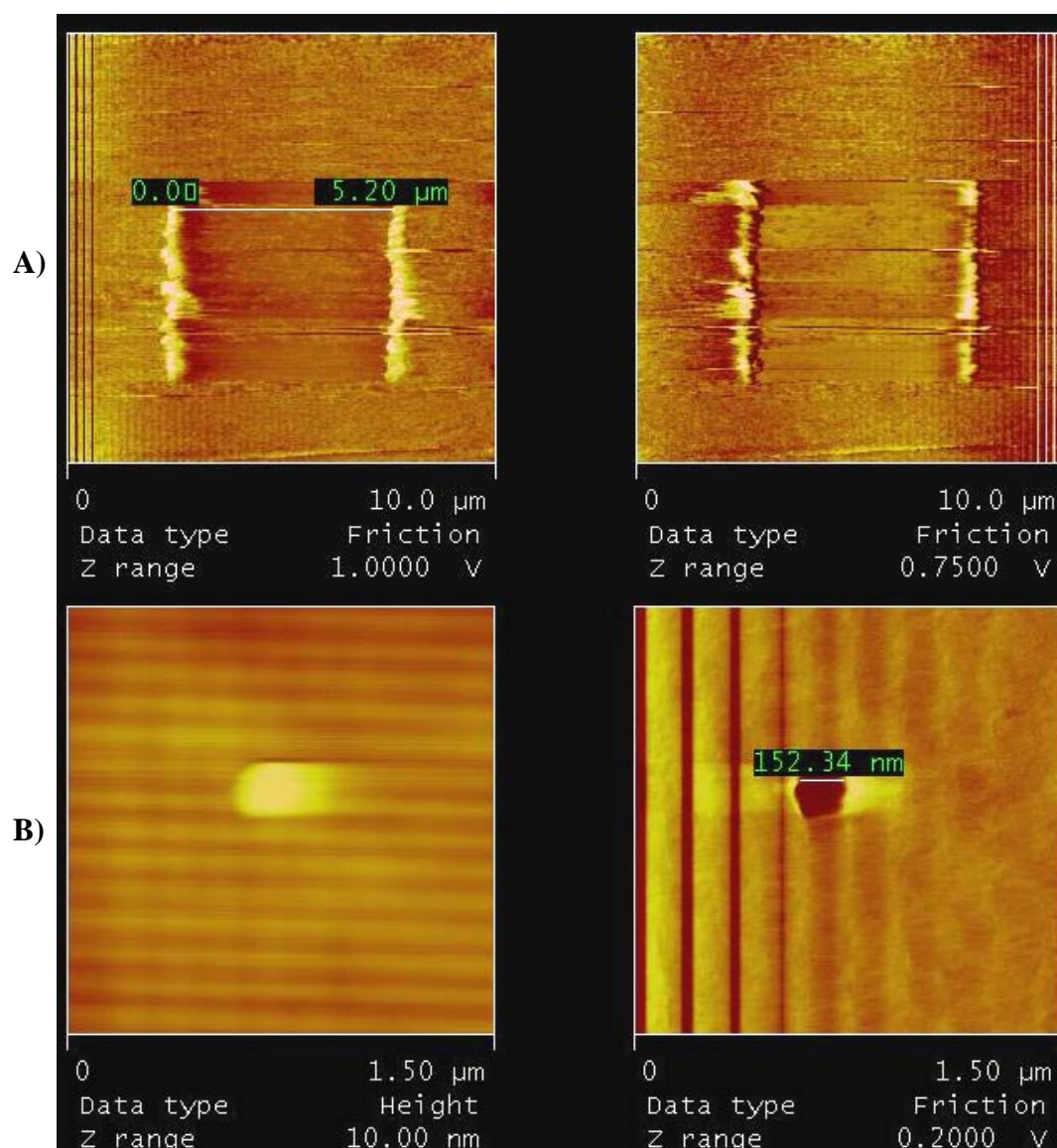


Figure 16. DPN of  $\text{NiCl}_2$  onto (A) Sindex Chip and (B)  $\text{SiN}_3$  Membrane



substrates, where three 1  $\mu\text{m}$  squares are deposited on the Sindex (A) and a 1  $\mu\text{m}$  square pattern on the  $\text{SiN}_3$  (B). In the deposition onto Sindex, the collection of deposited material near the lateral edges of the DPN scans are evident, which can be attributed to diffusion along the borders of the scan as well as the transfer from the pen tip occurring



**Figure 17. DPN of  $\text{CoCl}_2$  onto (A) Sindex Chip and (B)  $\text{SiN}_3$  Membrane**

during the reversal of motion. Likewise, DPN deposition of  $\text{CoCl}_2$  is depicted in Figure 17, where a  $5\ \mu\text{m}$  deposition on Sindex is shown in (A) and a  $150\ \text{nm}$  deposition on  $\text{SiN}_3$  in (B). The  $150\ \text{nm}$  wide pattern (B) can be clearly seen in both the topographical

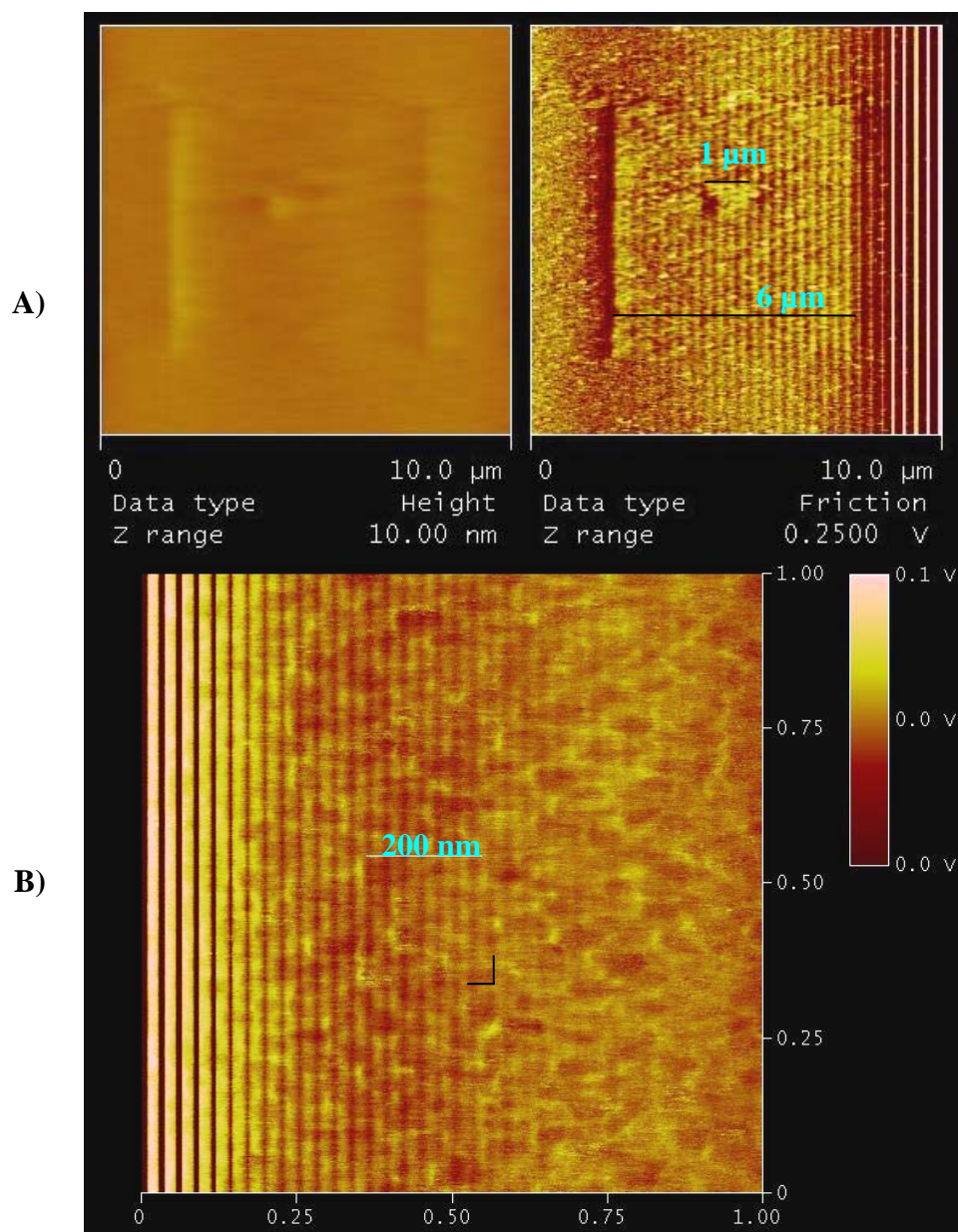


Figure 18. DPN of  $\text{PdCl}_2$  onto (A) Sindex Chip and (B)  $\text{SiN}_3$  Membrane

measurement (left) and the friction measurement (right). This pattern was obtained after attempting a 100 nm square pattern, for which the effects of pattern diffusion are seen in this image. Patterns of PdCl<sub>2</sub> were also created. Two such instances are shown in Figure 18. In the Sindex patterns (A), a double deposition, or bi-layer deposit, of a 1 μm square inside of a 6 μm square is pictured. Although faint, the height information (on the left) pertaining to this sample also depicts the slightly raised square pattern with the additional plateau in the middle. The deposition of PdCl<sub>2</sub> onto the SiN<sub>3</sub> is difficult to see in image (B), where only a faint outline of the square is visible in the lateral force measurement.

The collection of AFM images in Table 1 on the next two pages shows the repeated verification for all of the metal salts and salt mixtures of FeCl<sub>2</sub>, FeCl<sub>3</sub>, PtCl<sub>2</sub>, RhCl<sub>3</sub>, and the mixtures of NiCl<sub>2</sub>-CoCl<sub>2</sub> and RhCl<sub>3</sub>-PdCl<sub>2</sub>. As mentioned previously, the ability to observe DPN deposits on the SiN<sub>3</sub> window grids was quite difficult at times, which resulted in non-obvious scans in the case of RhCl<sub>3</sub>-PdCl<sub>2</sub> mixture. The growth of CNT from DPN deposits were evaluated for NiCl<sub>2</sub>, CoCl<sub>2</sub>, PdCl<sub>2</sub> and the NiCl<sub>2</sub>-CoCl<sub>2</sub> mixture.

Table 1. DPN Depositions for Various Metal Salts on Sindex and SiN<sub>3</sub> Substrates

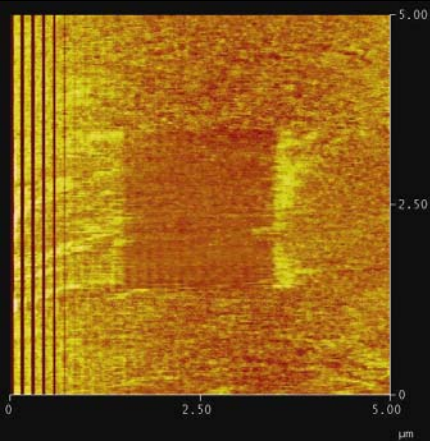
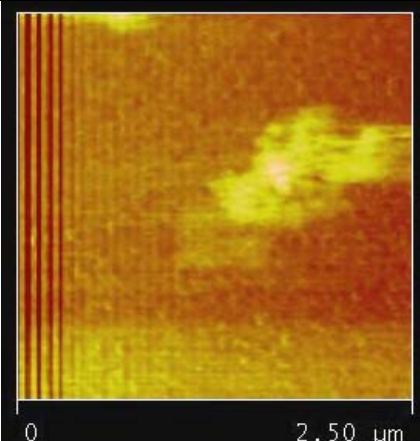
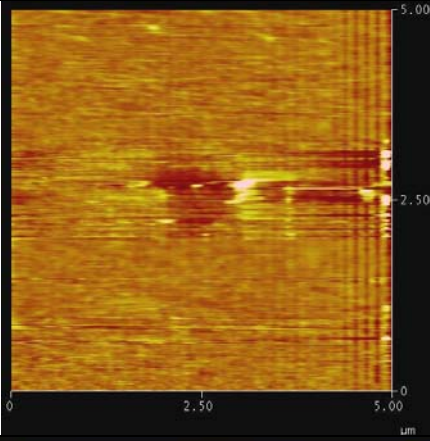
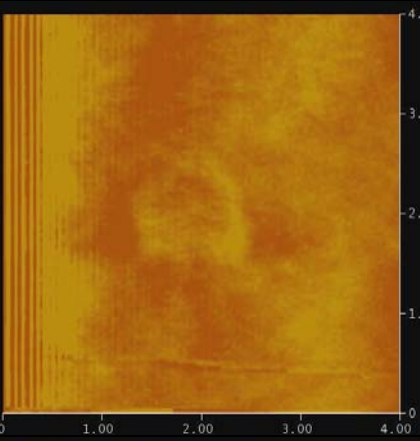
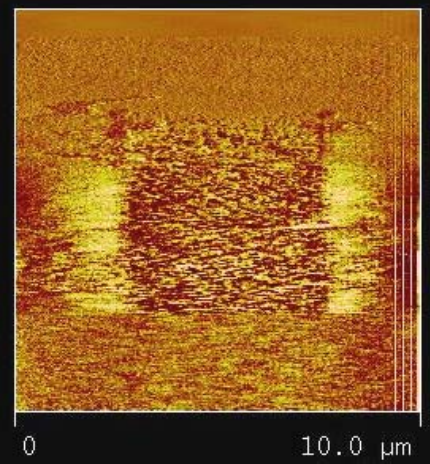
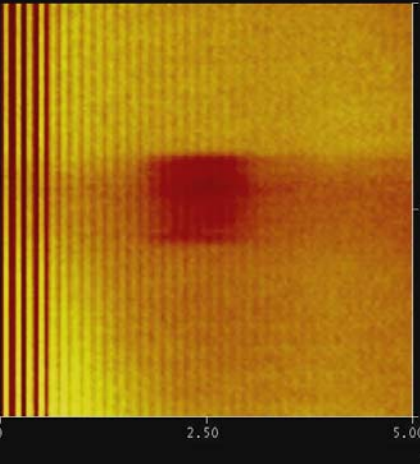
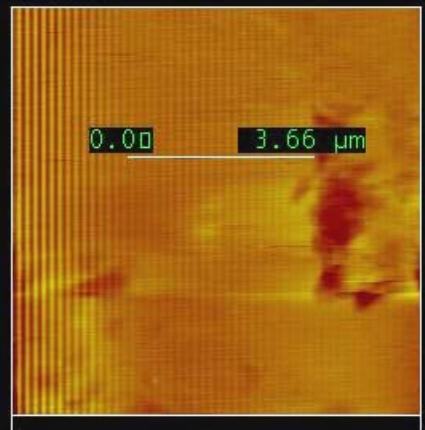
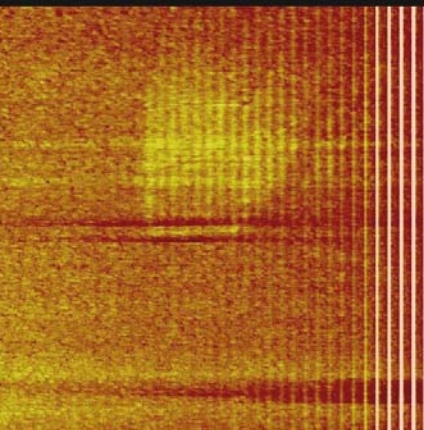
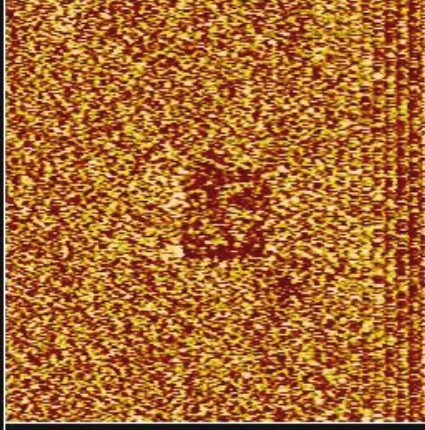
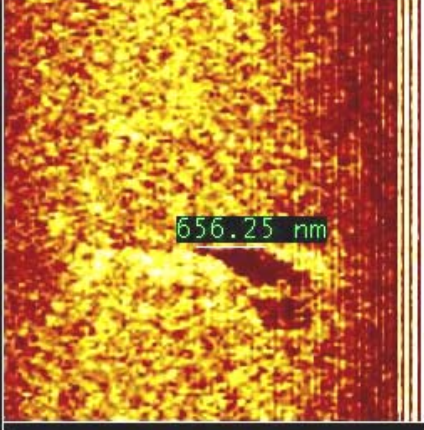
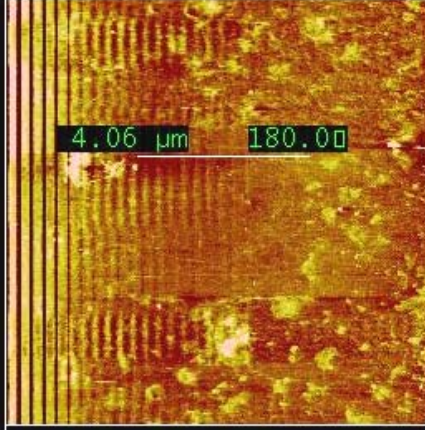
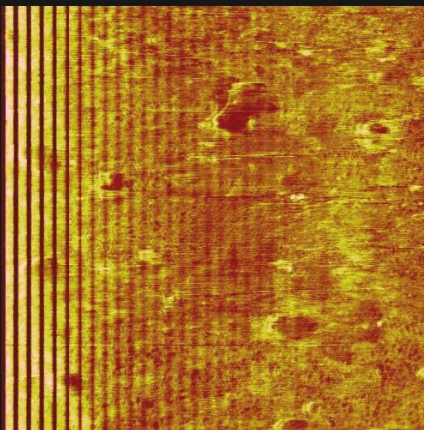
Metal Salt	Sindex Chip DPN	SiN <sub>3</sub> Membrane DPN
FeCl <sub>2</sub>		
FeCl <sub>3</sub>		
PtCl <sub>2</sub>		

Table 1, Continued

Metal Salt	Sindex Chip DPN	SiN <sub>3</sub> Membrane DPN
RhCl <sub>3</sub>	 <p>0.00 3.66 <math>\mu\text{m}</math></p> <p>0 8.00 <math>\mu\text{m}</math></p>	 <p>0 2.50 5.00</p>
NiCl <sub>2</sub> - CoCl <sub>2</sub> Mixture	 <p>0 5.00 <math>\mu\text{m}</math></p>	 <p>656.25 nm</p> <p>0 4.00 <math>\mu\text{m}</math></p>
RhCl <sub>3</sub> - PdCl <sub>2</sub> Mixture	 <p>4.06 <math>\mu\text{m}</math> 180.00</p> <p>0 10.00 <math>\mu\text{m}</math></p>	 <p>0 1.00 2.00 3.00 4.00</p>

#### 4.1.2 *Post CVD Comparison*

To verify the precision of synthesizing the CNTs at desired locations after deposition of catalysts by the DPN/CVD process, lateral force imaging of post CVD samples were evaluated. Because the nature of the surface of SiN<sub>3</sub> membranes causes difficulty in LFM measurements, a DPN sample of PdCl<sub>2</sub> was prepared on a gold film silicon wafer (Sindex) for its superior surface qualities. The deposited materials were evaluated before and after the CVD synthesis process. The images in Figure 19 (next page) were used to verify the efficacy of the developed process for its ability to deposit and synthesize CNT precisely at a particular location.

Figure 19a shows the deposition immediately after DPN, while Figure 19b through d show the deposition after the CVD process was complete. Figure 19c and d show 3D images of the post CVD sample at different "magnifications." The discrepancy between the sizes of the depositions in (a) and (b) can be explained by the fact that the probe that was being used to image the deposition in (a) actually continued to write ink to the surface during the shown scan. If one looks closely at image (b), the pattern seen in (a) is visible within the larger square near the center, but oriented at 90 degrees from the image in (a). Also, Figure 19b (and c) can be seen to have tube-like structures departing from the top of the square deposition toward the right of the scan, which are believed to be two separate CNTs or bundles. The 3D images show multiple bumps on the surface of the pattern ranging from less than 5 nm to 15 nm, which are likely the reduced Pd particles.

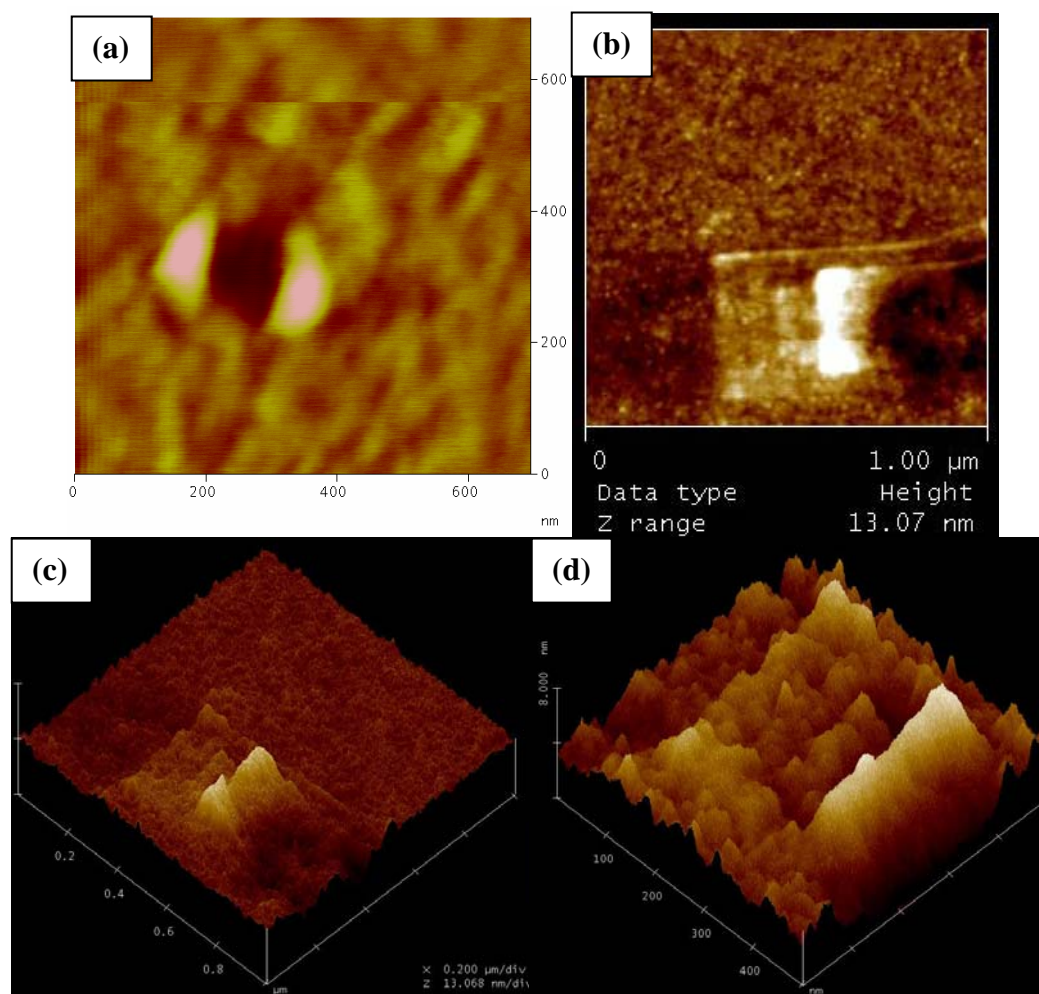


**Figure 19. LFM Imaging of PdCl<sub>2</sub> DPN on Sindex Chip (a) Before and (b) After CVD, Including (c) 3D Image and (d) Closer 3D Scan of Post CVD. [Figure 19(a) was obtained courtesy of Mr. Juan Alberto Rivas-Cardona, currently a graduate student of Mechanical Engineering Department at Texas A&M University].**

## 4.2 XPS Characterization

To verify the successful growth of carbon nanotubes from the metal salt compounds used as catalysts, the XPS responses of the bulk deposited samples before and after the CVD process were compared and are shown in Figures 17 – 19. Figure 20 (next page)

shows the XPS response for the metal salt samples prior to CVD. This figure incorporates all three responses. It should be noted that the relative intensities of the peaks between the three responses in these figures do not imply the information about the absolute concentration of the constituents relative to separate scans (represented by the different color spectra). In other words, the relative intensities of the peaks observed in each separate scan have no meaning, although the relative height of the peaks in a single scan does indicate the concentration of single elements in that particular spectral evaluation. Hence, the results are presented together only for convenience, e.g. the higher peak corresponding to silicon in the  $\text{NiCl}_2$  sample does not imply there is more

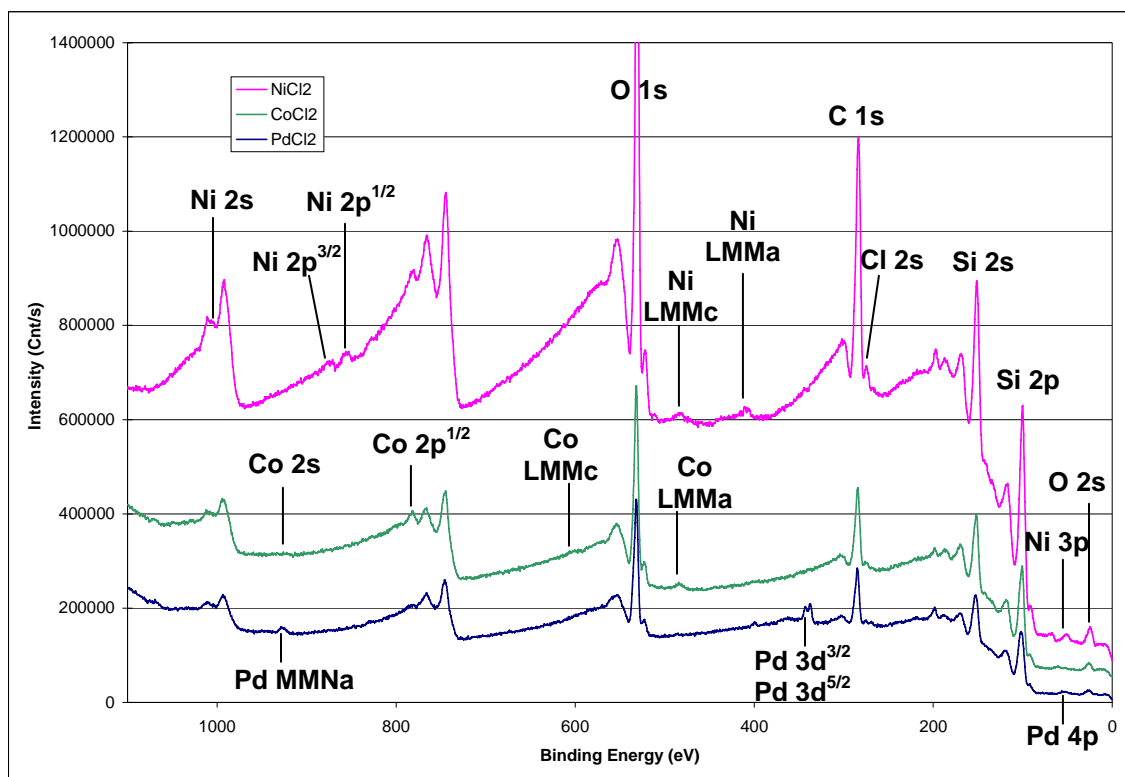


**Figure 20. XPS Response of Metal Salts Prior to CVD for  $\text{NiCl}_2$  (top),  $\text{CoCl}_2$  (middle), and  $\text{PdCl}_2$  (bottom)**



silicon in this sample, being that both samples were prepared on a silicon wafer. Table 2 in Appendix A describes the elements that correspond to the peaks in the figure for each sample. In the table, the element signified by the given binding energy peak is given with its spectral line information. As indicated by the XPS response, the sample contains a few contaminants, including oxygen and carbon. The presence of the oxygen is easily explained by the oxide layer that forms on the surface of the silicon wafer in the presence of air, while the presence of carbon is likely the effect of dust in the ambient environment migrating onto the surface of the sample during the evaporation of the salt solution deposited on the surface.

After the CVD deposition of carbon in the process for generating CNTs, the XPS

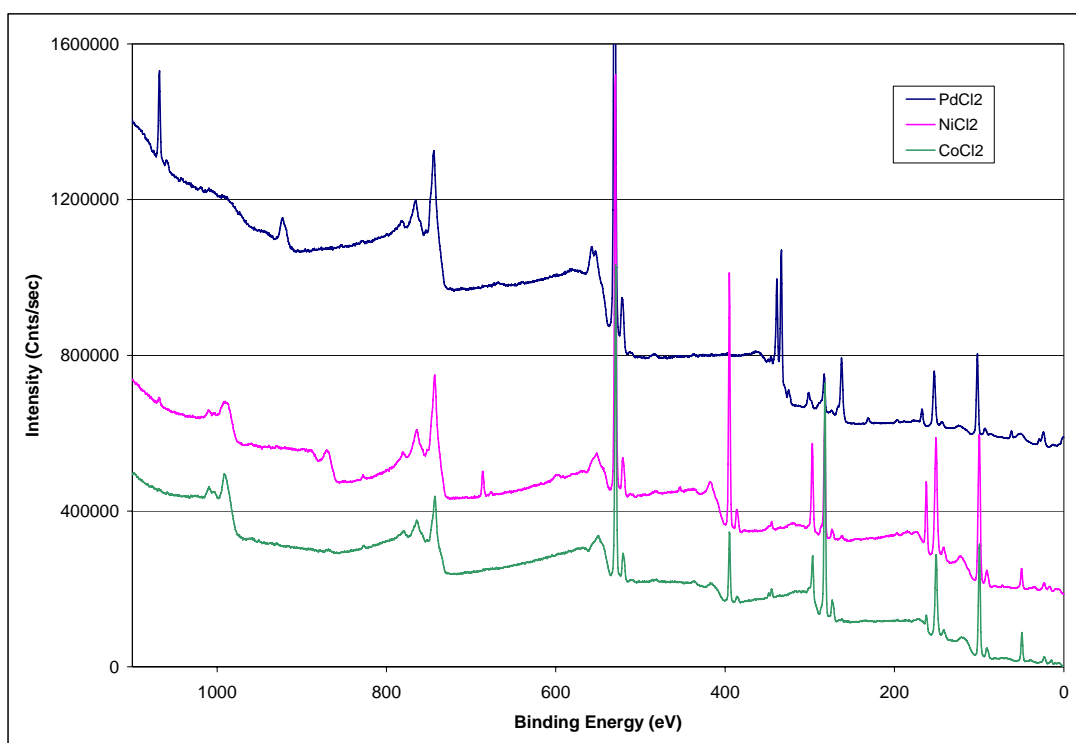


**Figure 21. XPS Response after CVD for PdCl<sub>2</sub> (top), NiCl<sub>2</sub> (middle), and CoCl<sub>2</sub> (bottom)**

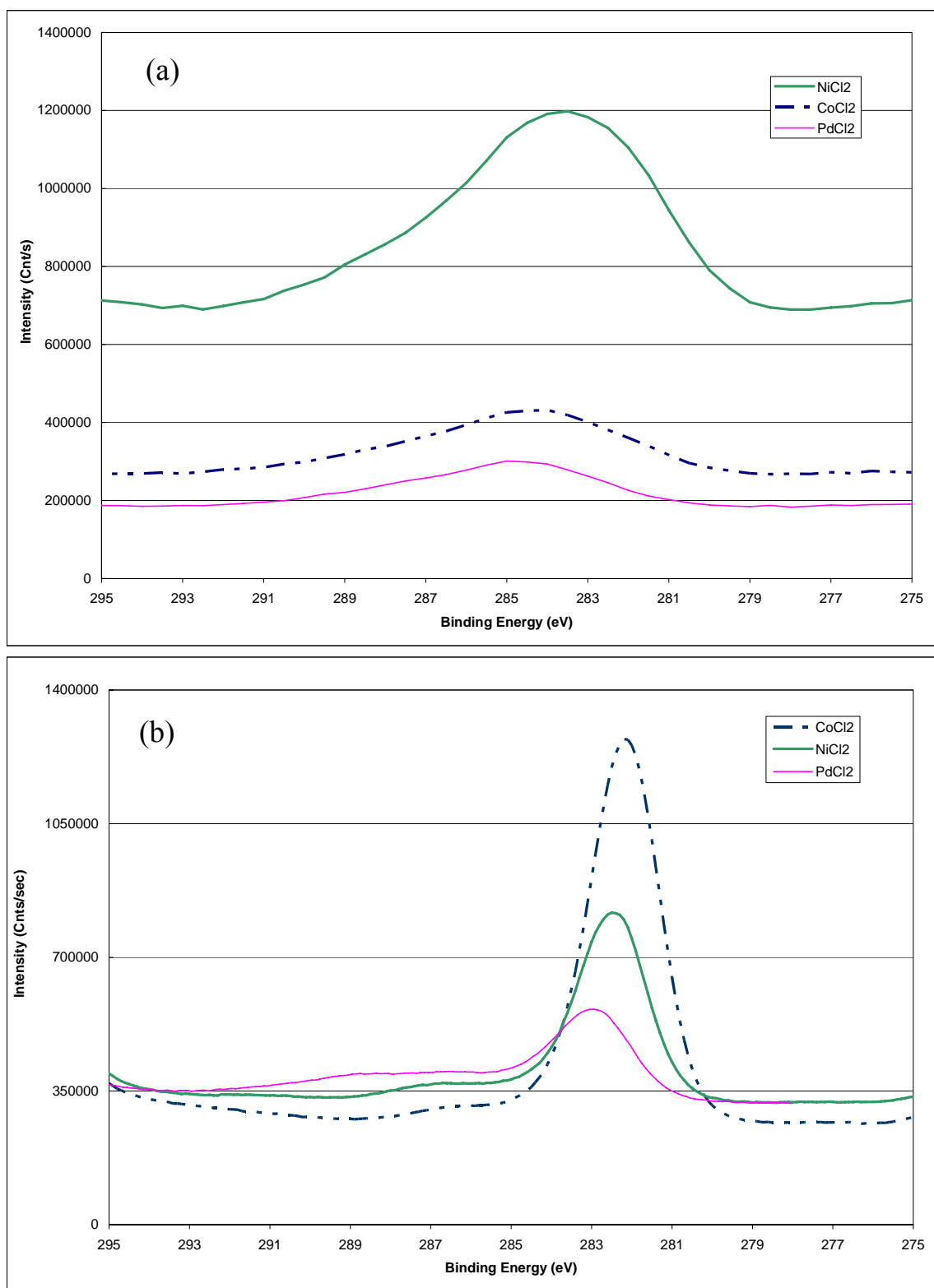
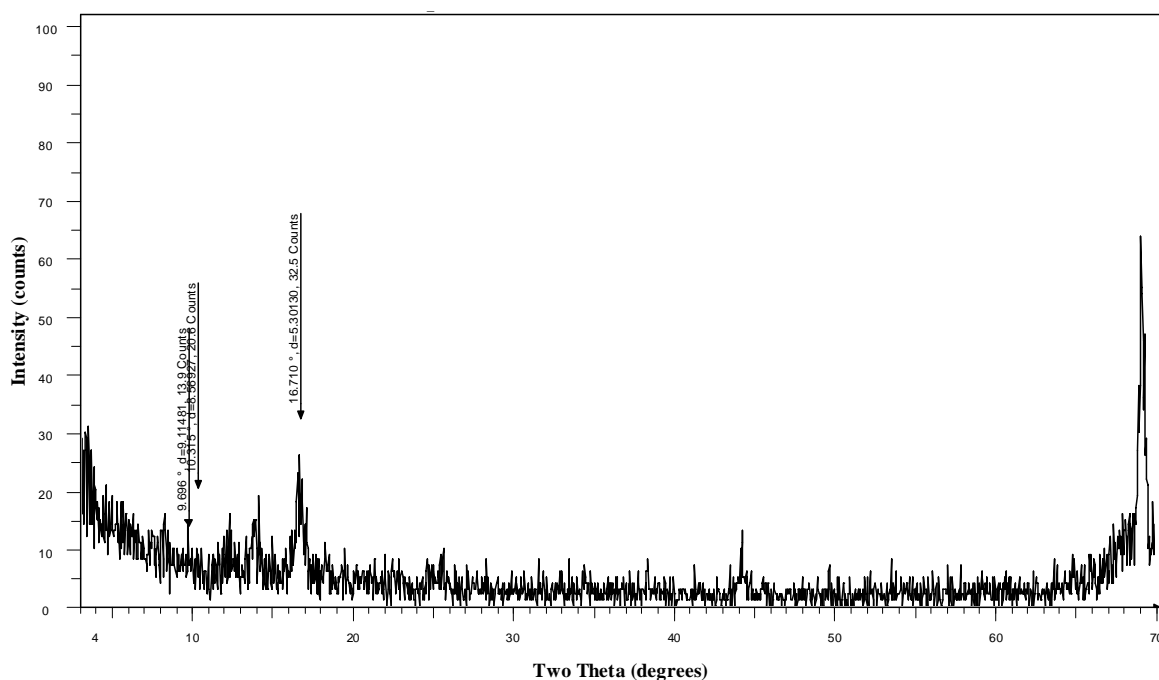


Figure 22. XPS Verification of Carbon Presence Prior to CVD (a) and After CVD (b)

response was shown to be slightly changed. Figure 21 depicts the XPS survey for post-CVD samples of  $\text{NiCl}_2$ ,  $\text{CoCl}_2$ , and  $\text{PdCl}_2$ . To be noted, an extra peak at 395 eV is observed in the  $\text{NiCl}_2$  and  $\text{CoCl}_2$  samples (though not in  $\text{PdCl}_2$ ) in this graph which corresponds to nitrogen. This is present because these two particular samples were prepared on silicon nitride ( $\text{SiN}_3$ ) membranes instead of on Si wafers, although the actual process was identical. It is also noticed that sharper peaks are observed at approximately 285 eV corresponding to increased carbon levels. Figure 22 (a) and (b) respectively show the carbon 1s peaks before and after CVD treatment for the sake of comparison. Figure 22b shows sharper peaks that are centered about a slightly lower binding energy. The width of the peaks in Figure 22a is indicative of amorphous carbon mixed with trace elements of other contaminants, which signifies that it is purely a dust-type contaminant. Additionally, the XPS results indicate an increased level of carbon in the sample, consistent with the CVD process which only deposits carbon where catalyst material is present.

### 4.3 XRD Characterization

An X-ray diffraction study of the bulk prepared samples was also attempted for structural characterization of the deposited carbon after CVD. Figure 23 (next page) depicts the spectral response obtained from evaluating a bulk prepared sample of  $\text{PdCl}_2$  after performing CVD. The peaks in this response indicated with the arrows correspond to peaks associated with C70 (a chemical characterization for CNT); however, as one can see, the signal to noise ratio is undesirable and the results are somewhat inconclusive



**Figure 23. XRD Response for Post-CVD PdCl<sub>2</sub> Bulk Sample on Si**

since not all C70 peaks are present. After obtaining similar graphs for NiCl<sub>2</sub> prepared samples, it was determined that the XRD equipment available for this experiment was not adequate for the types of samples created in this experiment. The apparatus was designed as a powder XRD and could not be properly aligned on a microscopic scale for evaluating small samples such as those produced for this study.

#### **4.4 Direct Measurements Using TEM and SEM**

##### *4.4.1 TEM of Bulk Deposited Samples*

TEM images of the bulk deposited salts also confirmed the presence of multi-walled CNTs (MWNTs) which can be seen growing around metal particles of diameters between 10 and 50 nm. Figure 24 (next page) shows a bundle of nanotubes grown from

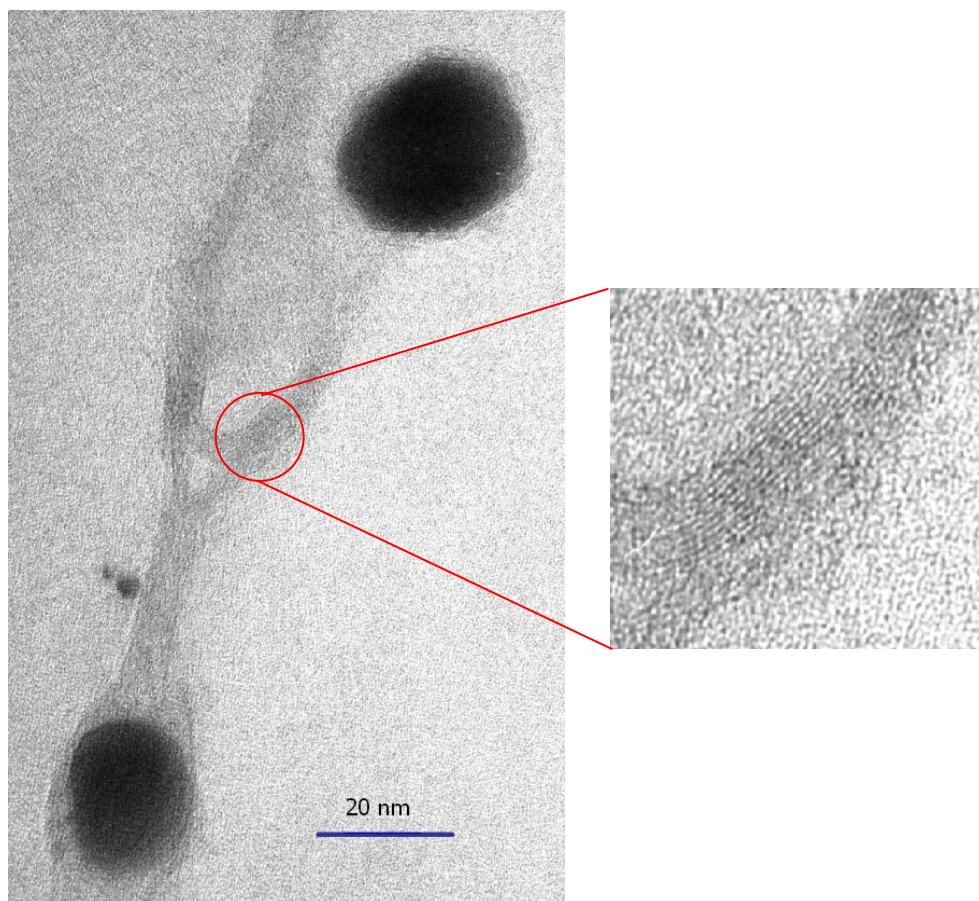


**Figure 24. Bundle of CNTs Grown from Bulk Deposition of NiCl<sub>2</sub>**

Nickel nanoparticles which are derived from the reduction of NiCl<sub>2</sub> during the CVD process. The figure clearly shows the different layers of the walls grown on a metal particle. Similar micrographs of CNTs formed from the bulk deposition of CoCl<sub>2</sub> as well as the mixture of NiCl<sub>2</sub> and CoCl<sub>2</sub> were taken, for which select images are shown in Figure 25. As indicated in the figure, the bulk deposition of CoCl<sub>2</sub> results in similarly sized CNTs as seen in Figure 24 – between 5 and 10 nm in diameter (in the absence of trapped catalyst particles). However, somewhat smaller diameter tubes are observed in

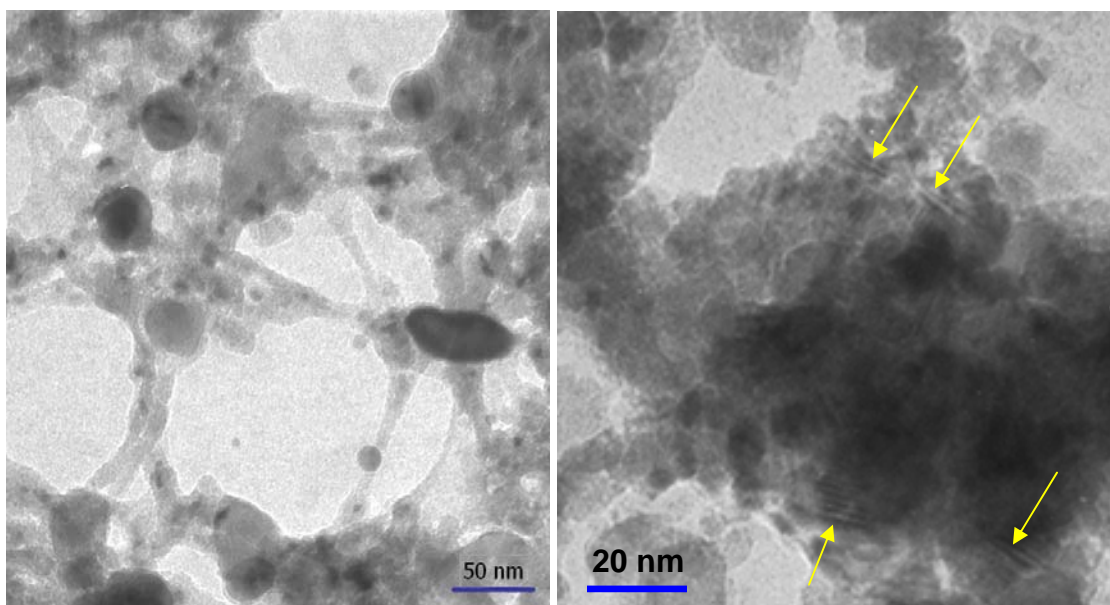


**Figure 25. CNT Formations from  $\text{CoCl}_2$  (Left) and  $\text{NiCl}_2\text{-CoCl}_2$  Mixture (Right) Bulk Deposits**

the TEM micrograph of the post-CVD  $\text{NiCl}_2\text{-CoCl}_2$  mixture bulk deposit. Those CNT observed are approximately 2 nm in diameter.

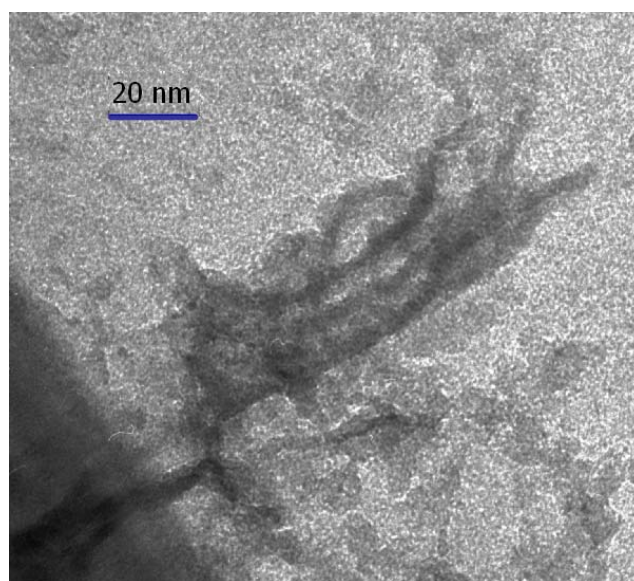


**Figure 26. CNT Bundle Grown from 1 $\mu\text{m}$  DPN Pattern ( $\text{PdCl}_2$ )**

#### 4.4.2 TEM of DPN Samples

In the case of  $\text{SiN}_3$  membranes, TEM imaging also verified the presence of CNTs at locations where the nano-patterns of catalyst material were deposited by DPN. Figure 26 shows a bundle of CNTs grown from a  $1\ \mu\text{m}$  square pattern of  $\text{PdCl}_2$ .

Similar results were obtained with  $\text{NiCl}_2$  and  $\text{CoCl}_2$ , whose micrographs are shown in Figure 27 and Figure 28, respectively; although the frequency of CNT growth was definitively less than that seen with Pd catalysts for both Ni and Co. The  $\text{NiCl}_2$  catalyst produced single 2 nm diameter tubes of roughly 20 nm length, as seen in Figure 27. The  $\text{CoCl}_2$  DPN sample produced slightly larger single CNTs (4-5 nm in diameter) than the  $\text{NiCl}_2$ , but both catalysts were shown to generate a significant amount of amorphous carbon in relation to the tube frequency, unlike that seen in the  $\text{PdCl}_2$  samples. Figure 28 depicts the presence of a 4 nm diameter CNT growing from the resultant catalyst of a

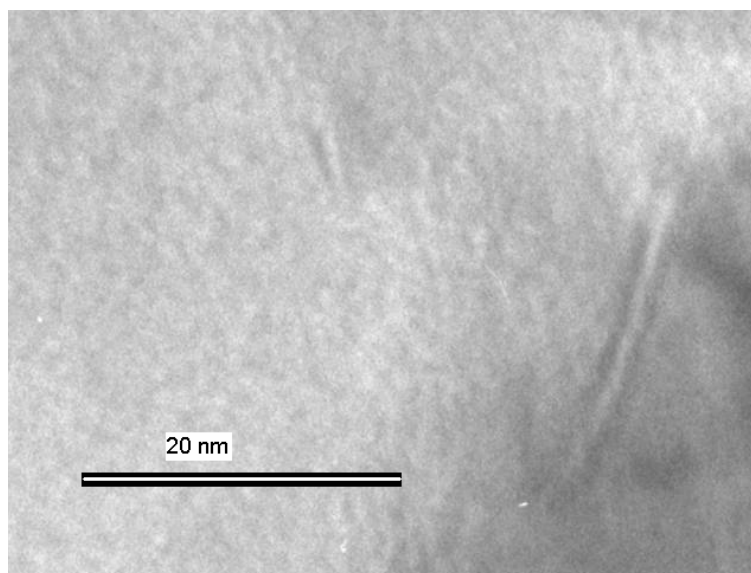


**Figure 27. CNT Formation from 1 $\mu\text{m}$  DPN Pattern ( $\text{NiCl}_2$ )**

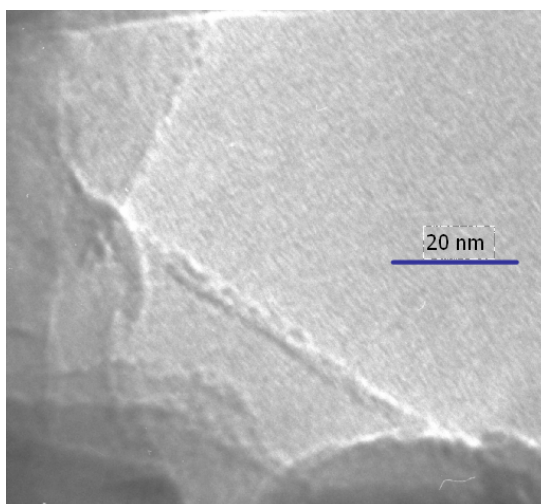


**Figure 28. CNT Formation from 2um DPN Pattern (CoCl<sub>2</sub>)**

2 μm DPN pattern. The DPN of the mixture of NiCl<sub>2</sub> and CoCl<sub>2</sub> behaved somewhat differently from either of the two metal salt solutions alone. The first and most notable difference observed was that metal particle formation along with CNT generation was achievable from smaller DPN patterns. In Figure 29, CNTs forming from metal catalyst

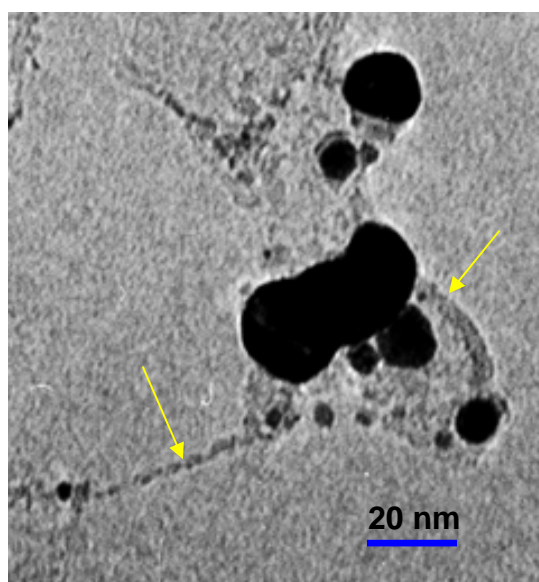


**Figure 29. CNT Formation from 30 second Stationary DPN Pattern (NiCl<sub>2</sub>-CoCl<sub>2</sub> Mixture)**



particles is observed for a DPN deposition where the tip was placed in contact with the substrate for 30 seconds before removing the probe and repeating at a distance of 750 nm away in a 3 x 3 array.

#### 4.4.3 SEM of AFM Tip Samples

After CVD processing of the tip-to-tip prepared samples, the probes were evaluated with SEM in attempt to identify CNT growth on the tip where the DPN deposition had been performed. Unfortunately, high-resolution images of the tips were not possible because the non-conducting nature of the silicon nitride probes resulted in significant sample charging. Multiple imaging attempts were made using different SEM technologies; however, even when sputtering the surface of the probe with a conductive layer could not alleviate the electron charging that occurred. Even so, somewhat lower magnification images were obtainable, for which some are presented in Figure 30. In

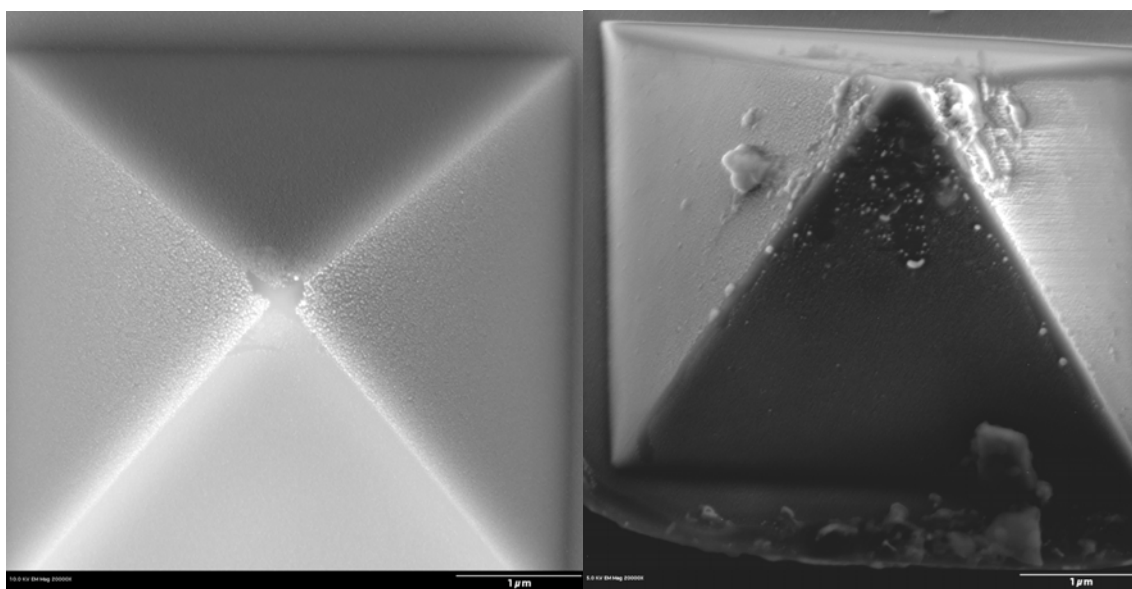


**Figure 30. SEM Micrographs of Clean AFM Tip (Left) and Post-CVD Tip-to-Tip Sample Showing Presence of CVD Deposit (Right)**

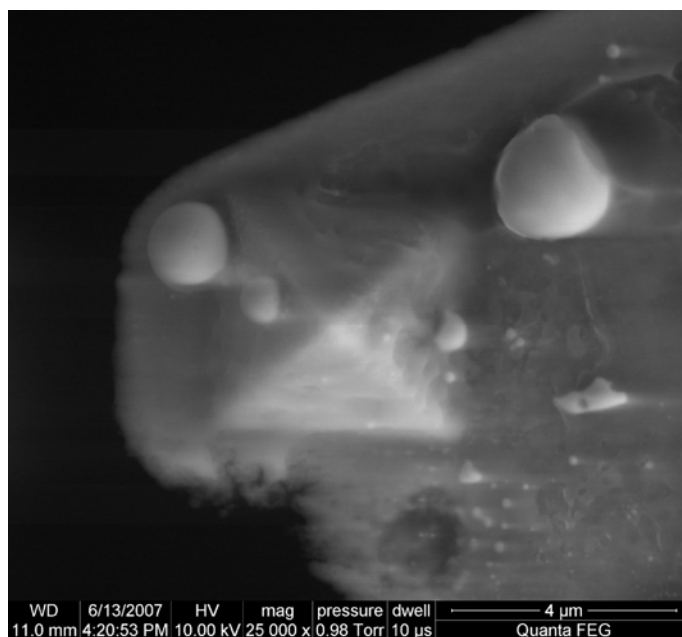


**Figure 31. SEM Micrograph of Deposited Material on Post-CVD Inkwell Dipped Sample**

these images it is possible to see the collection of particles on the tip of the probe where DPN was performed. Additionally, similar images were obtained for Inkwell dipped probes, where instead of only seeing material present at isolated locations, the observed "film" of deposited material is more pervasive. Figure 31 depicts this behavior. In this image, large clumps of material are observed which are stray droplets of the silver paint used to conductively adhere the sample to the SEM stage. Although images at this magnification do not verify the presence of CNT, energy dispersive x-ray spectroscopy (EDX) confirmed the presence of carbon on the tip of the probe, as seen in the chart in Figure 32 (next page). This spectrum, taken with the assistance of Dr. S.K. Ganguli, also shows the presence of gold and palladium on the tip which is due to the sputtering of the sample for enhanced imaging using a Au-Pd target. The elements

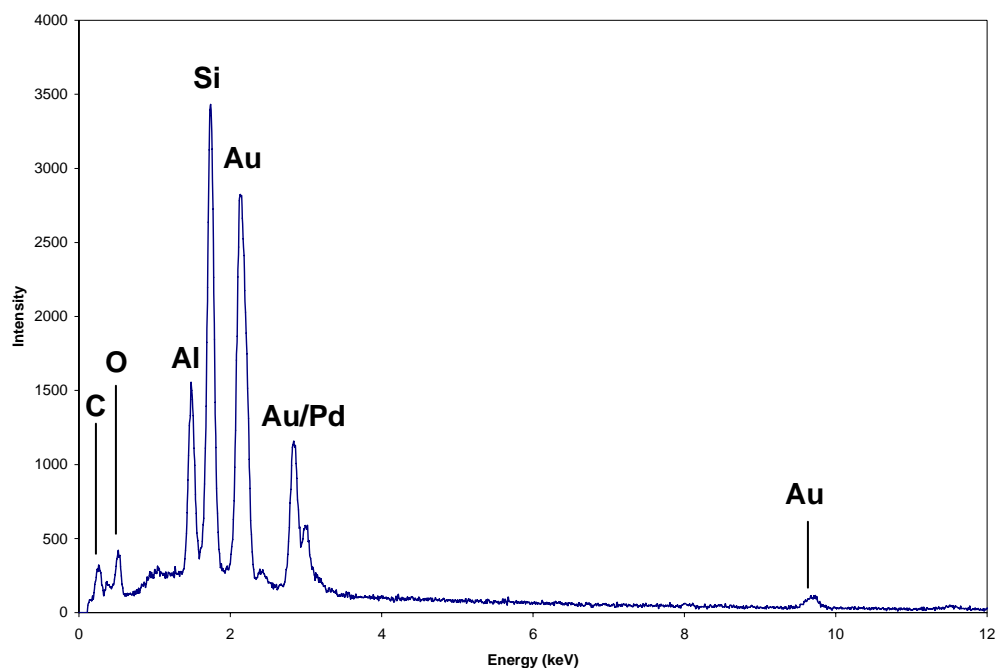


**Figure 32. EDX Analysis of Tip-to-Tip Sample (Courtesy Dr. S.K. Ganguli)**

corresponding to the peaks are indicated in the figure. The aluminum detected in this scan is caused by the SEM stage. Although this still does not qualify the presence of CNT, Raman spectroscopy (to be discussed later) verified that the carbon content was in fact nanotubes.

## 4.5 Raman Spectral Characterization

### 4.5.1 Samples Prepared on $\text{SiN}_3$

When performing Raman spectral characterizations of the DPN and bulk prepared samples, laser excitation wavelengths of 633 nm and 785 nm were available. Prior studies using Raman spectroscopy has shown that differing excitation wavelengths cause a variation in the signal background but do not alter the spectral response of the

CNT samples.<sup>15</sup> Since the signal background can be quite different for different excitation sources during Raman spectroscopy it can lead to one excitation wavelength exhibiting preferential response behavior in the intensity of the peaks. This effect is illustrated in Figure 33, where the D and G bands of a MWNT sample are seen to have the same peaks at roughly  $1320\text{ cm}^{-1}$  and  $1600\text{ cm}^{-1}$ , respectively, while the shape of the peaks are quite different. Because of this effect, the 633 nm laser was primarily used for Raman analysis, although in some instances the 785 nm laser more clearly showed the presence of the RBM peak. In the following sections the results obtained with either laser excitation wavelength will be presented depending on the clarity of the spectral

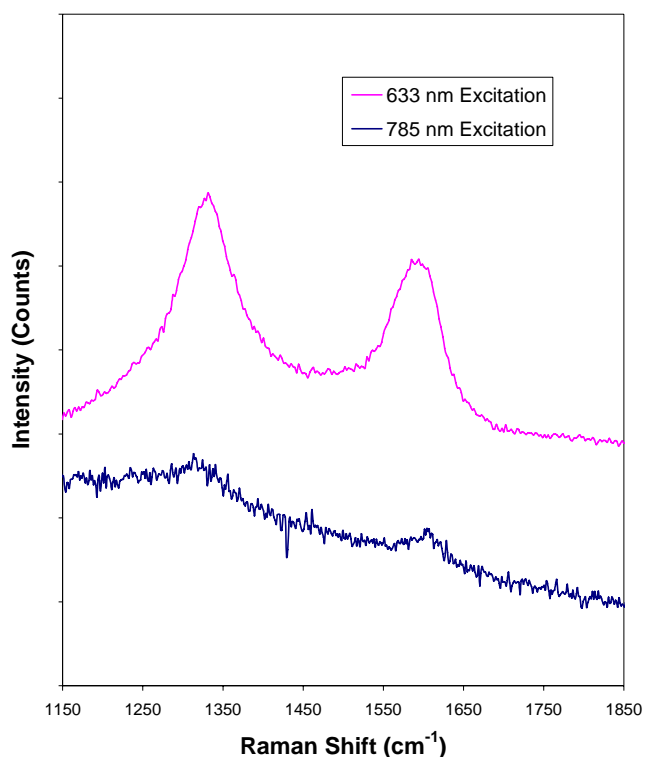


**Figure 33. Comparison of Raman Laser Excitation for Wavelengths of 633 and 785nm**

information. The detailed results for the different spectral responses corresponding to either laser energy are presented in Appendix B.

In the following pages, the Raman spectra are compared for both types of CNT samples (prepared either by bulk deposition or by nano-patterning of the catalysts by DPN). As indicated in the figure legends, the DPN sample responses are plotted in bold magenta while the bulk samples are shown in navy blue (thin). In the Raman spectra peaks from the silicon substrate are also obtained and the silicon substrate is found to exhibit peaks at 303, 460, and 525  $\text{cm}^{-1}$  as seen in Figure 34. Since the silicon response is not the focus of this study, the figures are arranged such that only the RBM peak range (100 - 300  $\text{cm}^{-1}$ ) and the D and G band range (1150 - 1700  $\text{cm}^{-1}$ ) is provided for better clarity. The RBM range is shown in the left image while the D and G band

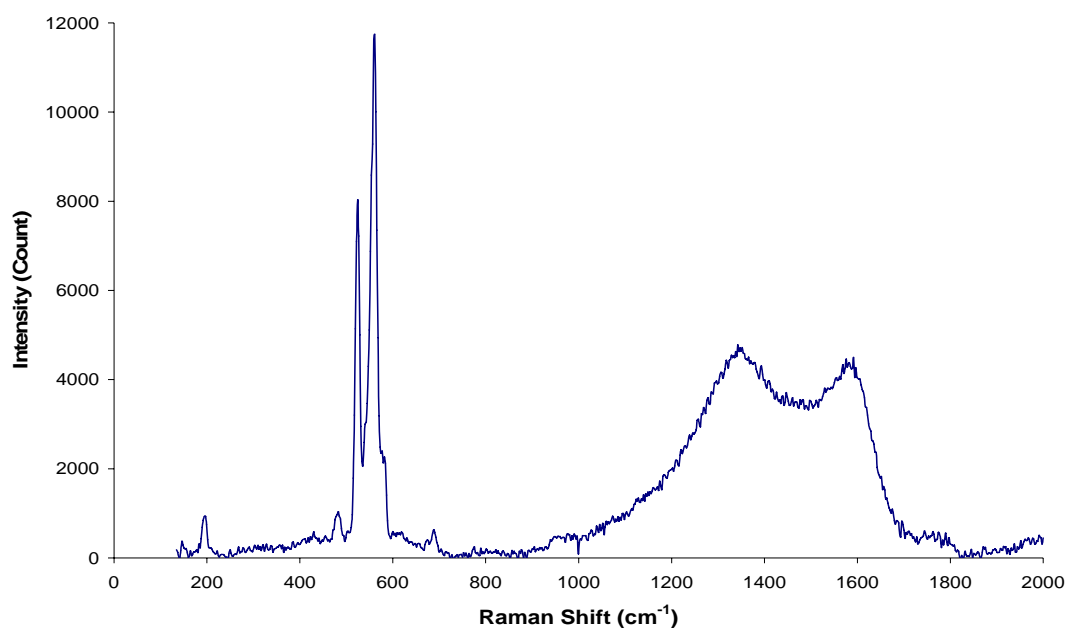


**Figure 34. Full Raman Spectra of MWNT**

range is presented on the right. Figure 35 depicts these Raman responses for the bulk and DPN samples prepared with  $\text{NiCl}_2$ . In the bulk response, clearly MWNT spectra is observed where the D band ( $1330 \text{ cm}^{-1}$ ) exhibits greater intensity than the G band ( $1590 \text{ cm}^{-1}$ ), without a clear response in the RBM. This is typical of MWNT samples, where no single diameter dominates in the radial excitation of the tube sample. However, when evaluating the DPN prepared sample, an RBM peak appears at  $230 \text{ cm}^{-1}$ , while no significant evidence of the D and G bands is shown. The RBM peak indicates a diameter of 1.1 nm which corresponds well to the TEM micrographs (see Figure 27) taken of the CNT sample obtained by the combination of DPN and CVD process. This correlation indicates that an error in the signal is unlikely, and therefore, there must

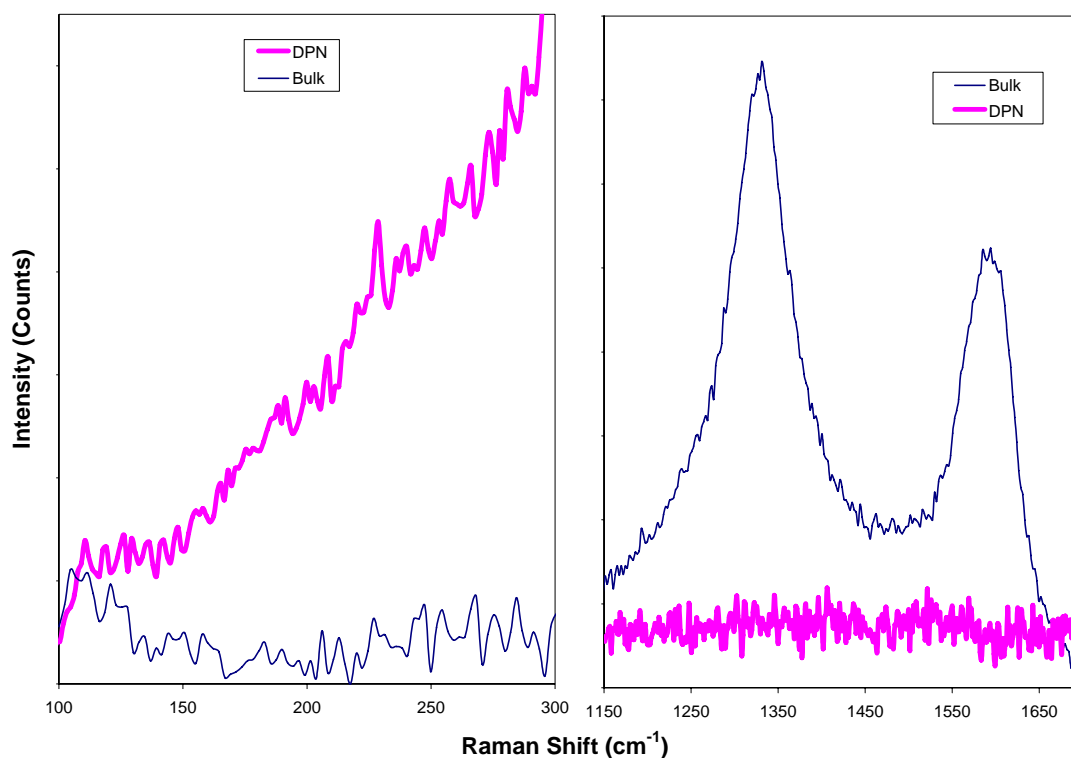


**Figure 35. Raman Spectra for CNTs Grown from Bulk and DPN Deposits of  $\text{NiCl}_2$**

be some physical reason for the lack of the D and G bands. The lack of the D band is not as unusual since this is indicative of SWNT. However, the G band discrepancy presents a peculiar question: do the CNT produced in this manner behave differently? One explanation may be that since the CNT have a low aspect ratio and produced in low number density, the axial structural features do not have significant contribution to the laser scattering. If this is reason is valid, then a very weak signal for the peak is observable, which is the case. A shallow peak at approximately  $1530\text{ cm}^{-1}$  (spanning  $1450$  to  $1600\text{ cm}^{-1}$ ) can be seen although weak. This peak is significantly shifted to the left of the bulk sample which indicates a CNT of the metallic type. This seems reasonable since previous research<sup>16</sup> indicated a relationship between metallic chirality tubes and decreasing tube diameter.

When evaluating the Raman response from  $\text{CoCl}_2$  depositions, similar results were obtained, which are shown in Figure 36. Unlike the  $\text{NiCl}_2$  bulk sample, the  $\text{CoCl}_2$  bulk sample displayed very distinct RBM responses at  $150$  and  $190\text{ cm}^{-1}$  (corresponding to  $1.7$  and  $1.3\text{ nm}$  diameters) which indicates the presence of some SWNT although MWNT are also present as signified by the large D band peak at  $1350\text{ cm}^{-1}$ . Another interesting feature of the D and G bands in the bulk sample is the shallow trough observed between the two crests of the peaks. It appears that a smaller peak around  $1450\text{ cm}^{-1}$  exists between the large peaks that results in this behavior which would show a separate band of conducting tubes that may correspond to the smaller diameter observed in the RBM. Looking at the DPN sample, an RBM peak is also observable at  $190\text{ cm}^{-1}$ , as well as  $240\text{ cm}^{-1}$ , which correlate to  $1.3$  and  $1\text{ nm}$  diameters, respectively.

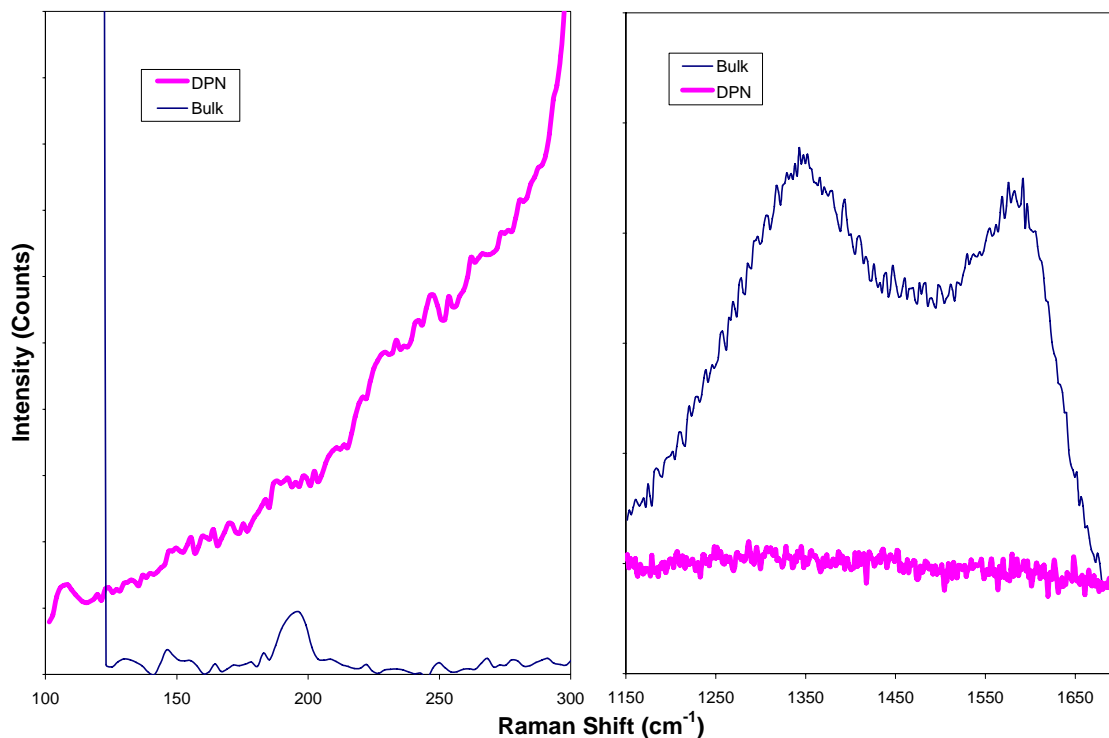


**Figure 36. Raman Spectra for CNTs Grown from Bulk and DPN Deposits of  $\text{CoCl}_2$**

Again, the D and G bands are not evident as in the bulk sample; however, a close examination shows slight peaks at the same shift as the bulk G band peaks at 1450 and 1560  $\text{cm}^{-1}$ . Although unclear, this may signify the nature of the DPN produced tubes as a mixture of conducting and semi-conducting.

Figure 37 depicts another very similar Raman response for  $\text{PdCl}_2$  samples. As in the  $\text{NiCl}_2$  bulk sample, the  $\text{PdCl}_2$  bulk sample also clearly exhibits MWNT, shown by the lack of RBM response and the large D band peak at 1330  $\text{cm}^{-1}$ . Additionally, two G band peaks – the larger at 1590  $\text{cm}^{-1}$  and the smaller at 1460  $\text{cm}^{-1}$  – indicate the presence of both semi-conducting and conducting tubes, respectively, although in greater



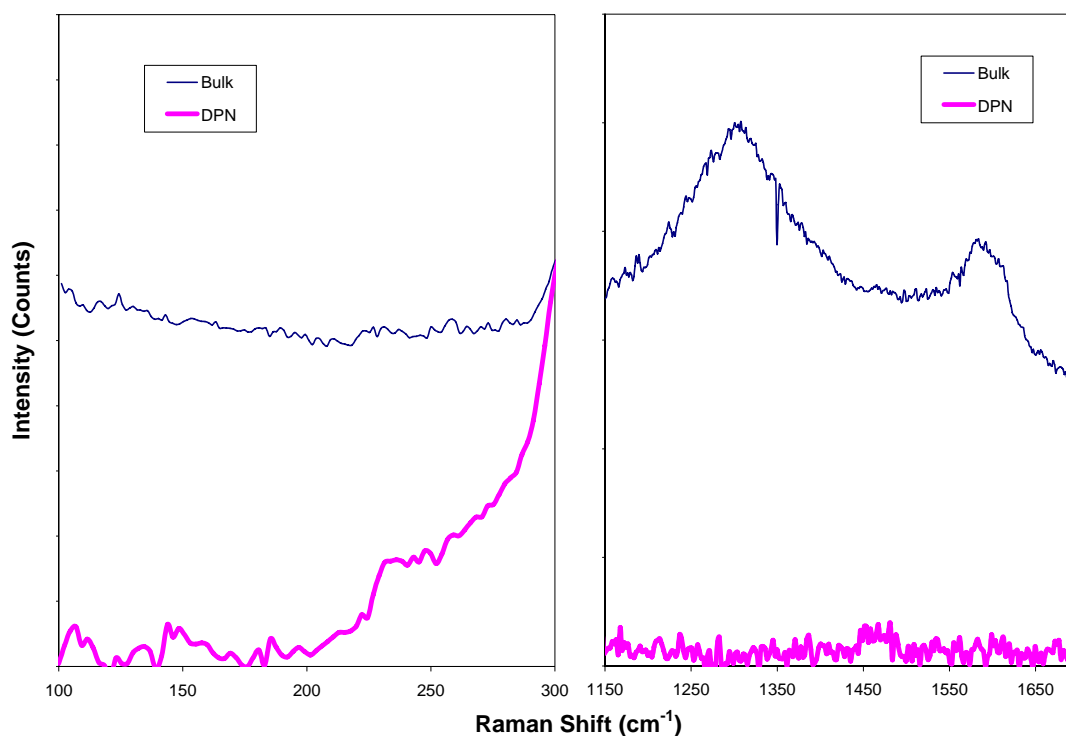


**Figure 37. Raman Spectra for CNTs Grown from Bulk and DPN Deposits of PdCl<sub>2</sub>**

proportion of semi-conducting. Alternatively, the DPN sample exhibits SWNT of 1.1 nm diameter which are exclusively conducting as indicated by  $\omega_{\text{RBM}} = 230 \text{ cm}^{-1}$ ,  $\omega_{\text{G-band}} = 1460 \text{ cm}^{-1}$ , and the lack of the D band peak.

Unlike the other metal salts, the mixture of NiCl<sub>2</sub> and CoCl<sub>2</sub> behaved much differently, as seen in Figure 38. The bulk sample's Raman response (shown in navy) exhibited a very clear RBM peak at  $190 \text{ cm}^{-1}$  while not having a strong response in the D and G bands. This behavior is more similar to the DPN samples previously studied. A slight G band peak is observable at  $1550 \text{ cm}^{-1}$ , for which it seems that the bulk sample produced very short SWNT of 1.3 nm diameter that are semi-conducting in type. However, an unusual peak is observed in the Raman Spectra for the sample obtained

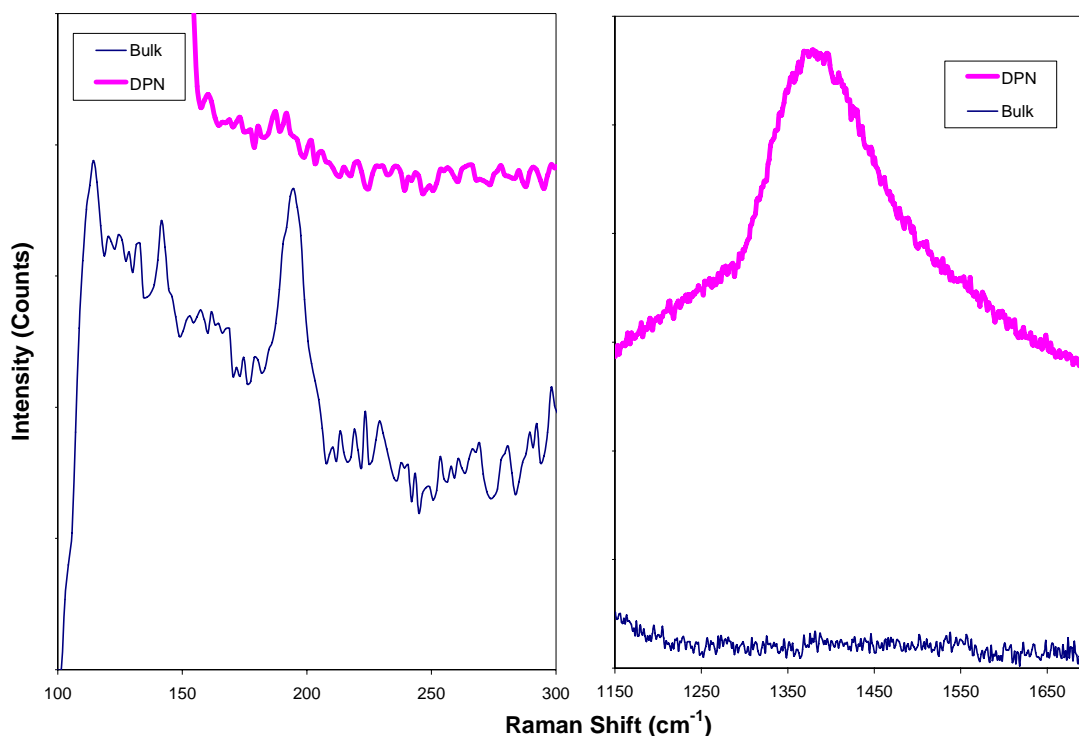


**Figure 38. Raman Spectra for CNTs Grown from Bulk and DPN Deposits of NiCl<sub>2</sub>-CoCl<sub>2</sub> Mixture**

from the DPN process. The G band is observed to shift strongly to the left with a very intense signal at  $1375\text{ cm}^{-1}$ . Additionally a weak RBM peak at  $185\text{ cm}^{-1}$  can be seen, suggesting the presence of 1.4 nm diameter conducting tubes of significantly greater aspect ratio than seen in the bulk prepared sample.

When scanning the surface of the samples, other anomalous Raman signals were found in the case of two of the DPN prepared samples. As shown in Figure 39, MWNT signals were observed at particular locations on both a PdCl<sub>2</sub> DPN and NiCl<sub>2</sub> DPN sample. Here, somewhat weak, although clear, D and G peaks are observed at  $1320\text{ cm}^{-1}$  and  $1600\text{ cm}^{-1}$ , respectively, while no obvious RBM peak is present. The locations at which

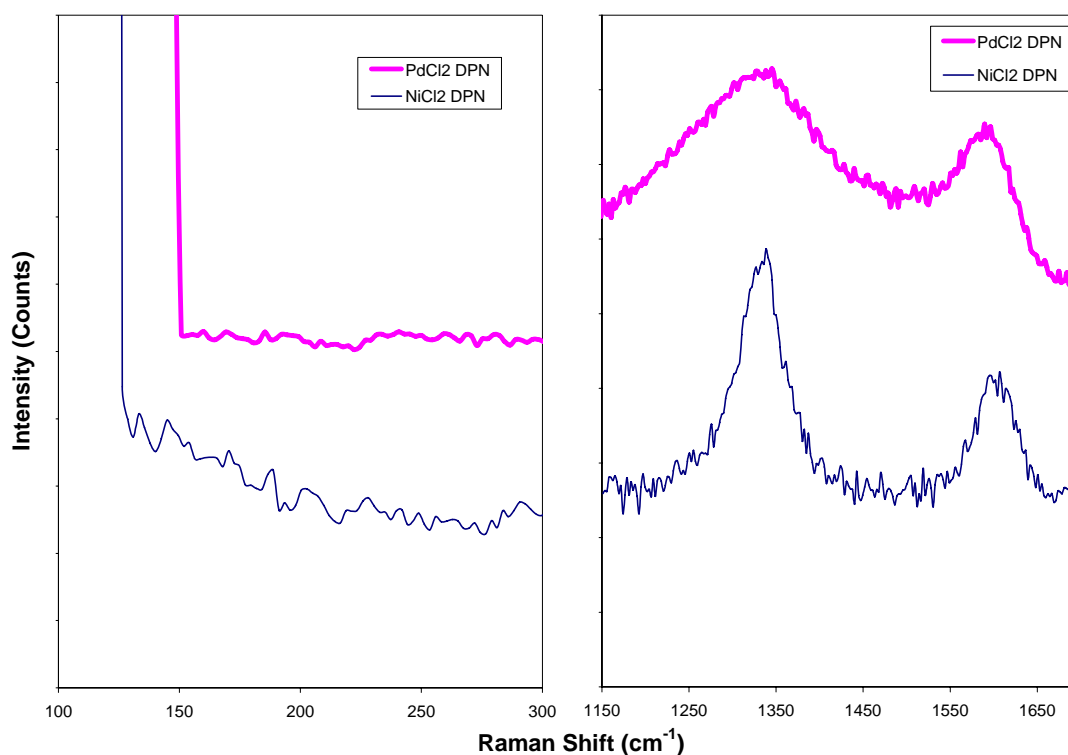


**Figure 39. Raman Scans of Anomalous Behavior on DPN Samples Showing MWNT**

these responses appeared, however, were no where near the locations where DPN patterns were made and had no connection with the patterned material. It is believed that these signals are either the result of CNT(s) grown from contaminating particles - perhaps iron particles in dust - or the accidental deposition of vagrant CNTs present in the CVD system from previous experiments which happened to land on the surface of the sample. In either case, it does not seem that these signals could have arisen from any tubes generated on the DPN samples which were hundreds of microns away from the laser spot.

#### 4.5.2 Samples Prepared on AFM Probe Tips

The samples prepared on AFM probe tips by inkwell dipping, meniscus dipping, and tip-to-tip DPN were also evaluated using Raman spectroscopy for which some telling results prepared from  $\text{NiCl}_2$  are provided in Figure 40. In this figure, the inkwell dipped tip response is shown in navy blue (dotted line); the meniscus dipped tip is shown in magenta (heavy); and the tip-to-tip DPN sample is provided in green. By evaluating the D and G bands, every sample preparation method exhibits the same peak locations at  $1320$  and  $1590$   $\text{cm}^{-1}$ , respectively. However, with the increasing control of metal salt delivery (meniscus  $\rightarrow$  inkwell  $\rightarrow$  tip-to-tip), a decrease in the relative height of the D band

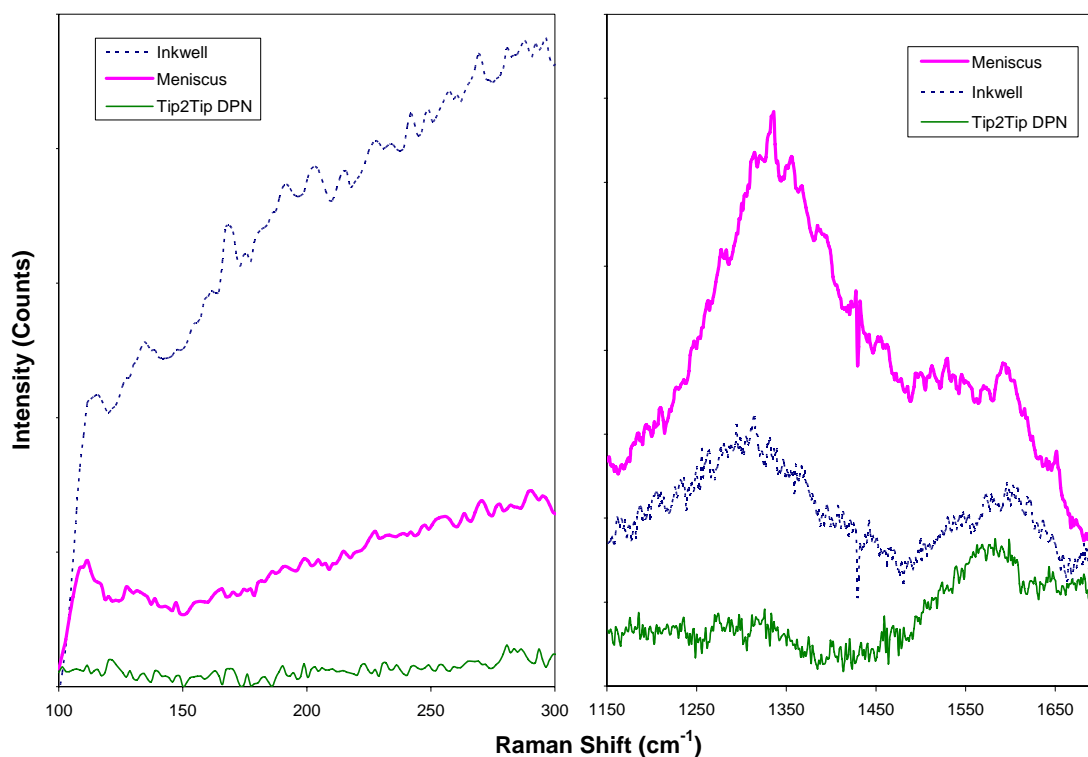


**Figure 40. Raman of Samples Prepared on AFM Probes ( $\text{NiCl}_2$ )**

is apparent. This indicates that the relative proportion of SWNT in the sample increases with the increasing control of salt delivery, culminating in an essentially complete SWNT sample in the tip-to-tip method. The RBM peaks in the meniscus and inkwell dipped samples are fairly indistinct, although a slight peak at roughly  $140\text{ cm}^{-1}$  is observable in both. A similar peak at  $125\text{ cm}^{-1}$  can be seen in the tip-to-tip sample, as well as a small peak at  $270\text{ cm}^{-1}$ . All G band peaks signify primarily semi-conducting tubes, although a shoulder in the response is visible for each sample, indicating some metallic tubes. This is reasonable since the RBM peaks observed correlate to 2 nm diameter tubes, with the exception of the smaller peaks at higher Raman shifts which are the likely contributors to the conducting tubes.

Additionally, Figure 41 shows a similar Raman spectrum for a  $\text{CoCl}_2$  tip-to-tip prepared sample in which, unlike the  $\text{NiCl}_2$  tip-to-tip sample, the results indicated a MWNT sample had formed. RBM peaks are observed at 135, 190, and  $285\text{ cm}^{-1}$ , with a MWNT indicating D band at  $1315\text{ cm}^{-1}$  and a semi-conducting G band at  $1600\text{ cm}^{-1}$ .

The differences observed in these scans as compared to the results from the deposition of  $\text{NiCl}_2$  and  $\text{CoCl}_2$  on the  $\text{SiN}_3$  window grids may be the result of differing particle formation at the corners of the probe prism. These variations in surface energy may result in metal particle sizes along these boundaries which are larger than those on the flat surface, which is qualified by the presence of the 2 nm CNT on the tip-to-tip samples. The results also indicate that the formation energy of the different metal particles differ slightly such that the Co particles primarily form MWNT whereas the Ni particles form SWNT on the surface of the AFM probe.

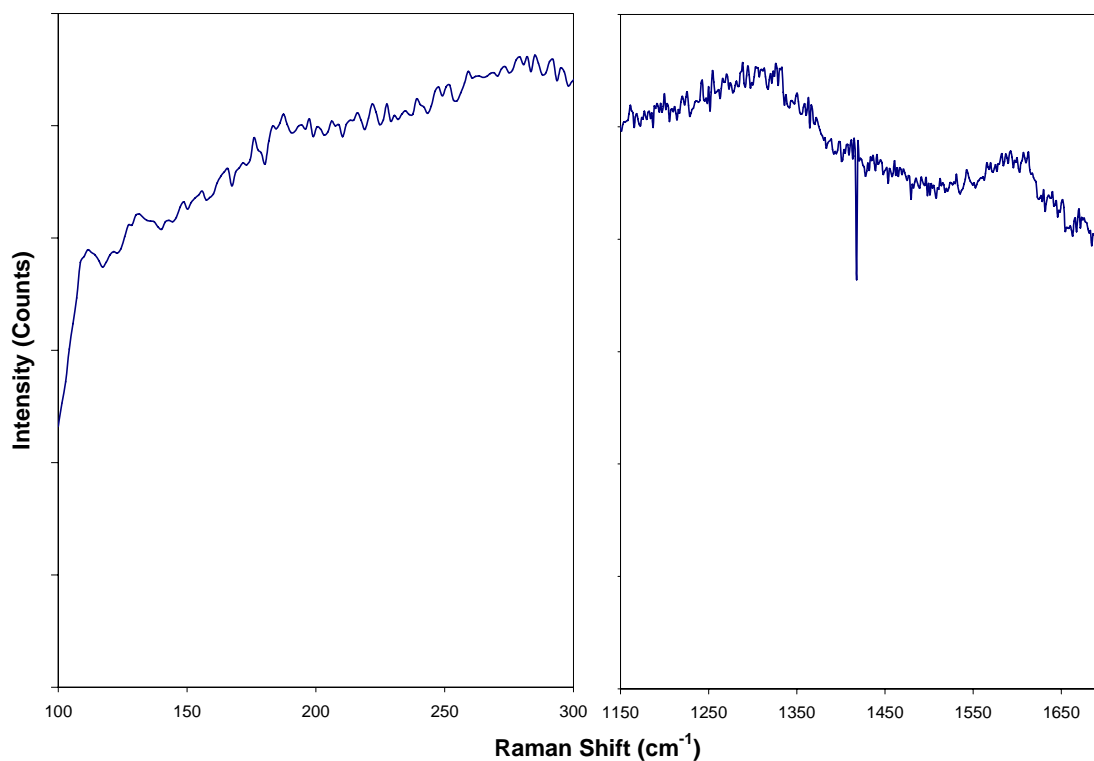


**Figure 41. CoCl<sub>2</sub> Tip-to-Tip CNT Sample Raman Spectrum**

#### 4.5.3 Overview of Raman Results

In review, the results of the Raman spectral evaluations showed the use of DPN to deliver the catalyst agents for nanotube growth in CVD effectively generated SWNT of metallic type except in the case of tip-to-tip DPN where differing surface energy likely resulted in the formation of both conducting and semi-conducting CNT. The use of differing catalyst agents also resulted in different formations. The bulk samples primarily generated semi-conducting MWNT except in the cases of CoCl<sub>2</sub>, where a SWNT peak was observed in the RBM of the bulk sample in addition to the presence of mixed metallic and semi-conducting tubes as indicated in the DPN samples G band. In

the NiCl<sub>2</sub>-CoCl<sub>2</sub> mixture, the bulk sample also rendered SWNT although semi-conducting in type. DPN of PdCl<sub>2</sub> appeared to have the best performance in creating metallic SWNT while also having the highest aspect ratio, as indicated by both the intensity of the G band peak and the bundle of tubes observed by TEM.

## CHAPTER V

### CONCLUSION

Since the discovery of carbon nanotubes, scientists and engineers have sought to exploit their amazing properties in various technologies and applications. Though the science of using dip pen nanolithography as a means of controlled delivery of catalyst materials for CNT growth is still in its infancy, the work presented herein has shown it to be a viable means of producing CNTs when used in conjunction with CVD synthesis processes. Using this method of “nano-gardening,” the growth of tubes in specified locations with nanometer resolution is possible, allowing for the development of nano-arrays of CNTs and eventually, the ability to grow entire nano-circuit boards. Moreover, the results indicate that the tubes grown using this process can be designed as metallic in type based on the selection of catalyst material – an unprecedented feat in the production of carbon nanotubes! Up to this point, all samples of CNTs consist of mixtures of both conducting and semi-conducting tubes, making the development of CNTs for nano-electronics incredibly difficult because of the complex separation processes that would be necessary.

As in many technological advances, this process is yet to be completely refined. Currently, processing results in a large degree of amorphous carbon in proportion to the tube growth, which must be eliminated for use in future systems. Additionally, although the DPN catalyst delivery process results in fairly uniform tube diameters, the lengths of the tubes are not properly controlled. An idea to possibly solve both of these problems is



to use a variation of the current process where the writing tip on the cantilever is also a MEMS heating device. Presumably, if writing in a controlled atmosphere of ethanol, the heated tip would grow the tubes as it was writing the pattern, such that proper atmospheric concentration and tip speed could result in a patterned tube of precise size, shape, and location. Additionally, at this point, only conducting type tubes have been grown, and it would be advantageous to determine the proper conditions for growing other chiralities so that all aspects of CNT applications could be exploited.

**REFERENCES**

- (1) Singer J.M.; Grumer J. *Proc. Combust. Inst.* **1959**, 7, 559.
- (2) Su, D.S.; Chen, X. *Angew. Chem. Int. Ed.* **2007**, 46, 1823.
- (3) Lerner, E. *The Industrial Physicist* December **1999**, pp. 22-25.
- (4) Iijima, S. *Nature* **1991** 354, 56.
- (5) Ebbesen, T. W.; Ajayan, P. M. *Nature* **1992**, 358, 220.
- (6) Collins, P. G.; Avouris, P. *Scientific American* December **2000**, pp. 67-69.
- (7) Guo, T.; Nikolaev, P.; Thess, A.; Colbert, D.T.; Smalley, R.E. *Chem. Phys. Lett.* **1995**, 243, 49.
- (8) Ouellette, J. *The Industrial Physicist* December **2002**, pp. 18-21.
- (9) José-Yacamán, M.; Miki-Yoshida, M.; Rendon, L.; Santiesteban, J.G. *Appl. Phys. Lett.* **1993**, 62(6), 657.
- (10) Ren, Z. F. *Science* **1998**, 282, 1105.
- (11) Yasuda, A.; Kawase, N.; Mizutani, W. *J. Phys. Chem. B* **2002**, 106(51), 13294.
- (12) Sinnot, S. B.; Andrews, R.; Qian, D.; Rao, A. M.; Mao, Z.; Dickey, E. C.; Derbyshire, F. *Chem. Phys. Lett.* **1999**, 315, 25.
- (13) Li, Y.; Kim, W.; Zhang, Y.; Rolandi, M.; Wang, D.; Dai, H. *J. Phys. Chem. B* **2001**, 105, 11424.
- (14) Tang, X.-P.; Kleinhammes, A.; Shimoda, H.; Fleming, L.; Bennoune, K. Y.; Sinha, S.; Bower, C.; Zhou, O.; Wu, Y. *Science* **2000** 288, 492.
- (15) Dresselhaus, M. S.; Eklund, P. C. *Adv. Phys.* **2000** 49(6), 705.

- (16) Dresselhaus, M.S.; Dresselhaus, G.; Saito, R.; Jorio, A. *Physics Reports* **2005**, *409*(2), 47.
- (17) Jorio, A.; Saito, R.; Hafner, J.H.; Lieber, C.M.; Hunter, M.; McClure, T.; Dresselhaus, G.; Dresselhaus, M. S. *Physical Review Letters* **2001**, *86*(6), 1118.
- (18) Bandow, S.; Asaka, S.; Saito, Y.; Rao, A.M.; Grigorian, L.; Richter, E.; Eklund, P.C. *Phys Rev Lett* **1998**, *80*(17), 3779.
- (19) Saito, R.; Jorio, A.; Filho, A.; Dresselhaus, G.; Dresselhaus, M.; Grüneis, A.; Cançado, L.; Pimenta, M. *Jpn. J. Appl Phys* **2002**, *41*, 4878.
- (20) Pimenta, M.A.; Marucci, A.; Brown, S.D.M.; Matthews, M.J.; Rao, A.M.; Eklund, P.C.; Smalley, R.E.; Dresselhaus, G.; Dresselhaus, M.S. *J. Material Research* **1998**, *13*(9), 2405.
- (21) Robertson, J. *Materials Today* **2007**, *10*, 36.
- (22) Grobert, N. *Materials Today* **2007**, *10*, 28.
- (23) Bonard, J.-M.; Stora, T.; Salvétat, J.-P.; Maier, F.; Stöckli, T.; Duschl, C.; Forró, L.; de Heer, W.A.; Châtelain, A. *Adv. Mater.* **1997**, *9*, 827.
- (24) Liu, X. M.; Spencer, J.L.; Kaiser, A.B.; Arnold, W.M. *Curr. Appl. Phys.* **2006**, *6*(3), 427.
- (25) Banerjee, S.; Wong, S. S. *J. Phys. Chem. B* **2002**, *106*, 12144.
- (26) Piner, P.; Zhu, J.; Xu, F.; Hong, S.; Mirkin, C. *Science* **1999**, *283*, 661.
- (27) Schwartz, P. *Langmuir* **2002**, *18*, 4041.
- (28) Weeks, B. Vaughn, M.W.; DeYoreo, J.J.; *Langmuir* **2005**, *21*(18), 8096.

- (29) Weeks, B.L.; Noy, A.; Miller, A.E.; De Yoreo, J.J. *Phys Rev Lett* **2002**, *88*, 255505.
- (30) Manandhar, P.; Jang, J.; Schatz, G.C.; Ratner, M.A.; Hong, S. *Phys Rev Lett* **(2003)** *90*, 115505.
- (31) Sheehan, P.; Whitman, L. *Phys Rev Lett* **2002**, *88*, 156104.
- (32) Freund, J.; Halbritter, J.; Hörber, J.K.H. *Microscopy Research and Technique* **1999**, *44*, 327.
- (33) Mirkin, C.; Piner, R.; Rozhok, S. *J. Phys. Chem B* **2003**, *107*, 751.
- (34) Hampton, J.R.; Dameron, A.A.; Weiss, P. *JACS* **2006**, *128*, 1648.
- (35) Salaita, K.; Amarnath, A.; Maspoch, D.; Higgins, T.B.; Mirkin, C.A. *JACS* **2005**, *127*, 11283.
- (36) Mirkin, C.; Hong, S. *Science* **2000**, *288*, 1808.
- (37) Sheehan, P.; Whitman, L. J.; King, William P.; Nelson, Brent A. *Applied Physics Letters* **2004**, *85*(9), 1589.
- (38) Jang, J.; Hong, S.; Schatz, G.C.; Ratner, M.A. *J. Chem. Phys.* **2001**, *115*(6), 2721.
- (39) Rivas-Cardona, J.A.; Banerjee, D. *J. Micro/Nanolith. MEMS MOEMS* **2007**, *6*, 033004.
- (40) Hong, S.; Zhu, J. *Science* **1999**, *286*, 523.
- (41) Su, M.; Liu, X.; Li, S.-Y.; Dravid, V.P.; Mirkin, C.A. *J. Am. Chem. Soc.* **2002**, *124*, 1560.
- (42) Li, Y.; Maynor, B.; Liu, J. *J. Am. Chem. Soc.* **2001**, *123*, 2105.
- (43) Maynor, B.; Li, Y.; Liu, J. *Langmuir* **2001**, *17*, 2575.

- (44) Zhang, M.; Bullen, D.; Chung, S.-W.; Hong, S.; Ryu, K.S.; Fan, Z.; Mirkin, C.A.; Liu, C. *Nanotechnology* **2002**, *13*, 212.
- (45) Liu, X.; Fu, L.; Hong, S.; Dravid, V.P.; Mirkin, C.A. *Advanced Materials* **2002**, *14*, 231.
- (46) Lee, K.B.; Park, S.J.; Mirkin, C.A.; Smith, J.C.; Mrksich, M. *Science* **2002**, *295*, 1702.
- (47) Lander, E.S. *Nat. Genet.* **1999**, *21*, 3.
- (48) Sinha, S.; Barjami, S.; Iannacchione, G.; Schwab, A.; Muench, G. *Journal of Nanoparticle Research* **2005**, *7*(6), 651.

## APPENDIX A

### XPS ELECTRON HYBRIDIZATION LEVELS

Below is a table listing the binding energies corresponding to elemental electron hybridization levels as measured by XPS. This table is for use in identifying the peaks seen in the XPS responses provided in the text (Figure 20 and Figure 21). These values were obtained from the NIST XPS database, available online at <http://srdata.nist.gov/xps/>.

**Table 2. Binding Energies for Elements Present on Metal Salt Samples**

Binding Energy Value at Peaks (eV)	Corresponding Elements Present on Sample		
	NiCl <sub>2</sub>	CoCl <sub>2</sub>	PdCl <sub>2</sub>
1008	Ni 2s	-	-
928	-	Co 2s	-
920	-	-	Pd MMNa
870	Ni 2p <sub>3/2</sub>	-	-
855	Ni 2p <sub>1/2</sub>	-	-
796	-	Co 2p 1/2	-
605	-	Co LMMc	-
532	-	-	Pd 3p 3/2
529	O 1s	O 1s	O 1s
490	Ni LMMc	-	-
485	-	Co LMMa	-
410	Ni LMMa	-	-
342	-	-	Pd 3d 3/2
337	-	-	Pd 3d 5/2
285	C 1s	C 1s	C 1s
270	Cl 2s	Cl 2s	Cl 2s
153	Si 2s	Si 2s	Si 2s
112	Ni 3s	-	-
103	Si 2p	Si 2p	Si 2p
101	-	Co 3s	-
68	Ni 3p	-	-
51	-	-	Pd 4p
23	O 2s	O 2s	O 2s

## APPENDIX B

### RAMAN SPECTRA FOR SAMPLES BY EXCITATION WAVELENGTH

The following pages present Raman spectral data taken for several of the samples on which CNT were synthesized. The data presented in this appendix is complimentary to the results provided in the text. The data presented in the main text were chosen specifically for the clarity of the information provided by the spectral responses, whereas the information (e.g., intensity peaks) in the following charts were not always as clearly defined. Herein, the graphs are presented by sample type and laser excitation wavelength. Figure B - 1 through B – 10 provide comparative graphs for both 633 and 785 nm excitation wavelengths. These charts also show that the same results were obtained for various samples from similar processes, although of different DPN deposition size (the titles describe sample number – in parentheses – and locations of DPN depositions on the given sample, if applicable). Corner A, B, C, and D provided in these graphs correspond to DPN deposition sizes of 1  $\mu\text{m}$ , 500 nm, 250 nm, and 2  $\mu\text{m}$  respectively. Also, in Figure B - 8, the anomaly described in the text and referred to in Figure 39 is presented a second time. These charts show that typically the D and G bands are more easily evaluated when excited by the 633 nm laser although both lasers will indicate the peaks. Sometimes the signal intensity of the peaks are weak in the 785 nm scans, though they are still present. The RBM peaks can be observed in the Raman spectra obtained by using either laser source, of which the spectra with the best clarity were reported in the results section in the main body of the text.

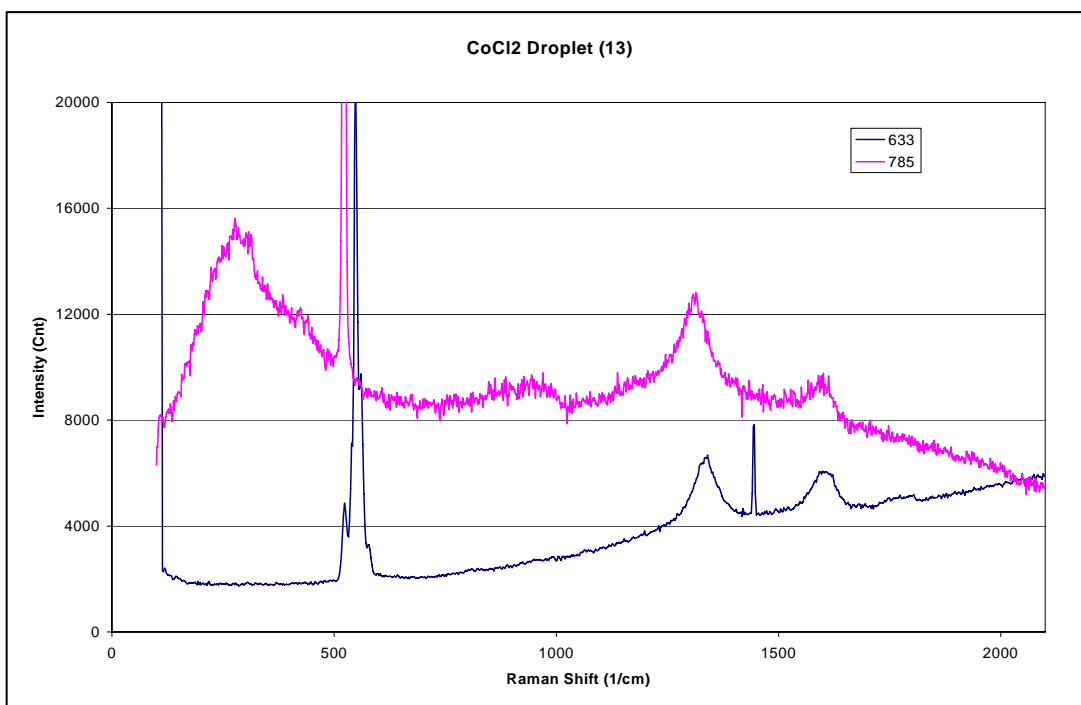


Figure B - 1. Spectra Excitation Comparison of Bulk Prepared CNT Sample of CoCl<sub>2</sub>

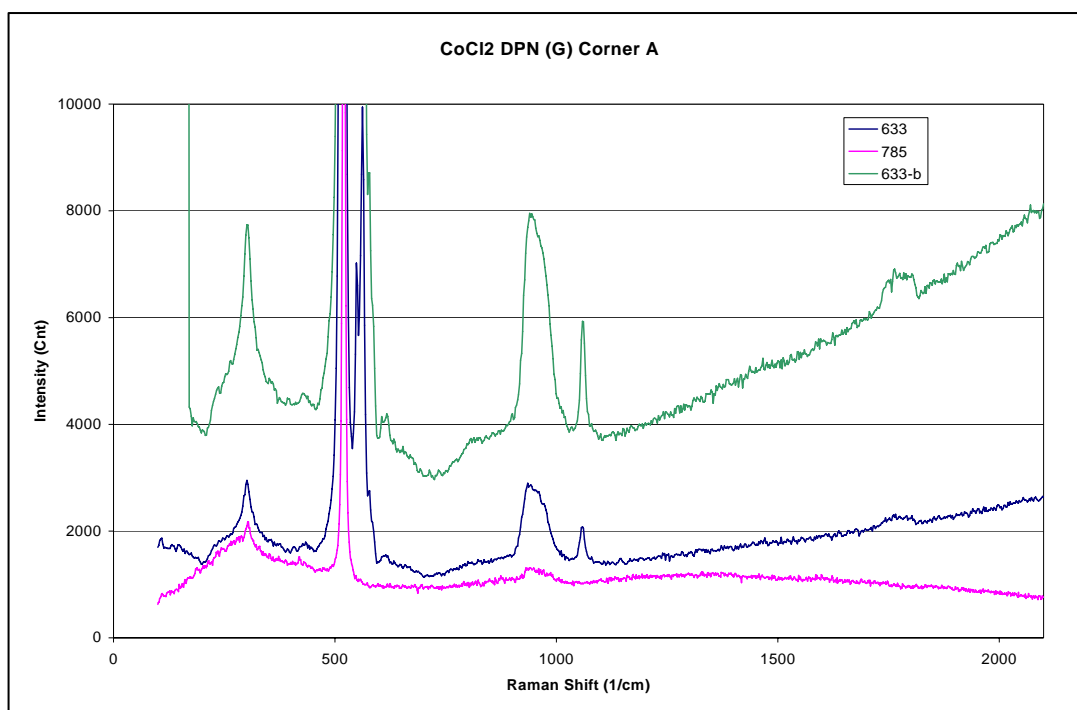


Figure B - 2. Spectra Excitation Comparison of 1  $\mu$ m DPN Patterned CNT Sample of CoCl<sub>2</sub>



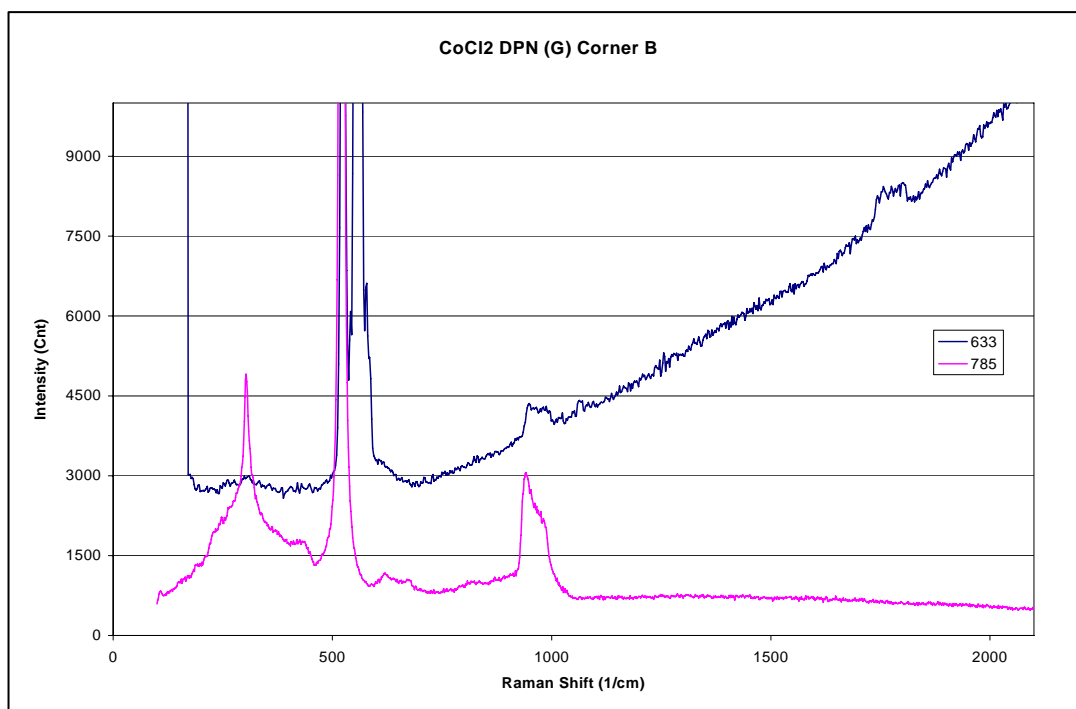


Figure B - 3. Alternate Excitation Comparison of 500 nm DPN Patterned CNT Sample of CoCl<sub>2</sub>

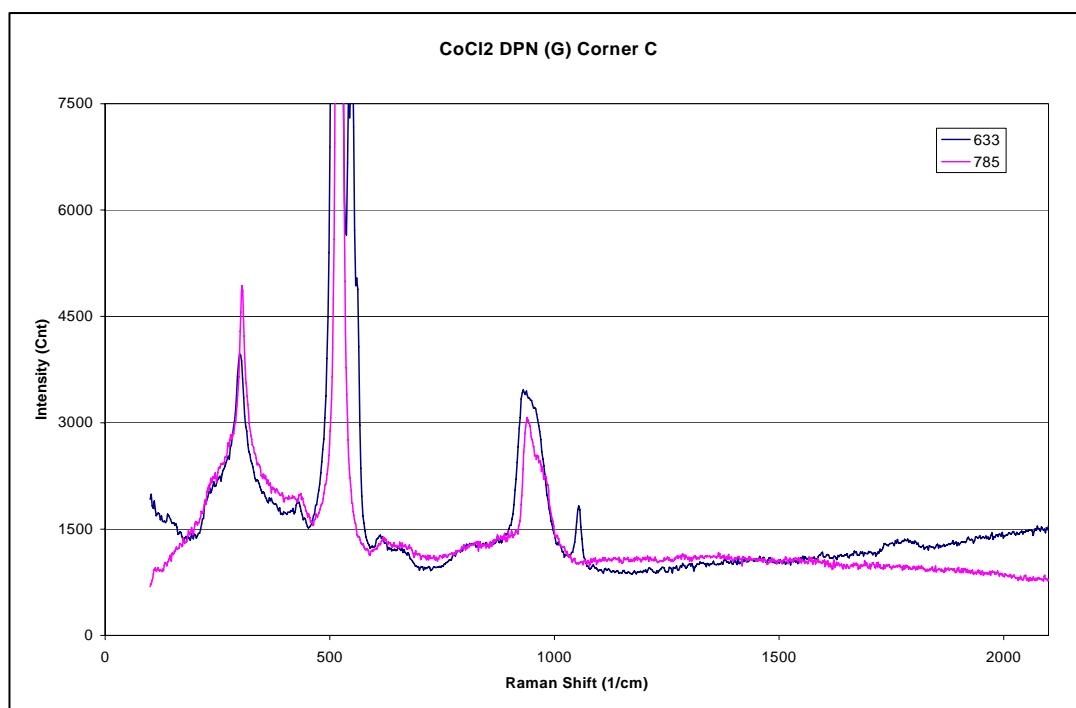


Figure B - 4. Alternate Excitation Comparison of 250nm DPN Patterned CNT Sample of CoCl<sub>2</sub>

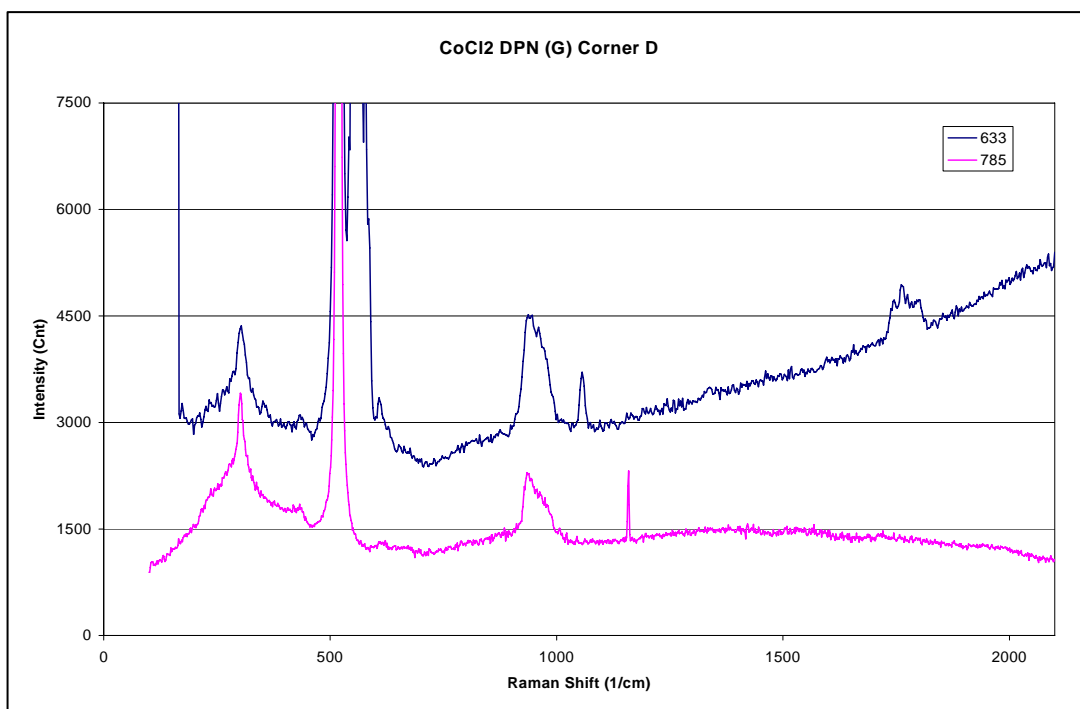


Figure B - 5. Alternate Excitation Comparison of 2  $\mu$ m DPN Patterned CNT Sample of CoCl<sub>2</sub>

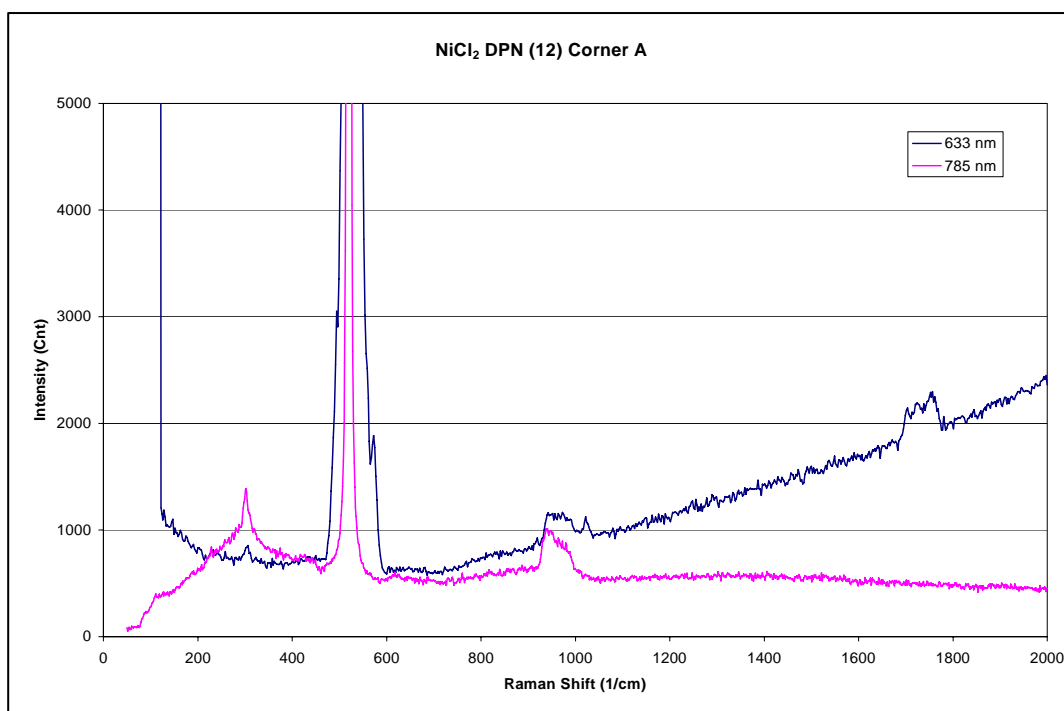
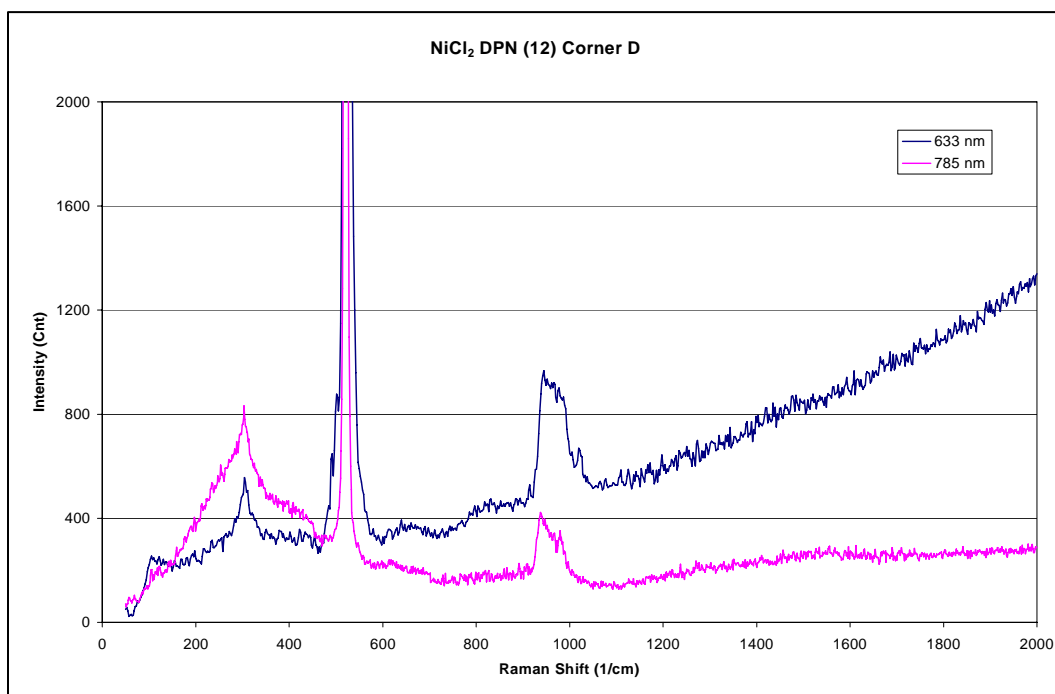
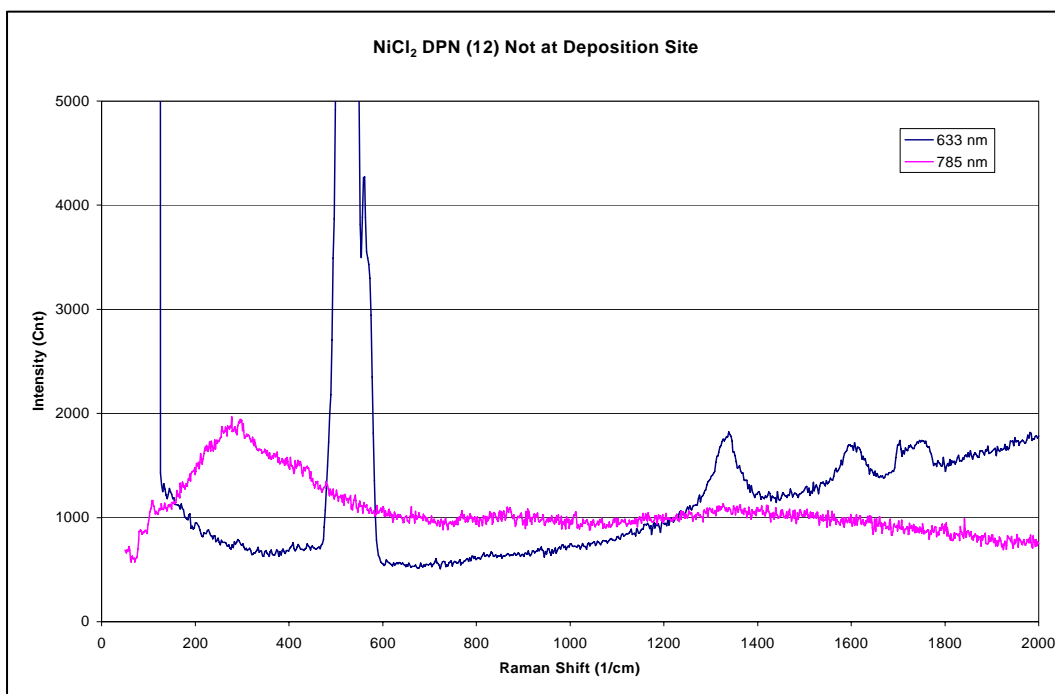


Figure B - 6. Excitation Comparison of 1  $\mu$ m DPN Patterned CNT Sample of NiCl<sub>2</sub>



**Figure B - 7. Alternate Excitation Comparison of 2  $\mu\text{m}$  DPN Patterned CNT Sample of NiCl<sub>2</sub>**



**Figure B - 8. Excitation Comparison of DPN Prepared CNT Sample of NiCl<sub>2</sub> Exhibiting an Anomalous Response Away from Deposition Site**

The following two figures compare bulk and DPN prepared samples of PdCl<sub>2</sub> when using both laser excitations.

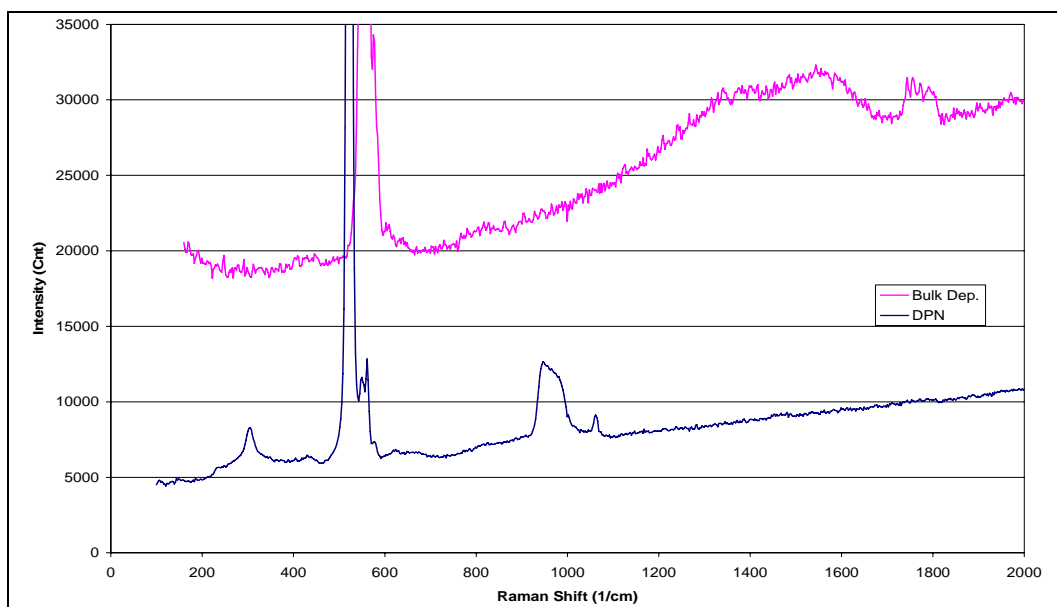


**Figure B - 9. Bulk and DPN Prepared CNT Samples of PdCl<sub>2</sub> Observed with 633 nm Laser**

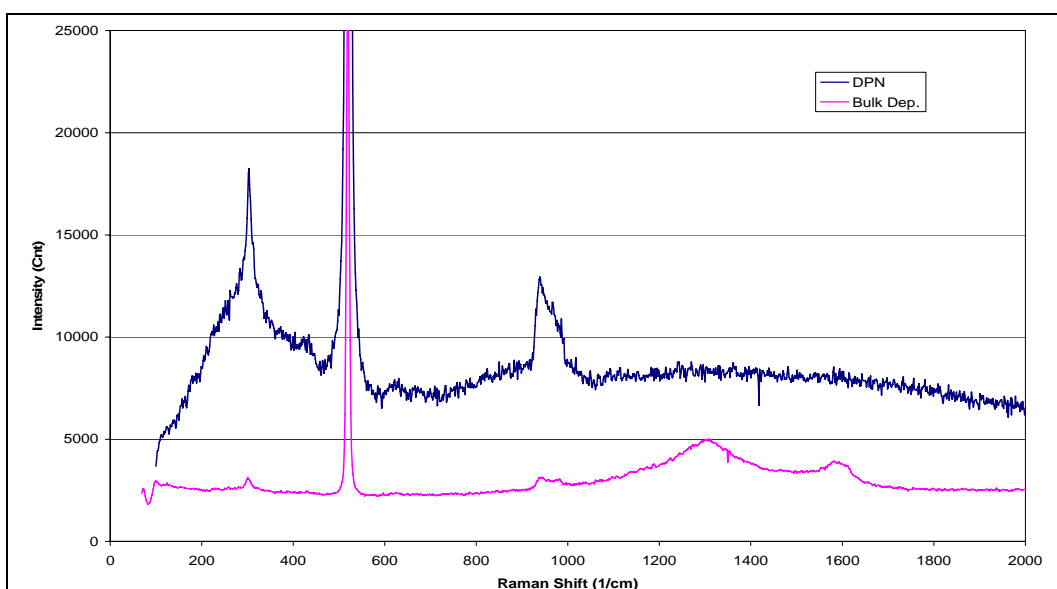


**Figure B - 10. Bulk and DPN Prepared CNT Samples of PdCl<sub>2</sub> Observed with 785 nm Laser**

The following graphs contain several additional Raman scans showing the presence of CNT after CVD processing of various sample types. In the figure legends, Tips 1 and 2 refer to the two tips present on the AFM probe. When a “Different Location” is mentioned in reference to the tips, this means the scan was performed on the base of the cantilever supporting the tip. On those figures referring to bulk deposits on any substrates, the numbers in the legend refer to different areas on the substrate where CNTs were observed. In a couple figures, the magnification level of the objective lens is mentioned to show differences when observing at different magnifications; however, if not listed, the magnification at which the spectra were obtained is 100x. When performing Raman analyses of the DPN samples performed on  $\text{SiN}_3$ , a naming convention of A, B, C, and D was adopted to describe the location of the deposition. These locations are referred to in a few of the charts, but of most importance, the charts where the legend indicates “near D,” etc., explains that the sample being observed was not at the location of the deposition, but at a significant distance in the vicinity of the said location. This distance was typically greater than 50 microns. Similarly, where “perf” is listed in the charts, this refers to signals obtained on the perforated region of the  $\text{SiN}_3$  window grids, where no DPN patterning had been performed. The numbers incorporated into the legend text in these figures indicate repeated scans of the same location which were slightly enhanced by changing the scan parameters.

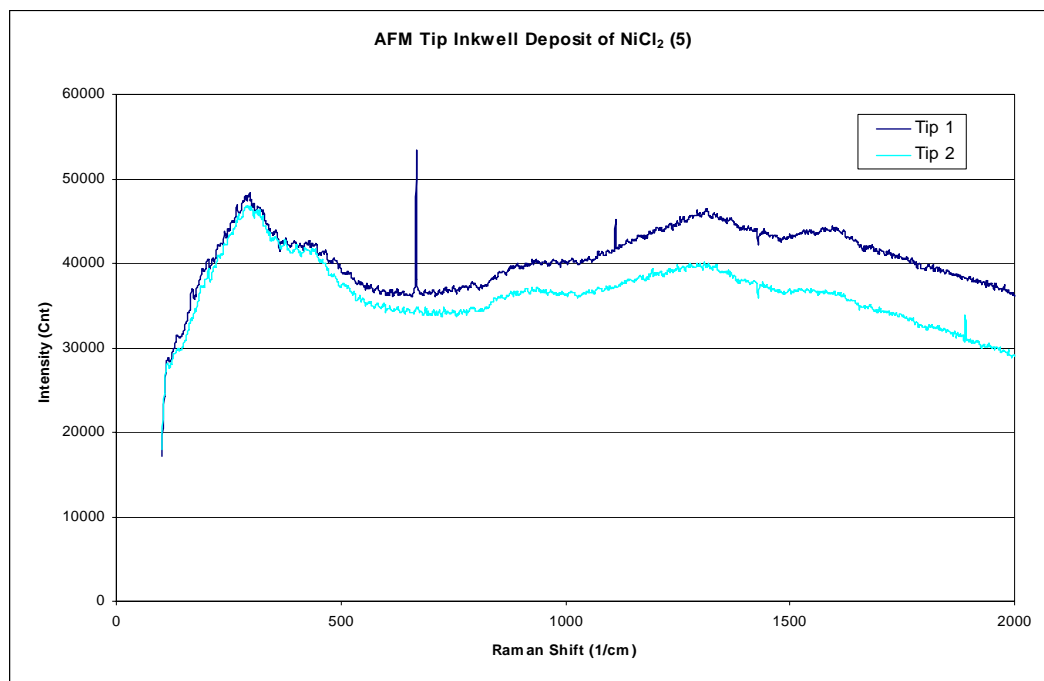


Figure B - 11. 785 nm Excitation of NiCl<sub>2</sub> Inkwell Dipped Tips

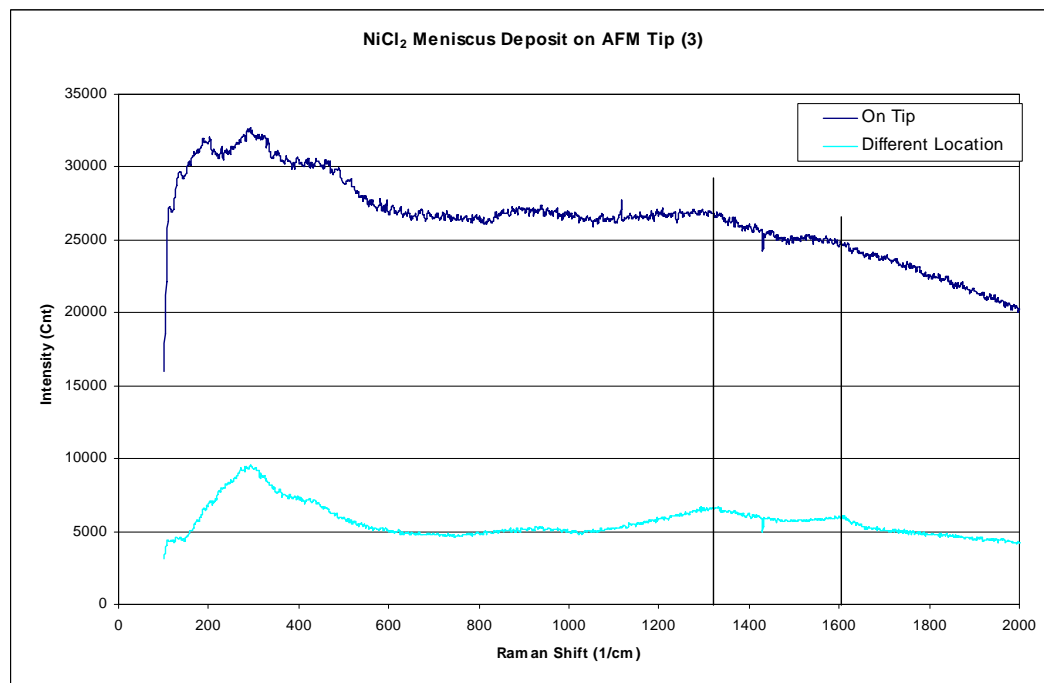
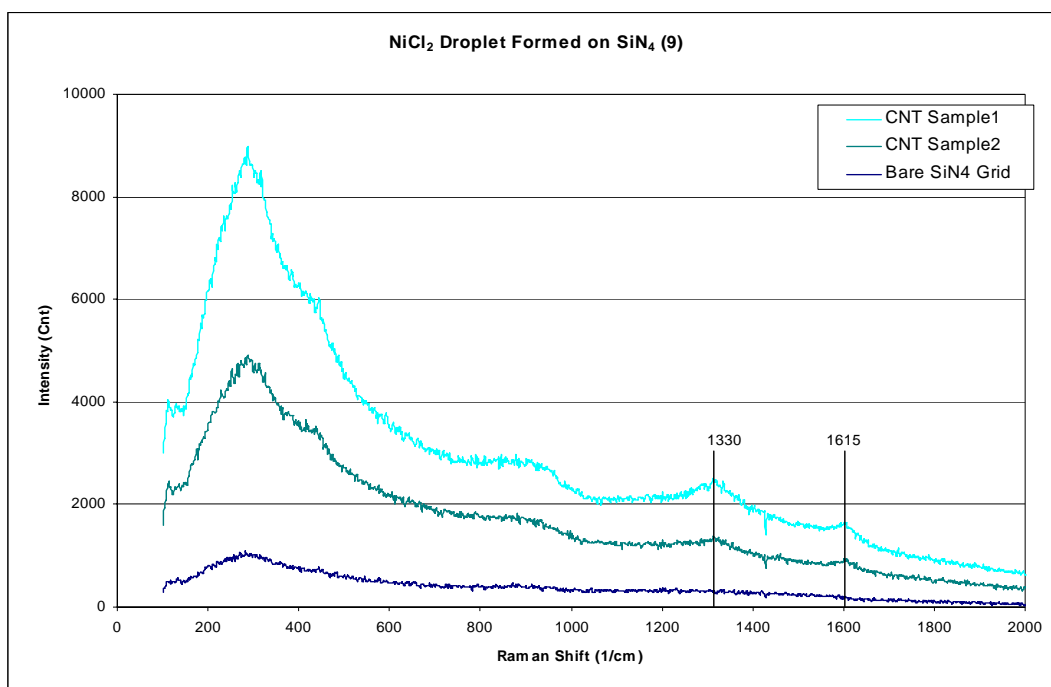
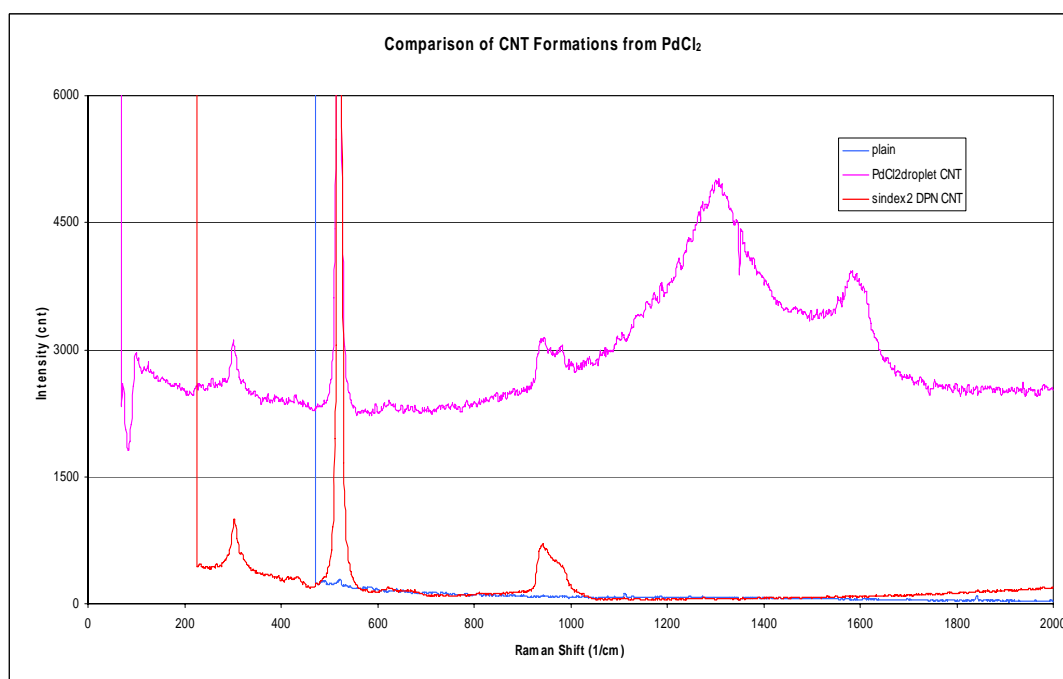


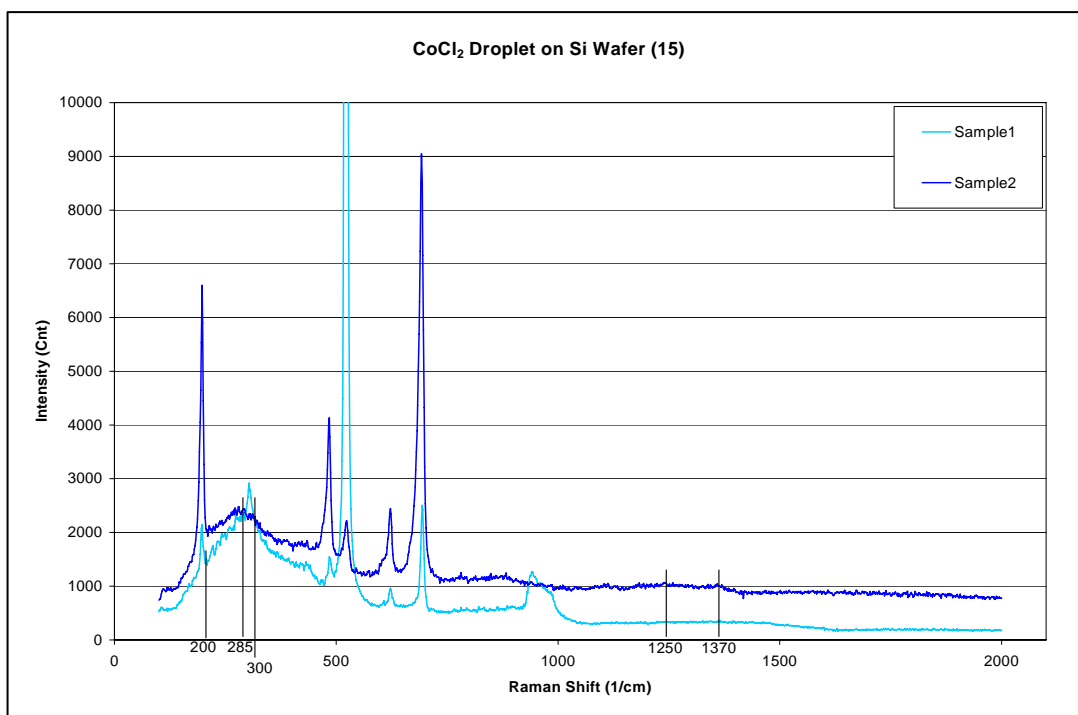
Figure B - 12. 785 nm Excitation of NiCl<sub>2</sub> Sample. Meniscus Dipped Tip and Cantilever Arm of the Scanning Probe.



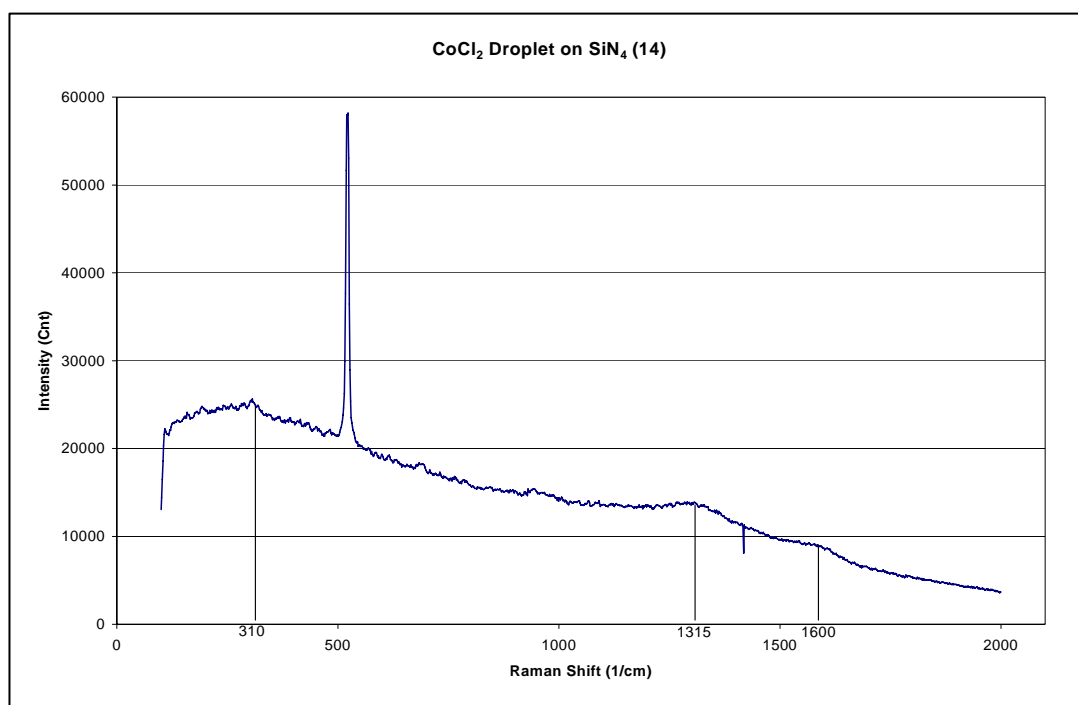
**Figure B - 13.** 785 nm Excitation of NiCl<sub>2</sub> Bulk Deposited Samples on SiN<sub>3</sub> Compared to Bare SiN<sub>3</sub>



**Figure B - 14.** Comparison of 785 nm Excitation on Bare Substrate and on CNT Obtained from PdCl<sub>2</sub> Catalysts by Bulk and DPN Deposition on Sindex Substrate

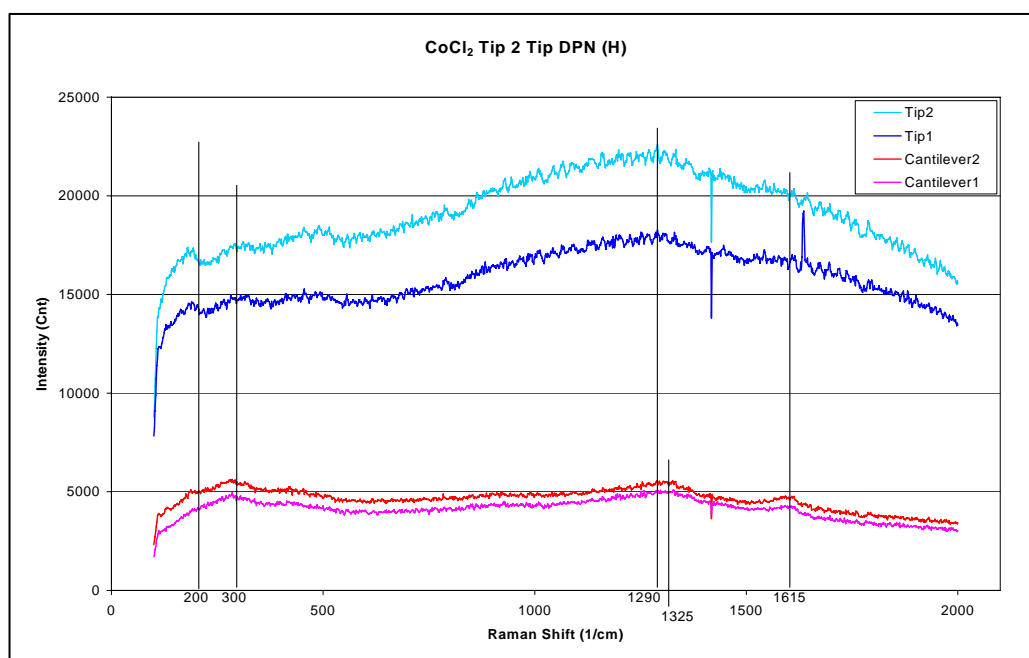


**Figure B - 15. 785 nm Excitation of CoCl<sub>2</sub> Bulk Deposited Samples on Si**

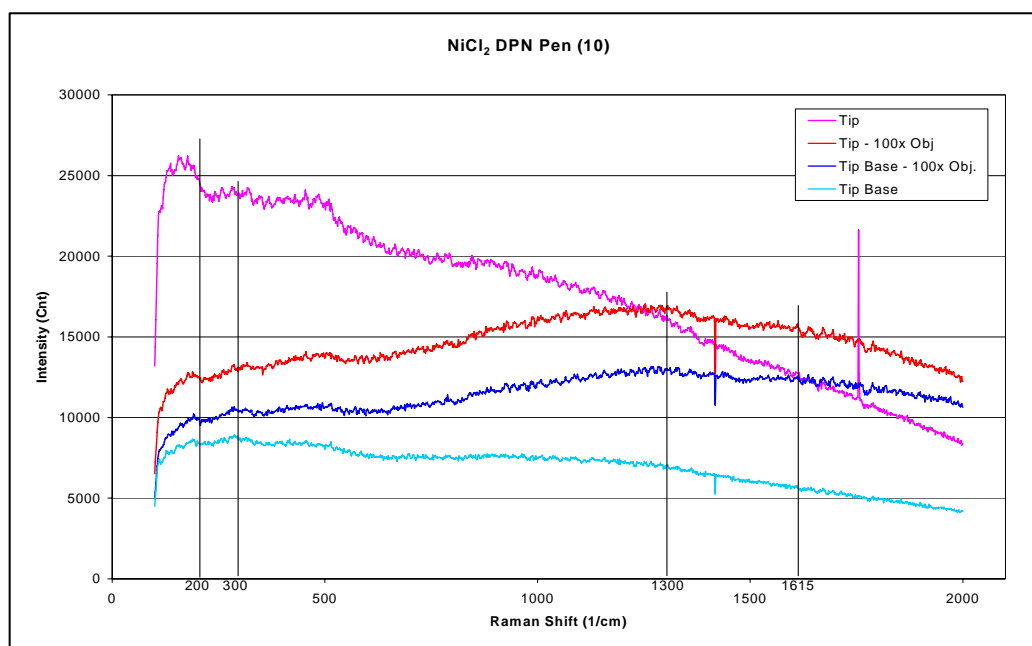


**Figure B - 16. 785 nm Excitation of CoCl<sub>2</sub> Bulk Deposited Sample on SiN<sub>3</sub>**

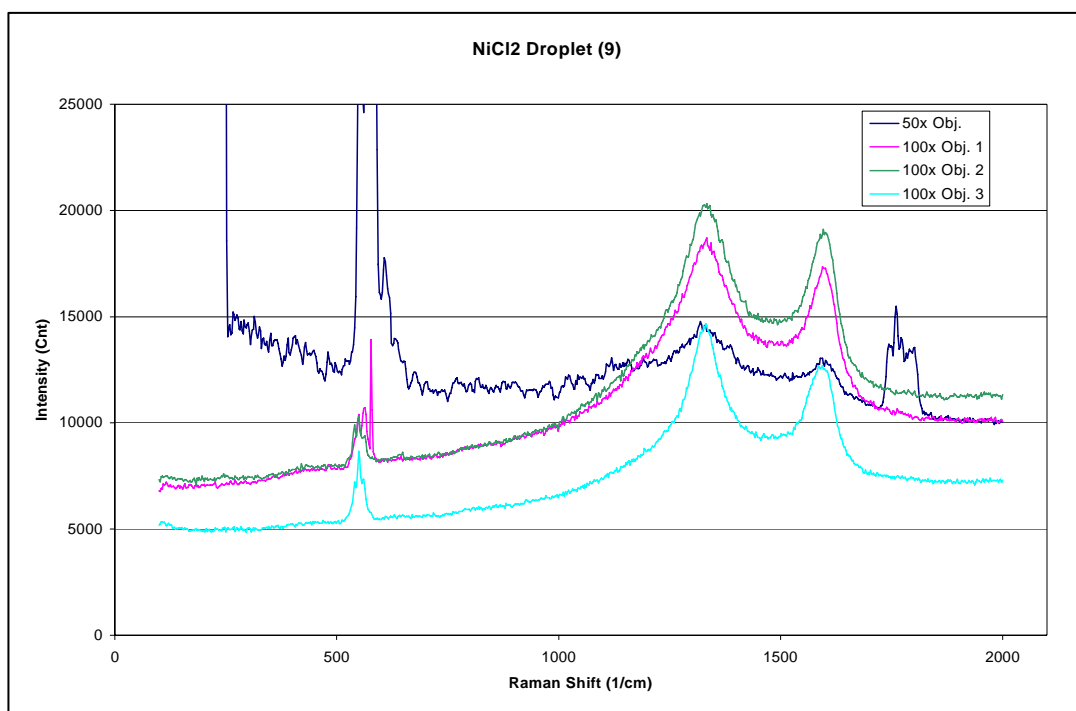
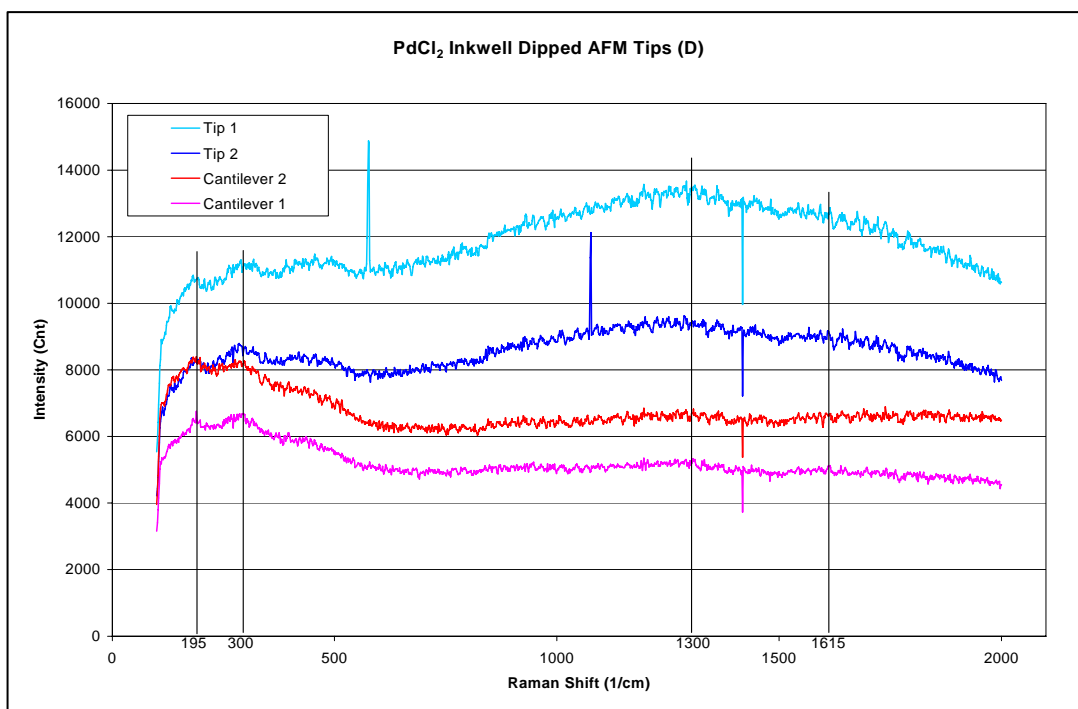


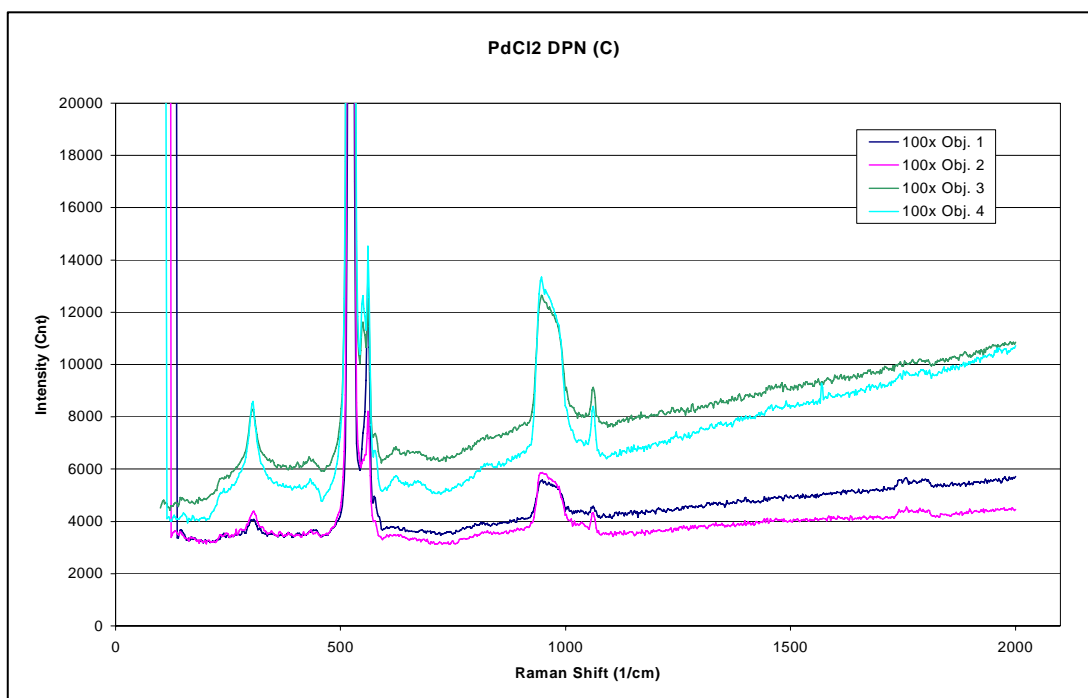
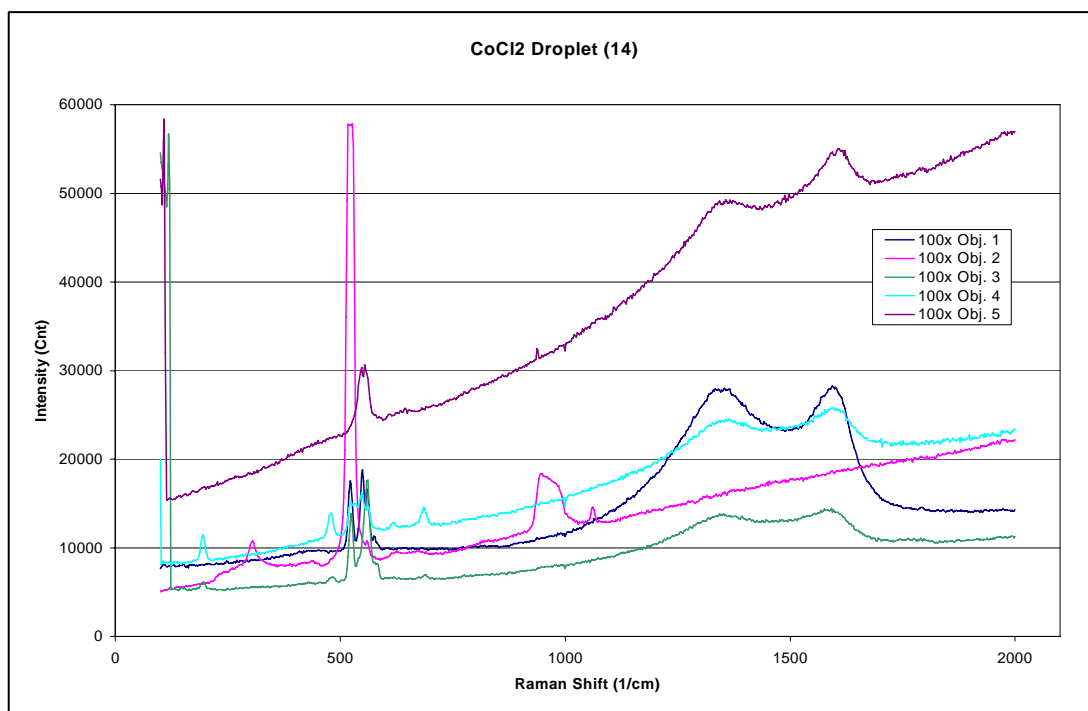


**Figure B - 17. 785 nm Excitation of CNT Obtained by Deposition of CoCl<sub>2</sub> Catalysts using Tip-to-Tip Deposition. (Responses Obtained Away from the Tip though Still Patterned - On the Cantilever Arm of the Scanning Probe - is Also Shown for Reference)**



**Figure B - 18. 785 nm Excitation after CVD on the NiCl<sub>2</sub> Catalysts Remaining on the Tip of the DPN Pen (Double Dipping Procedure)**





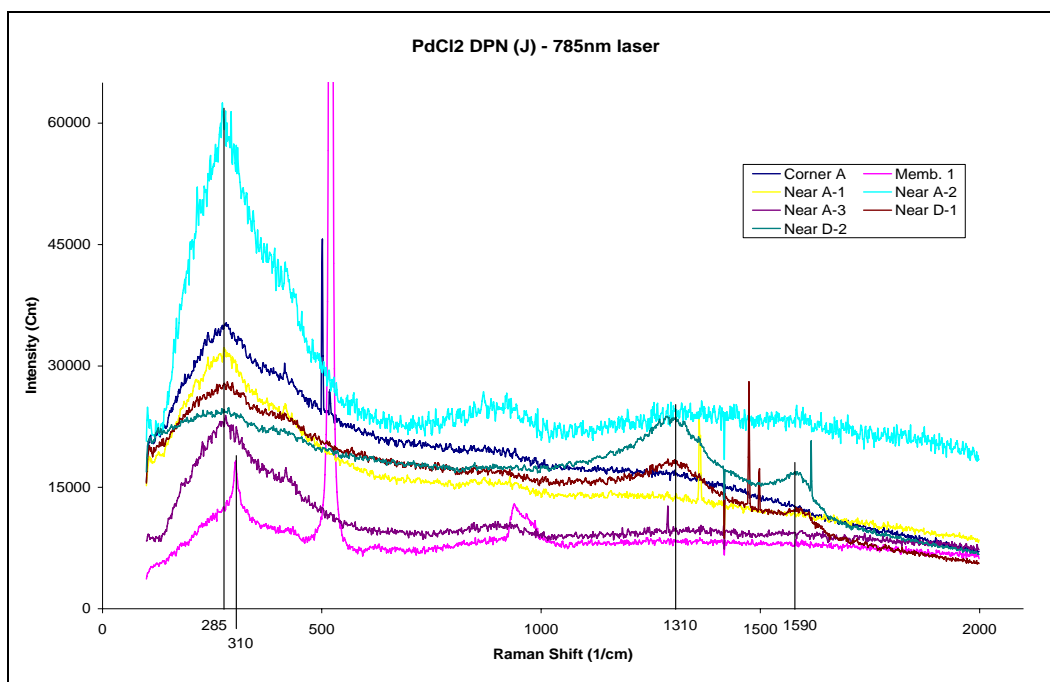


**Figure B - 23. 785 nm Excitation of PdCl<sub>2</sub> DPN Deposited Samples on SiN<sub>3</sub>. The Figure Also Shows Anomalies Away from DPN Locations**

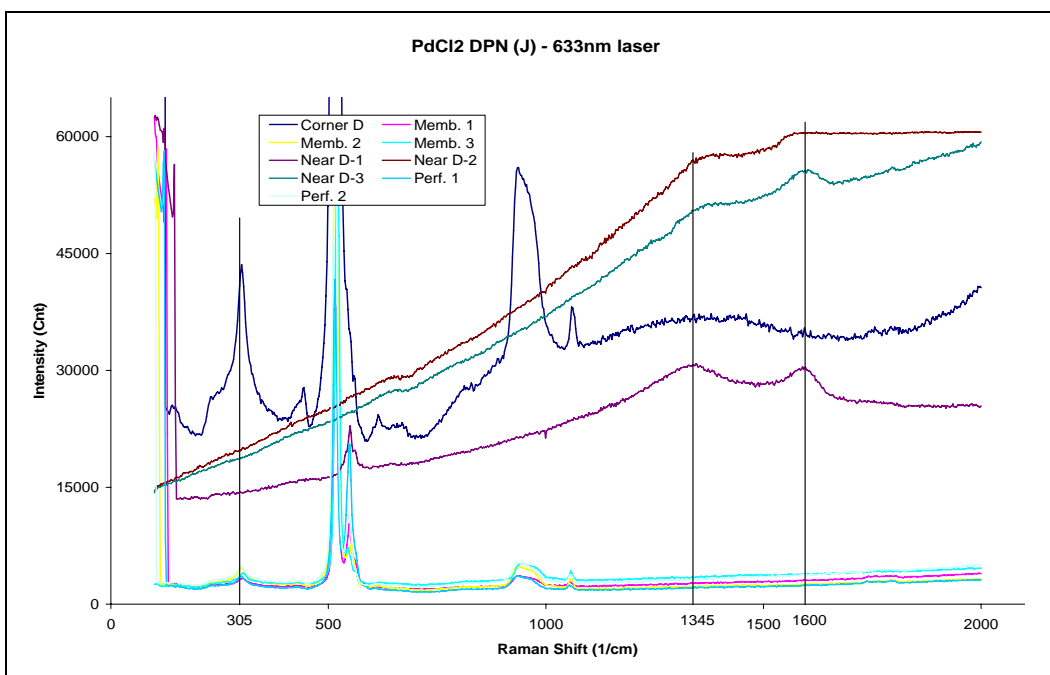


**Figure B - 24. Raman Spectra Obtained by 633 nm Excitation of PdCl<sub>2</sub> DPN Deposited Samples on SiN<sub>3</sub>. The Figure Also Shows Anomalies Away from DPN Locations**

**VITA**

Name: David Huitink

Address: Department of Mechanical Engineering

c/o Dr. Debjyoti Banerjee

Texas A&M University

College Station, Texas 77843-3123

Education: M.S., Mechanical Engineering, Texas A&M University, Dec. 2007.

B.S., Mechanical Engineering, Texas A&M University, Aug. 2006.

Publications:

1. Huitink, D.; Banerjee, D.; Sinha, S.K. "Nanolithography of Metal Catalysts Using Dip Pen Nanolithography (DPN<sup>TM</sup>).” SPIE Defense and Security Symposium **2007**, Orlando, FL. *Paper # 6556-22*.
2. Huitink, D.; Banerjee, D.; Sinha, S.K. "Precise Control of Carbon Nanotube Synthesis of a Single Chirality.” IMECE **2007**, Seattle, WA. *Paper # 42588*.